

CATALOGED BY STIA  
AS AD 1187  
404189

**BRL**

REPORT NO. 1187  
JANUARY 1963

**SUMMARY REPORT ON STRONGARM ROCKET MEASUREMENTS OF  
ELECTRON DENSITY TO AN ALTITUDE OF 1500 KILOMETERS**

Spence T. Marks  
Charles E. Shafer  
William J. Cruickshank  
Raymond E. Prenatt  
George A. Dulk

RDT & E Project No. 1A011001B021  
**BALLISTIC RESEARCH LABORATORIES**

**ABERDEEN PROVING GROUND, MARYLAND**

ASTIA AVAILABILITY NOTICE

Qualified requestors may obtain copies of this report from ASTIA.

The findings in this report are not to be construed  
as an official Department of the Army position.

BALLISTIC RESEARCH LABORATORIES

REPORT NO. 1187

JANUARY 1963

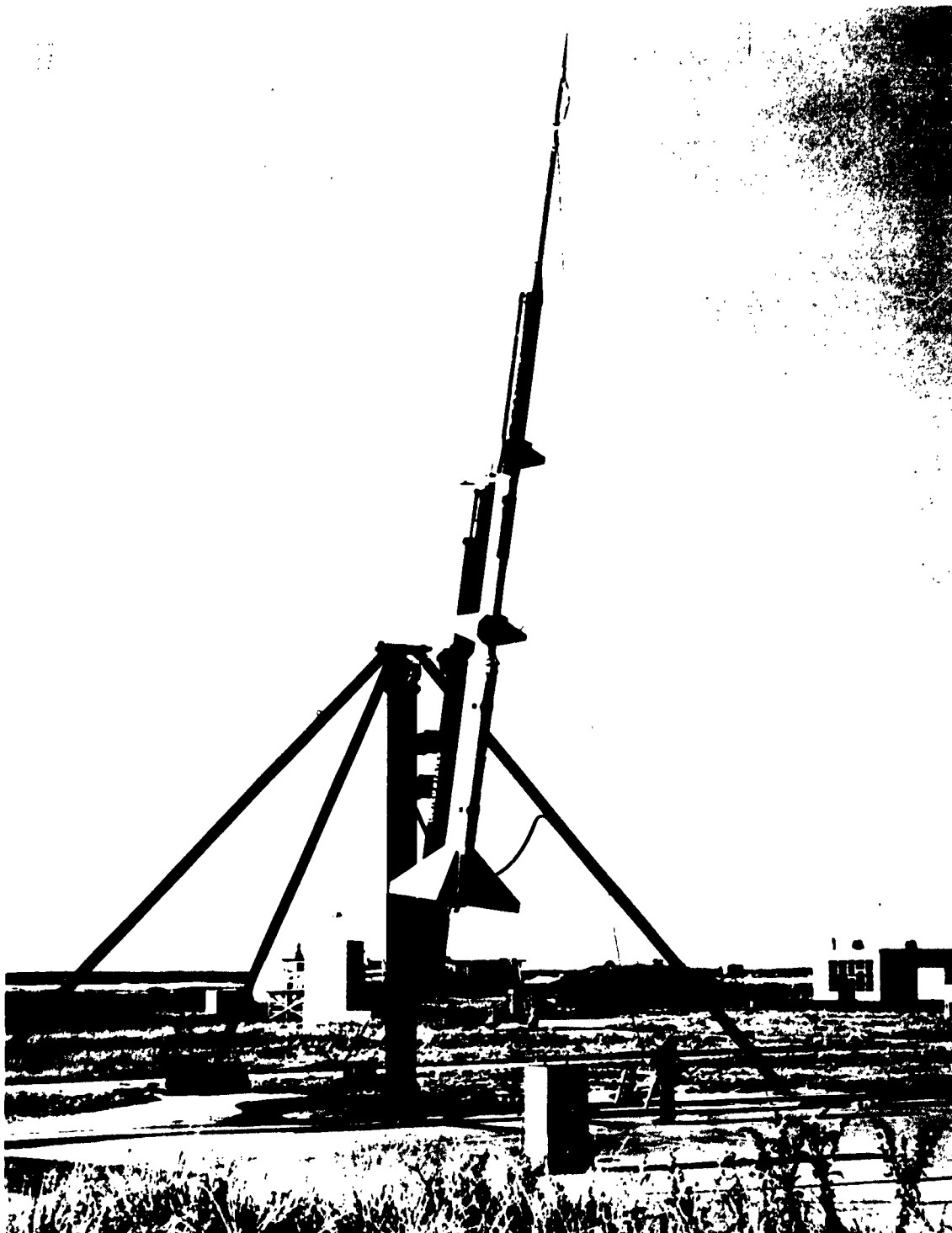
SUMMARY REPORT ON STRONGARM ROCKET MEASUREMENTS OF  
ELECTRON DENSITY TO AN ALTITUDE OF 1500 KILOMETERS

Spence T. Marks  
Charles E. Shafer  
William J. Cruickshank  
Raymond E. Prenatt  
George A. Dulk

Ballistic Measurements Laboratory

RDT & E Project No. 1A011001B021

ABERDEEN PROVING GROUND, MARYLAND



FRONTISPIECE - STRONGARM ROCKET ON LAUNCHER, VERTICAL

BALLISTIC RESEARCH LABORATORIES

REPORT NO. 1187

STMarks/CEShafer/WJCruickshank/  
REPrentiss/GADulk/bj  
Aberdeen Proving Ground, Md.  
January 1963

SUMMARY REPORT ON STRONGARM ROCKET MEASUREMENTS OF  
ELECTRON DENSITY TO AN ALTITUDE OF 1500 KILOMETERS

ABSTRACT

A summary report is presented which covers all phases of a project for the measurement of electron density to an altitude of 1500 kilometers by employing a five-stage solid propellant rocket combination known as the Strongarm, and a two-frequency propagation experiment. Included in the report are sections which describe the theory applicable to the measurements, the rocket vehicle, the airborne instrumentation, the ground instrumentation, the vehicle performance, and the experimental results. An early morning electron density profile to an altitude of 1500 kilometers is presented, together with a daytime and a nighttime profile to 650 kilometers. A model of the ionospheric inhomogeneities which existed during the daytime rocket flight is given. Scale heights and exospheric temperatures derived from the profiles are also presented and discussed.

## TABLE OF CONTENTS

	Page
I. INTRODUCTION. . . . .	9
II. PROJECT OBJECTIVES. . . . .	11
III. THEORY APPLICABLE TO THE MEASUREMENTS . . . . .	13
IV. STRONGARM VEHICLE . . . . .	19
V. AIRBORNE INSTRUMENTATION. . . . .	25
VI. GROUND INSTRUMENTATION. . . . .	41
VII. VEHICLE PERFORMANCE DATA. . . . .	53
VIII. NOSE CONE AND BEACON TEMPERATURE DATA . . . . .	67
IX. ELECTRON DENSITY PROFILES AND INHOMOGENEITIES . . . . .	71
X. DERIVED SCALE HEIGHTS AND EXOSPHERIC TEMPERATURES . . . . .	85
XI. BIBLIOGRAPHY. . . . .	97
XII. APPENDIX. . . . .	99

## LIST OF FIGURES

	Page
Frontispiece - Strongarm Rocket on Launcher, Vertical. . . . .	2
4-1. Strongarm Rocket on Launcher, Horizontal. . . . .	20
4-2. Strongarm Firing Circuit. . . . .	22
5-1. Fifth Strongarm Stage . . . . .	26
5-2. Beacon and Antenna Assembly . . . . .	27
5-3. Beacon Block Diagram. . . . .	28
5-4. Beacon Assembly . . . . .	29
5-5. Oscillator Circuit. . . . .	31
5-6. Oscillator Assembly . . . . .	32
5-7. 37 MC Power Amplifier . . . . .	33
5-8. 148 MC Amplifier and Telemeter Generator. . . . .	34
5-9. Interface Nose Cone Temperature vs Pulse Rate . . . . .	35
5-10. Frequency Variation vs Temperature. . . . .	37
5-11. Temperature Variation of Alloy. . . . .	38
5-12. Beacon Assembly with Foam . . . . .	39
6-1. Ground Stations at Wallops. . . . .	42
6-2. Helical Antenna . . . . .	43
6-3. Cross-Dipole Antenna. . . . .	44
6-4. Ground Station Interior . . . . .	45
6-5. Block Diagram, Ground Station . . . . .	46
6-6. Block Diagram, Receivers. . . . .	48
6-7. Section of Original Chart Recording, Strongarm III. . . . .	50
7-1. Velocity vs Time, Strongarm I . . . . .	54
7-2. Acceleration vs Time, Strongarm I . . . . .	55
7-3. Spin Rate vs Time, Strongarm I. . . . .	56
7-4. Altitude and Range vs Time, Strongarm I . . . . .	58
7-5. Spin Rate vs Time, Strongarm III. . . . .	60
7-6. Altitude and Range vs Time, Strongarm III . . . . .	61
7-7. Z vs Time, Strongarm III. . . . .	62
7-8. Spin Rate vs Time, Strongarm IV . . . . .	64
7-9. Altitude and Range vs Time, Strongarm IV. . . . .	65

	Page
LIST OF FIGURES (Con't)	
7-10. Z vs Time, Strongarm IV. . . . .	66
8-1. Nose Cone Temperatures, Strongarm I, III . . . . .	68
8-2. Beacon Package Temperatures, Strongarm I, III, IV. . . . .	69
9-1. Slow Speed Chart Recording, Strongarm I. . . . .	72
9-2. $N_{max}$ vs Time at Fort Belvoir, Strongarm I Flight . . . . .	73
9-3. Electron Density Profile, Strongarm I. . . . .	74
9-4. Slow Speed Chart Recording, Strongarm III. . . . .	76
9-5. Ionogram Taken at Fort Belvoir, Strongarm III Flight . . . . .	77
9-6. $N_{max}$ vs Time at Fort Belvoir, Strongarm III Flight . . . . .	78
9-7. Electron Density Profile, Strongarm III. . . . .	80
9-8. E Region Electron Density Profile, Strongarm III . . . . .	82
9-9. Electron Density Profile, Strongarm IV . . . . .	83
10-1. Comparison of Strongarm III Profile With Chapman Layers of Constant Scale Height. . . . .	86
10-2. Comparison of Strongarm Profiles With Chapman Distributions. . . . .	89
10-3. Comparison of Strongarm I Sunrise Profile With Typical Daytime and Nighttime Profiles . . . . .	91
12-1. First-to-Second Stage Coupling Unit. . . . .	100
12-2. Second-to-Third Stage Coupling Unit. . . . .	101
12-3. Third-to-Fourth Stage Coupling Unit. . . . .	102
12-4. Fourth-to-Fifth Stage Coupling Unit. . . . .	104



## I. INTRODUCTION

Detailed information on the distribution of free electrons in the ionosphere is of interest to the U. S. Army Materiel Command in connection with its responsibilities for high altitude weapons systems and defense systems against intercontinental ballistic missiles. Information on the distribution of free electrons is desired to the vicinity of the F2 layer maximum at an altitude of approximately 300 km and beyond. These data are needed in a framework of geographical, diurnal, seasonal, and secular variations.

A trajectory comparison method for obtaining electron densities from Doppler Velocity and Position (DOVAP) data was devised at the Ballistic Research Laboratories as early as 1950. In this method, the DOVAP trajectory obtained for a rocket flight was compared with a vacuum trajectory. A small program was initiated at the time to obtain electron density data from V-2, Viking, and Bumper rounds fired at White Sands Missile Range. The V-2 and Viking rounds attained altitudes ranging from 160-240 km, while one of the Bumper rounds (Bumper V) reached an altitude of 400 km. Fragmentary electron density data were obtained from these firings.<sup>1,2,3,4</sup>

At the close of the International Geophysical Year (IGY), which terminated on December 31, 1958, the IGY rocket firings were screened, and it appeared that the DOVAP data from approximately twenty-five of the firings might be suitable for electron density reduction purposes. Closer examination reduced the number of suitable rounds to ten, three being Nike-Cajuns, six Aerobee Hi's, and one a Spaerobee. The Nike-Cajuns and Aerobee-Hi's attained altitudes ranging from 130-190 km, while the Spaerobee (ABM10.200) reached 280 km. Improved methods for handling the data were developed, suitable computer routines were worked out and good electron density data were obtained from these rounds. However, only one round approached the F2 maximum.<sup>5</sup>

It was therefore decided after the IGY that a further effort should be made to measure electron density profiles to high altitudes. A new solid propellant rocket combination, known as the Strongarm, was assembled for this purpose by the University of Michigan under contract to the Ballistic Research Laboratories.

This rocket combination consisted of five stages:

1. Honest John
2. Nike
3. Nike
4. Yardbird
5. Scale Sergeant

The theoretical altitude capability of this rocket combination with a 10 kg payload was 1500 km.

A VHF propagation experiment was designed for use with the Strongarm rocket. A technique similar to that devised by Seddon<sup>6</sup> was employed; however, the frequencies used were 37 mc and 148 mc, which greatly simplified the equipment design and the data analysis. The use of two frequencies eliminated the need for the extremely accurate vacuum trajectories required by the trajectory comparison method.

Five Strongarm rockets with this propagation experiment were fired by the University of Michigan for the Ballistic Research Laboratories from the NASA launching facility at Wallops Island, Virginia, during November 1959 and July 1960. The results obtained from these firings are given in this report.

Officially designated as the OB11.01, OB11.02, OB11.03, OB11.04 and OB11.05, these rockets are referred to in this report as the Strongarm I, Strongarm II, Strongarm III, Strongarm IV, and Strongarm V., respectively.

## II. PROJECT OBJECTIVES

### A. Primary

1. The region in the vicinity of the F2 maximum at an altitude of 300 km and beyond was relatively unexplored at the time that the Strongarm project was initiated. Thus, it was desired to make rocket measurements of electron density through this region, the objective being to establish electron density profiles to altitudes at least twice as high as the F2 maximum, or higher if possible.

2. It was also desired to make a comparison of daytime and nighttime electron density profiles to the same altitudes, the optimum observation times being approximately noon and midnight when the ionosphere approaches its most stable condition. This comparison was of interest because of its application to studies of the ionization and de-ionization processes in the atmosphere.

3. A further objective was to compare the measured electron density profiles with Chapman profiles, to derive scale heights from the electron density profiles, and to deduce exospheric temperatures from the scale heights.

### B. Secondary

1. It was desired to accomplish these objectives by using a combination of "off-the-shelf" solid propellant rocket units, so that procurement times would be short and the cost of the rocket development work would be relatively low.

2. There was the possibility, also, that the development of this solid propellant rocket combination would result in a low cost vehicle which could be used by other research organizations for making high altitude measurements.

### III. THEORY APPLICABLE TO THE MEASUREMENTS

#### A. Design of the Experiment

A technique for determining ionosphere electron density and integrated electron content by measuring the effect of the ionosphere on radio signals transmitted from sounding rockets has been described by Berning,<sup>1, 2, 3, 4</sup> and was applied to a number of rocket flights during the International Geophysical Year.<sup>5</sup> The measurements were accomplished by comparing the rocket altitudes measured by a DOVAP tracking system with those from a computed vacuum trajectory. Differences between the two trajectories were then attributed to the effect of the ionosphere on the DOVAP signals. An advantage of this so-called trajectory comparison technique was that it permitted ionospheric measurements to be made as a by-product of the DOVAP tracking data and required no additional rocket payload. However, the technique suffered from a number of limitations. It could only be applied at firing ranges instrumented with a complete, multistation DOVAP system and it required extremely careful determination of the DOVAP trajectory. In addition, it required a very accurate vacuum trajectory determination, a process that becomes increasingly difficult when applied to rocket flights which attain higher and higher peak altitudes.

Ionosphere measurements with the Strongarm rocket series were made using a variation of the two-frequency propagation experiment described by Seddon.<sup>6</sup> This experiment uses two harmonically related, phase coherent frequencies transmitted from a rocket-borne beacon to a ground station. Ionosphere measurements are accomplished by comparing the phase of a low frequency whose propagation is strongly affected by the ionosphere with the phase of a considerably higher reference frequency that is relatively unaffected by the ionosphere. The frequencies used by BRL were approximately 37 and 148 megacycles. The choice of a low frequency of 37 megacycles rather than the more sensitive 6-8 megacycle frequency used by Seddon resulted from the following considerations:

1. There is a significant decrease in man-made interference above approximately 30 megacycles,
2. A more compact beacon and antenna design is possible and lower transmitted powers can be used,
3. The 37 mc frequency is well above the ionospheric critical frequency so that no difficulties arise from signals reflected from the ionosphere even at fairly large zenith angles,

4. Refraction of the signals is so slight that straight line propagation can be assumed in the analysis, and

5. At 37 mc, approximations to the Appleton-Hartree expression for index of refraction are possible that greatly simplify the analysis.

The phase of an rf signal received from a rocket-borne radio beacon can be expressed by

$$\phi_1 = f_1 t - \int_0^r \frac{f_1}{c} dr \quad (1)$$

where  $\phi$  is the phase in cycles,  $f_1$  is the transmitted frequency,  $dr$  is an element of distance along the ray path, and  $c$  is the propagation velocity, which may vary along the ray path. The second term on the right hand side of equation (1) is the phase path between the rocket and receiver.

Neglecting electron collisions and magnetoionic effects the index of refraction can be expressed by

$$\eta = \sqrt{1 - \frac{N_e e^2}{4\pi^2 f_1^2 \epsilon_0 m}} = \sqrt{1 - \frac{80.6 N_e}{f_1^2}} \doteq 1 - \frac{40.3 N_e}{f_1^2} \quad (2)$$

where  $N_e$  is the electron density,  $\epsilon_0$  is the permittivity of free space, and  $e$  and  $m$  are the charge and mass of the electron respectively.

Substituting  $c = \frac{c_0}{\eta}$  in equation (1) the phase of the received signal becomes

$$\phi_1 = f_1 t - \frac{f_1}{c_0} \int \eta dr = f_1 t - \frac{f_1}{c_0} \int \left(1 - \frac{40.3 N_e}{f_1^2}\right) dr \quad (3)$$

which can be rewritten

$$\phi_1 = f_1 t - \frac{f_1 r}{c_0} + \frac{40.3}{f_1 c_0} \int N_e dr \quad (4a)$$

The first two terms on the right hand side represent the phase that would be observed in the absence of an ionosphere. The amount that the phase is changed by the presence of the ionosphere is seen, in the last term, to be inversely proportional to the propagated frequency and directly proportional to the integrated electron content along the ray path.

If a second frequency,  $f_2 = Kf_1$ , is also transmitted, its phase is

$$\phi_2 = f_2 t - \frac{f_2 r}{c_0} + \frac{40.3}{f_2 c_0} \int N_e dr \quad (4b)$$

If the phase of the lower frequency signal is multiplied by K and subtracted from that of the higher frequency signal, the phase difference is

$$\phi_2 - K \phi_1 = \phi_{dd} = -(K^2 - 1) \frac{40.3}{f_2 c_0} \int N_e dr \quad (5)$$

and its time rate of change, called the dispersive Doppler frequency is

$$\frac{d \phi_{dd}}{dt} = f_{dd} = -(K^2 - 1) \frac{40.3}{f_2 c_0} \frac{d}{dt} \int N_e dr \quad (6)$$

The integrated dispersive Doppler,  $\phi_{dd}$ , is thus shown to be a measure of the integrated electron content along the ray path and the dispersive Doppler frequency,  $f_{dd}$ , to be a measure of the rate of change of integrated electron content.

In practice, the required multiplication and differencing is done electronically at the receiving station and the dispersive Doppler frequency presented directly on a chart record. This procedure is described in greater detail in succeeding sections. Integrated dispersive Doppler is tabulated at one second intervals by counting the dispersive Doppler cycles from the chart with interpolations being made through poor quality sections of the record.

A second method of determining the integrated dispersive Doppler makes use of the BRL Transistorized Data Translator (TDT). Originally designed for use in reducing DOVAP tracking data, the TDT counts and accumulates the cycles that make up the audio frequency output from each tracking filter. Cycle count readout occurs at a rate of one per second. This method of data reduction is accomplished after the flight from magnetic tape playbacks. Accurate time alignment is effected using timing signals that are also recorded on the tape. The required multiplication and differencing to obtain dispersive Doppler is accomplished using a digital computer.

## B. Method of Analysis

The changes in integrated electron content along the ray path which produce the observed dispersive Doppler frequency arise from three sources:

1. Changes in the path length, due to radial motion of the rocket, the effect of which on the dispersive Doppler frequency is proportional to the electron density at the rocket,
2. Changes in electron density along the ray path due to either
  - a. Changes in the direction of the ray arising from transverse motion of the rocket i.e., changes in obliquity or,
  - b. Departure from quasi-stationary conditions in the ionosphere.

It is not possible, by observation of the dispersive Doppler alone, to separate these effects and therein lies one of the chief difficulties in using propagation experiment data to obtain electron density profiles. A technique for applying the necessary corrections has been outlined by Berning, and was used in a preliminary reduction of the dispersive Doppler data from Strongarm I.<sup>7</sup> A different technique, described below, was used in the final analysis of the Strongarm series.

For a horizontally stratified ionosphere where the electron density has no horizontal gradient, the integrated electron content can be rewritten.

$$\int N_e dr = \int N_e \sec \theta dh \quad (7)$$

where  $\theta$  is the angle between the ray path and the zenith. If a single effective value for  $\theta$  is used, the integrated electron content in a vertical column (hereafter called "vertical content") can be computed from the expression

$$\int N_e dh = - \frac{f_o^2 c_o \cos \theta}{40.3 (K^2 - 1)} \phi_{dd} = 7.36 \times 10^{13} \phi_{dd} \cos \theta \frac{\text{electrons}}{\text{meter}^2} \quad (8)$$

The use of the appropriate values of  $\cos \theta$  for successive rocket positions effectively eliminates the contribution of the changing zenith angle to the observed dispersive Doppler and constitutes the necessary obliquity correction.

• If the electron density at altitudes below the rocket were unchanging with time so that changes in vertical content were due solely to changes in rocket position, then the local electron density at the rocket could be computed directly from the expression

$$\bar{N}_e = \frac{\left[ \int_0^{h_{i+1}} N_e dh \right] - \left[ \int_0^{h_i} N_e dh \right]}{h_{i+1} - h_i} = \frac{\Delta \int N_e dh}{\Delta h} \quad (9)$$

where  $h_i$  and  $h_{i+1}$  are successive altitudes and  $\bar{N}_e$  is the average electron density in the altitude interval between  $h_i$  and  $h_{i+1}$ . The assumption of such a constant ionosphere is often not possible, especially near sunrise and sunset or when the rocket is at an altitude considerably above the  $F_{\max}$  where the electron density and rocket velocity are relatively low. Under these conditions the effect of temporal changes in ionization beneath the rocket can make a significant contribution to the observed changes in vertical content at successive altitudes throughout the flight. As a result, a "no-elapsd-time" vertical content profile is computed and used in turn to compute the electron density as described above. To compute the no-elapsd-time profile, the vertical content is assumed to be proportional to the F2-maximum electron density ( $N_{\max}$ ) so that

$$\frac{\left[ \int N_e dh \right]_{t_0}}{\left[ \int N_e dh \right]_{t_1}} = \frac{\left[ N_{\max} \right]_{t_0}}{\left[ N_{\max} \right]_{t_1}} \quad (10)$$

where  $t_0$  is some reference time during the rocket flight and  $t_1$  is any other time. This proportionality between  $F_{\max}$  electron density and integrated electron content is a property of a simple Chapman model as discussed by Wright.<sup>12</sup>  $N_{\max}$  versus time variations can be obtained from ionograms taken at nearby ionosphere stations.



A program has been coded for both the ORDVAC and BRLESC computers whose input consists of tabulated values of integrated dispersive Doppler, rocket position, and F2 maximum electron density. The outputs from the program include the no-elapsed time vertical content profile computed from

$$\left[ \int_0^{h_i} N_e dh \right]_{t_0} = 7.36 \times 10^{15} \phi_{dd} \left[ \frac{N_{max}}{N_{max}} \right]_{t_1}^{t_0} \cos \theta \quad (11)$$

and the electron density profile computed from equation (9).

#### IV. STRONGARM VEHICLE\*

##### A. Design Considerations

The principal design consideration for the Strongarm vehicle was the selection of a solid propellant rocket combination that would have the desired altitude capability, and be readily available "off-the-shelf" at relatively low cost.

At the same time, it was anticipated that aerodynamic heating of the upper stage fins and last rocket stage would be a design problem since the high velocities of the upper stages would undoubtedly be attained at altitudes where the air density would still be appreciable.

##### B. Strongarm Components

A five-stage solid propellant rocket combination, 56.5 feet long, and weighing 7125 pounds, was designed by the University of Michigan for the purpose. A photograph of the Strongarm rocket on the launcher is shown in Figure 4-1.

The first rocket stage was an Honest John Booster, designated M-6A1, which was used with the M-35 igniter. This rocket stage weighed 4080 pounds, and had a thrust of 80,000 pounds. The regular Honest John fins were employed, but their cant was eliminated to reduce spin to a minimum.

The second and third rocket stages were Nike-Hercules booster units, designated M5E1's, which were used with M-24E1 igniters. Each of these rocket stages weighed 1280 pounds, and had a thrust of 42,500 pounds. The regular Nike three-fin assemblies were replaced by four-fin assemblies on these stages, the second stage fins having an area of 2.5 square feet each, and the third stage fins an area of 2.0 square feet each. One inconel cuff, 0.031 inch thick and 1-1/2 inches wide, was provided for the leading edges of the second stage fins. The third stage fins had two inconel cuffs on their leading edges, one thickness being 0.031 inch, and the other 0.062 inch.

---

\* English units are used in this section and the Vehicle Performance section in accordance with the current practice in the rocket industry. However, the experimental data in this report are given in metric units to conform with the practice in the scientific community.

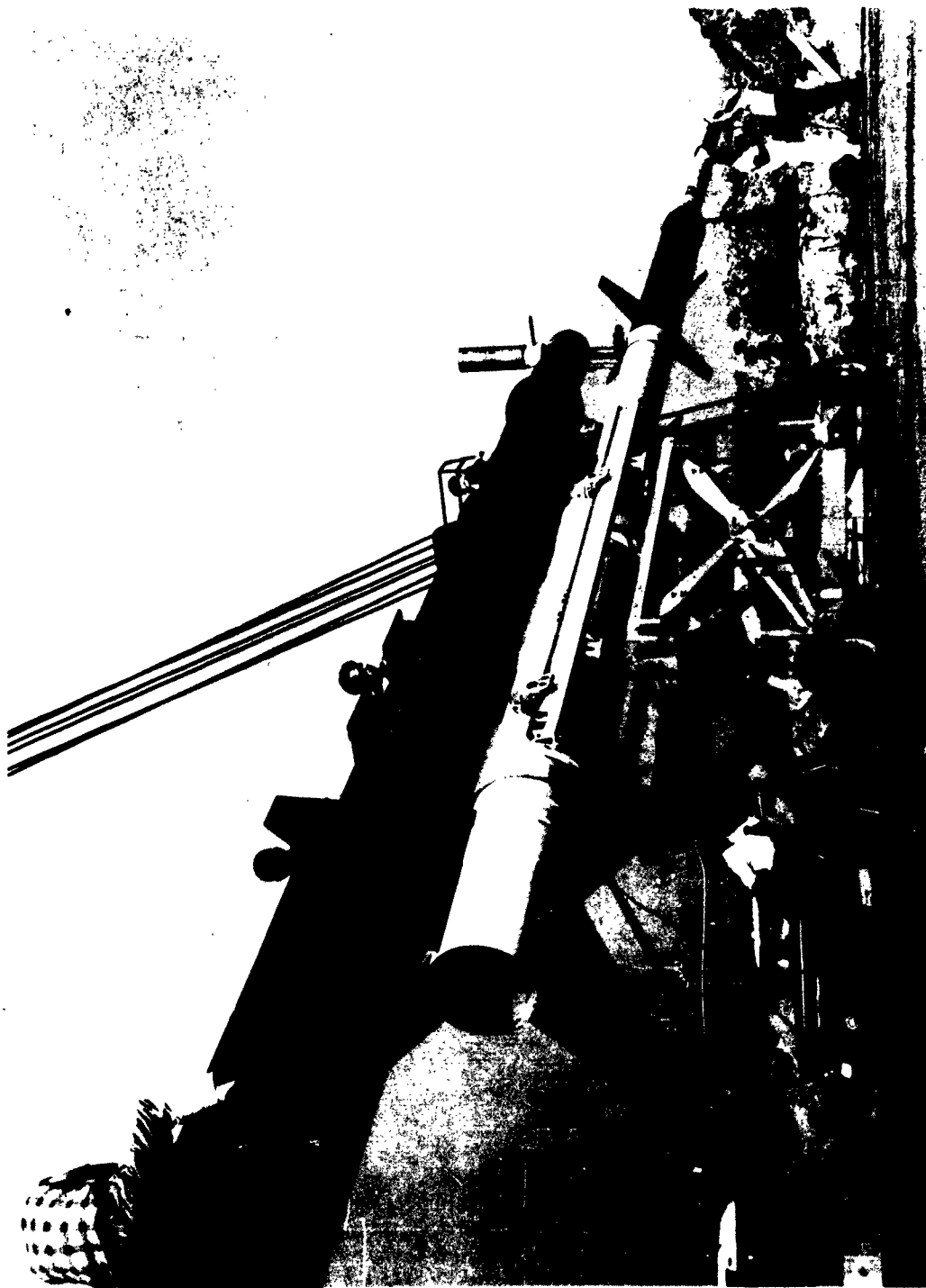


FIG. 4-1. STRONGARM ROCKET ON LAUNCHER, HORIZONTAL

The fourth rocket stage was a modified Recruit rocket called the Yardbird.\* This rocket stage weighed 400 pounds, and had a thrust of 19,600 pounds. It was stabilized by a flared skirt whose thickness was sufficient to provide an adequate heat sink through fourth stage burning.

The fifth and final stage was a Scale Sergeant rocket.\*\* This rocket stage weighed 85 pounds, and had a thrust of 1900 pounds. The steel rocket casing of this stage was coated with a 50 mil layer of Teflon, having an ablation temperature of 1100°F, to prevent excessive heating of the rocket propellant prior to ignition. This rocket stage was also stabilized by a flared skirt, which was composed of a new high temperature magnesium alloy, designated HK31A, that was capable of withstanding fifth stage burning.

A 1/8 inch thick fiberglass nose cone was employed on the fifth rocket stage, with an 80 mil Teflon overlay to prevent excessive heating of the nose cone. The nose cone tip consisted of a steel core with a Teflon coating varying from 3/4 to 5/16 inch in thickness.

#### C. Firing Circuit

The Strongarm firing circuit is shown in Figure 4-2. The first, second and third stage firing lines were connected in parallel, an instantaneous igniter being used in the first stage, a 7 second delay igniter in the second stage, and a 25 second delay igniter in the third stage. A two-inch movement of the first stage had to occur before the second and third stage firing lines could receive current. Thus, in the event that a first stage misfire were to occur the second and third stages would not ignite. The fourth and fifth stage igniters were to receive current from batteries carried in these stages when pressure sensitive switches closed upon the decay of the chamber pressures in the preceding stages.

#### D. Predicted Performance

The first stage was to drag separate after burning for 4.37 seconds. The second stage was to ignite approximately 2.0 seconds later, burn for 3.0 seconds, and drag separate after the second-to-third stage locking device was released by

---

\* Manufactured by the Thiokol Chemical Corporation, Elkton, Maryland.

\*\* Manufactured by the Jet Propulsion Laboratory, Pasadena, California.

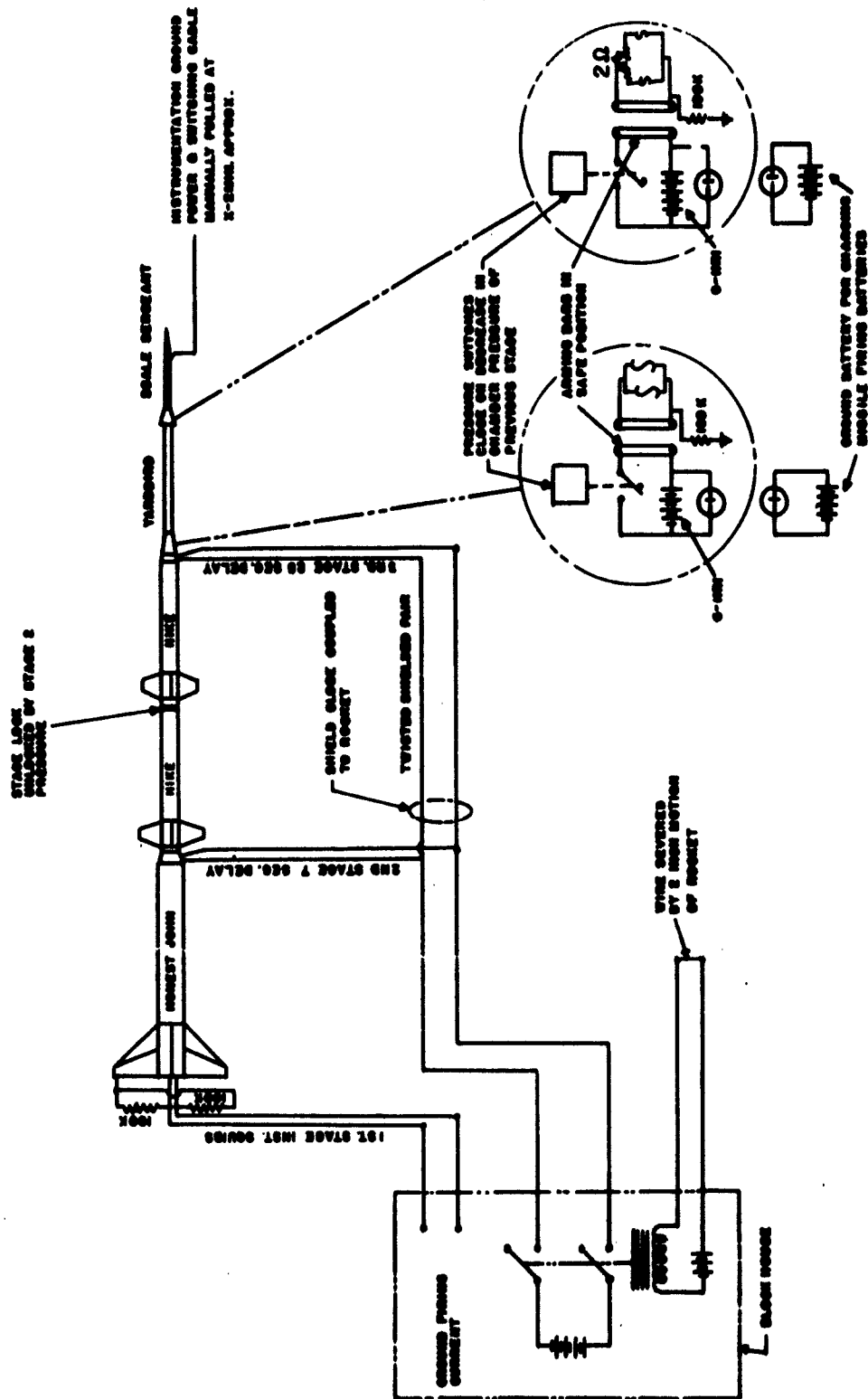


FIG. 4-2. STRONGARM FIRING CIRCUIT.

the decay of the chamber pressure in the second stage. A coast period of approximately 15 seconds was to follow. The third stage was then to ignite and burn for 3.0 seconds. The pressure decrease at burnout of the third stage was to trigger the ignition of the fourth stage, which was to burn for 3.25 seconds. Similarly, the decrease of pressure in the fourth stage was to trigger the ignition of the fifth stage, which was to burn for 6.25 seconds.

At the end of the powered flight phase (after 35.8 seconds), the fifth Strongarm stage was to be at an altitude of 178,000 ft. and have a velocity of 17,500 ft/sec. The fifth stage was then to coast upward, and attain a peak altitude of approximately 1000 miles. The predicted ground range of the fifth stage for an elevation angle of  $80^{\circ}$  was approximately 800 miles.

## V. AIRBORNE INSTRUMENTATION

### A. Airborne System

The airborne instrumentation of the Strongarm rocket was located in the nose cone of the 5th stage. A closeup view of this stage is shown in Figure 5-1. The instrumentation consisted of a two-frequency beacon, a telemeter, and associated antennas, as shown in Figure 5-2.

The two-frequency beacon was designed by the University of Michigan to satisfy the following ERL specifications: A 100 mw transmitter at 36.94 mc; a 20 mw transmitter at exactly four times 36.94 mc and phase coherent with it; both frequencies being derived from a common oscillator with a frequency stability of one part in  $10^6$  over a 30 minute period. A telemeter generator was added to the beacon to amplitude modulate the 147.76 mc signal with nose cone temperature information.

The nose cone antennas were trapezoidal loops perpendicular to each other. The radiation pattern of each antenna was omnidirectional in the plane of the loop. Both antennas used current fed loops and were temperature compensated in the tuning capacitors. Efficiencies of the antennas were 16 db below dipole for 36.94 mc and 2 db below dipole for 147.76 mc.

### B. Beacon Design

A block diagram of the beacon is shown in Figure 5-3, and the beacon assembly is shown in Figure 5-4. It consisted of the following parts:

- (a) A 36.94 mc crystal oscillator powered by a separate battery.
- (b) A three stage 36.94 mc amplifier driven by the oscillator and delivering 100 mw to the 36.94 mc antenna.
- (c) Two frequency doublers and a final amplifier driven by the second stage of the 36.94 mc amplifier and delivering 20 mw to the 147.76 mc antenna.
- (d) A telemeter generator to amplitude modulate the 147.76 mc signal.
- (e) A Ledex stepping switch to: (1) operate the 36.94 mc amplifier on external power; (2) operate the 147.76 mc amplifier on external power; (3) operate both amplifiers on external power; and (4) switch both amplifiers to internal power.

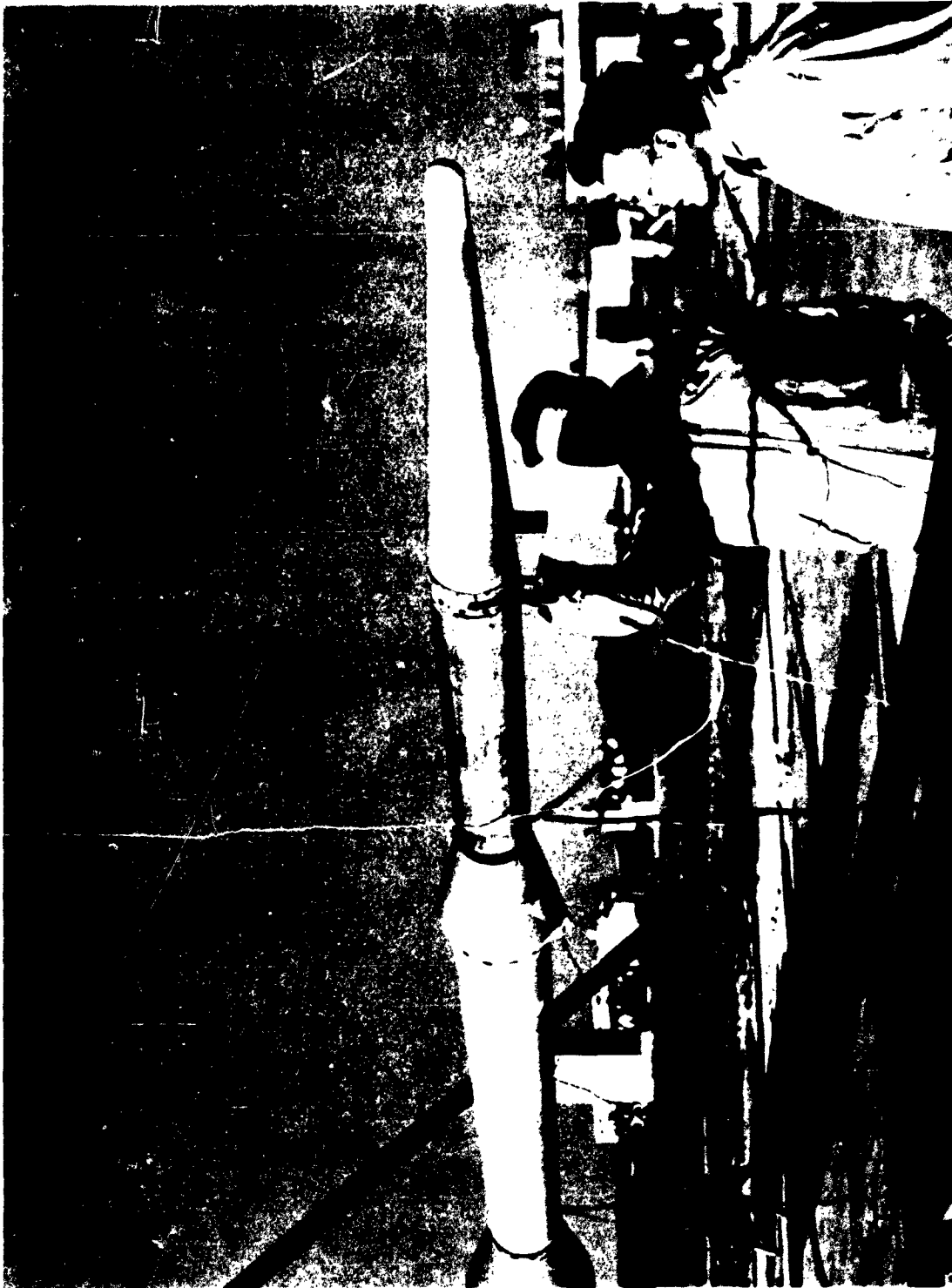


FIG. 5-1. FIFTH STRONGARM STAGE





FIG. 5-2. BEACON AND ANTENNA ASSEMBLY

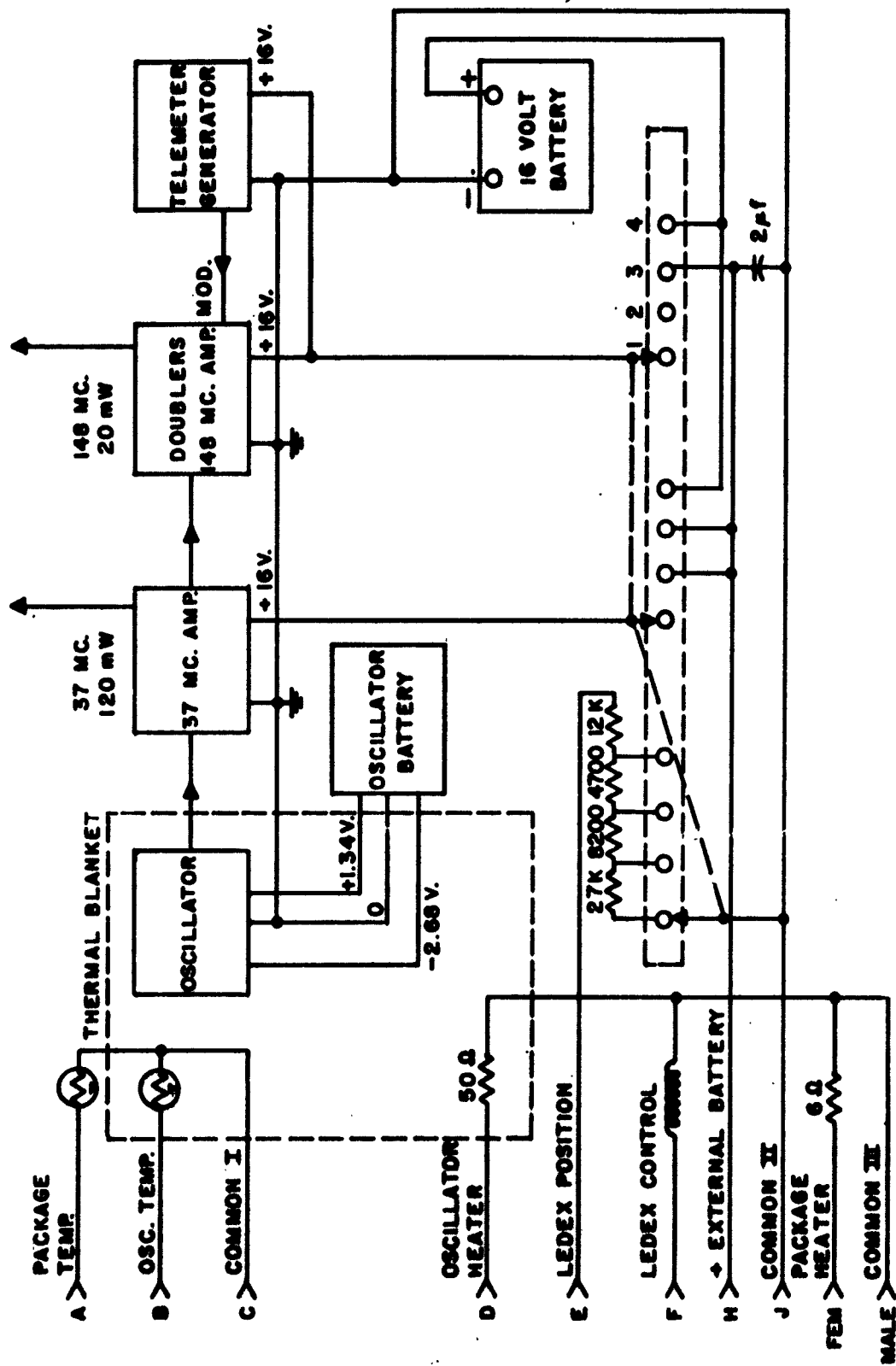


FIG. 5-3 BEACON BLOCK DIAGRAM

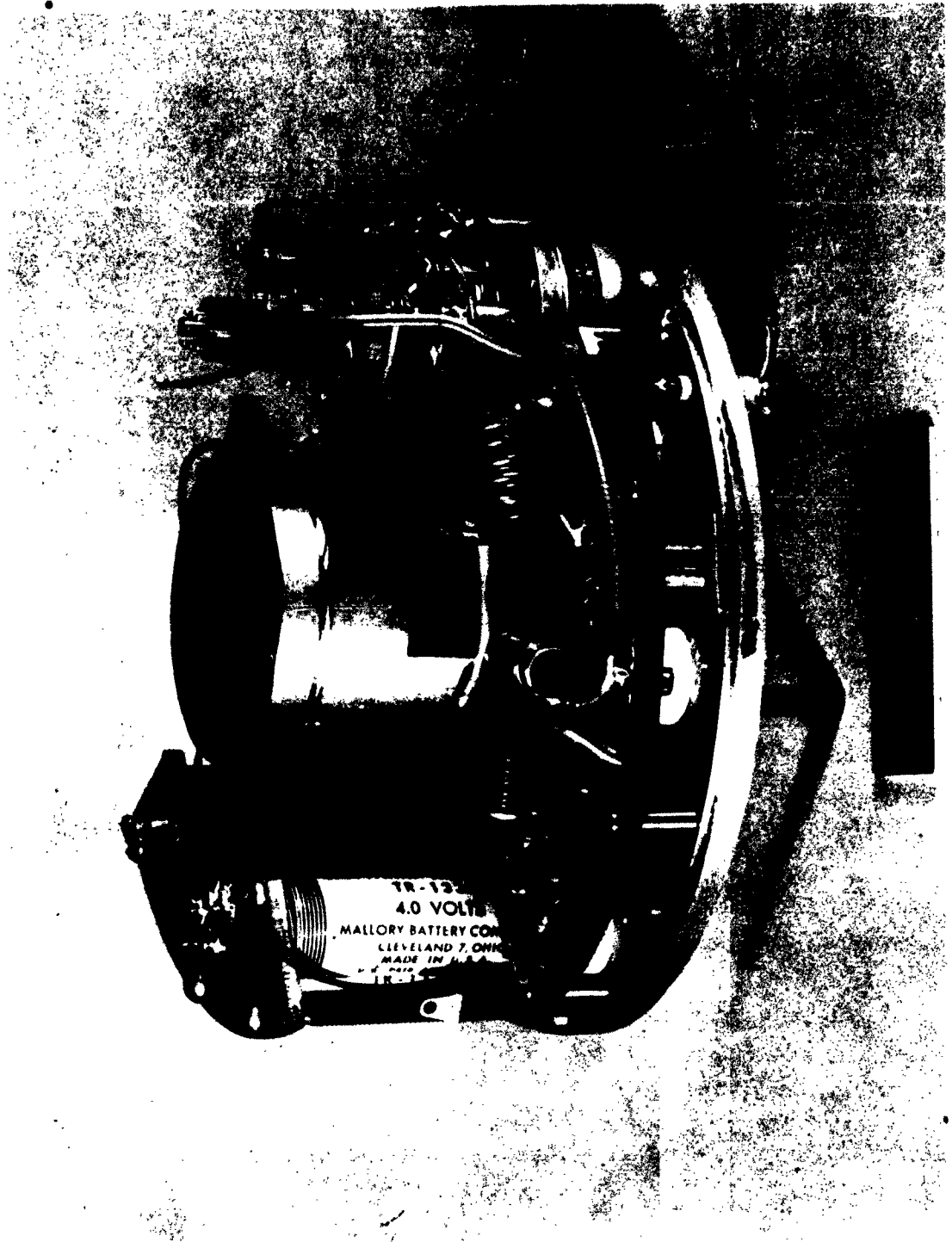


FIG. 5-4. BEACON ASSEMBLY

(f) A battery pack for powering the oscillator and amplifiers.

(g) Two VECO-32A84 thermistors for measuring package and oscillator temperature while the rocket was on the launcher.

(h) One VECO-61A7 thermistor for measuring temperature at the interface between the Teflon and Fiberglas of the nose cone during flight.

(i) A 12 watt oscillator heater.

(j) A 100 watt package heater.

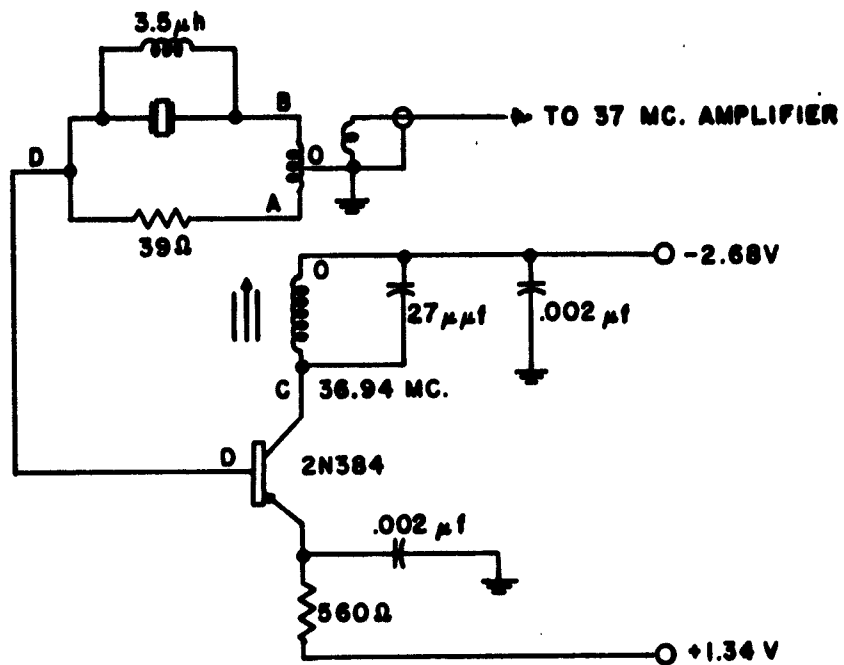
#### C. Oscillator Design

The oscillator circuit is shown in Figure 5-5; and the oscillator assembly is shown in Figure 5-6. The transistor crystal-controlled oscillator was mounted within one section of an aluminum container. A eutectic alloy occupied the other section. The container was enclosed in an insulating blanket of foamed resin. The heat-of-fusion method used to temperature stabilize the oscillator is explained in subsection E below. The voltage was held constant by using a separate battery to power the oscillator and by designing the circuit for low power output. Approximately 200 microwatts were coupled to the 36.94 mc amplifier.

#### D. Amplifiers and Telemeter Generator

Schematics of the 36.94 mc and 147.76 mc amplifiers are shown in Figures 5-7 and 5-8.

Telemetry was added to the beacon to measure: (1) the temperature at the interface of the Teflon and fiberglas on the nose cone, and (2) the temperature of the beacon package. The telemeter generator was a free running multivibrator. This circuit is shown in Figure 5-8. The pulsating current drawn through the 390 and 470 ohm resistors was used to amplitude modulate the 148 mc carrier. The pulse rate was determined by the resistance of the 61A7 thermistor which was bonded to the nose cone interface. Figure 5-9 shows the interface nose cone temperature versus pulse rate. A temperature fuze was employed in the beacon package to turn off the telemetry when a temperature of 47° C was reached, thus providing a one-point measurement of the temperature inside the beacon during flight.



**COIL DATA:**

COLLECTOR WINDING 7 TURNS  
 FEEDBACK WINDING 2 TURNS C.T.  
 OUTPUT WINDING 1 TURN  
 OUTSIDE DIA.  $\frac{5}{16}$  ; #28 ENAMEL WIRE

**XTAL DATA:**

SERIES RESONANT 36.94000  
 3RD OVERTONE  
 TURNING POINT  $45^{\circ}\text{C} \pm 1^{\circ}\text{C}$

**FIG. 5-5 OSCILLATOR CIRCUIT**

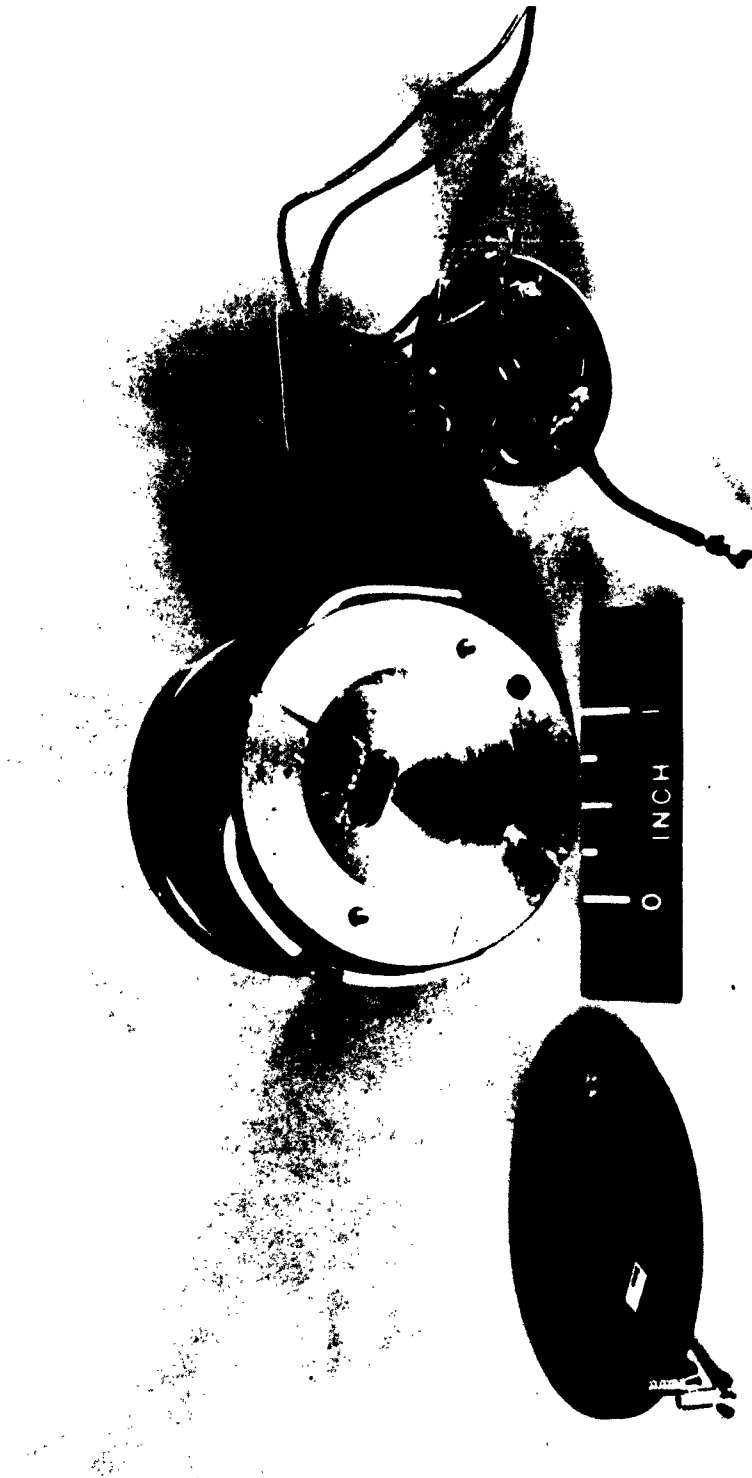
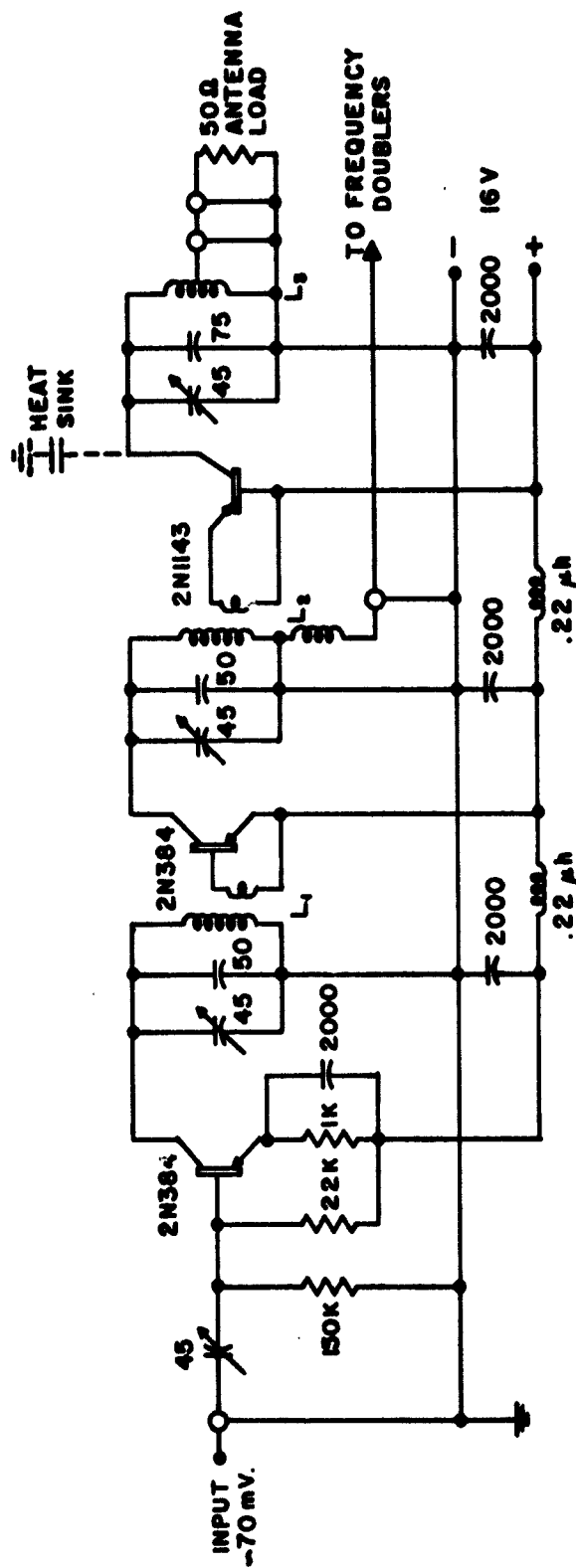


FIG. 5-6. OSCILLATOR ASSEMBLY



ALL CAPACITOR VALUES IN  $\mu$ f

- L<sub>1</sub> PRIMARY 8 TURNS ; SECONDARY 2 TURNS INTERLACED WITH PRIMARY  $\frac{1}{4}$  COIL FORM ; #20 ENAMEL WIRE.
- L<sub>2</sub> IDENTICAL WITH L<sub>1</sub> ; THIRD WINDING 5 TURNS #26 ENAMEL WIRE.
- L<sub>3</sub> 4 TURNS #12 BARE COPPER WIRE ; TAP 1 TURN FROM END. INSIDE DIAMETER  $\frac{1}{2}$ "

FIG. 5-7 37 MC. POWER AMPLIFIER

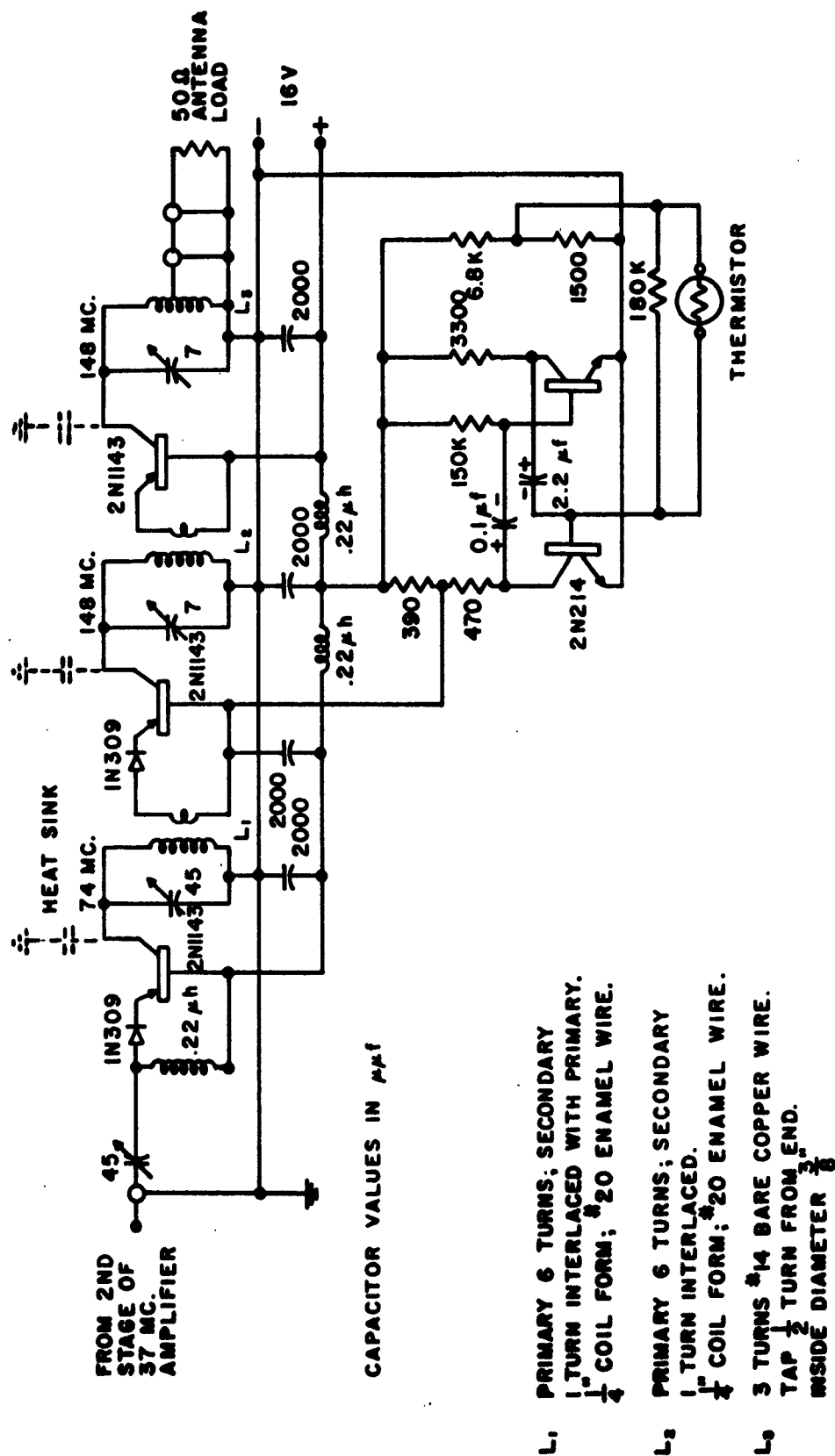
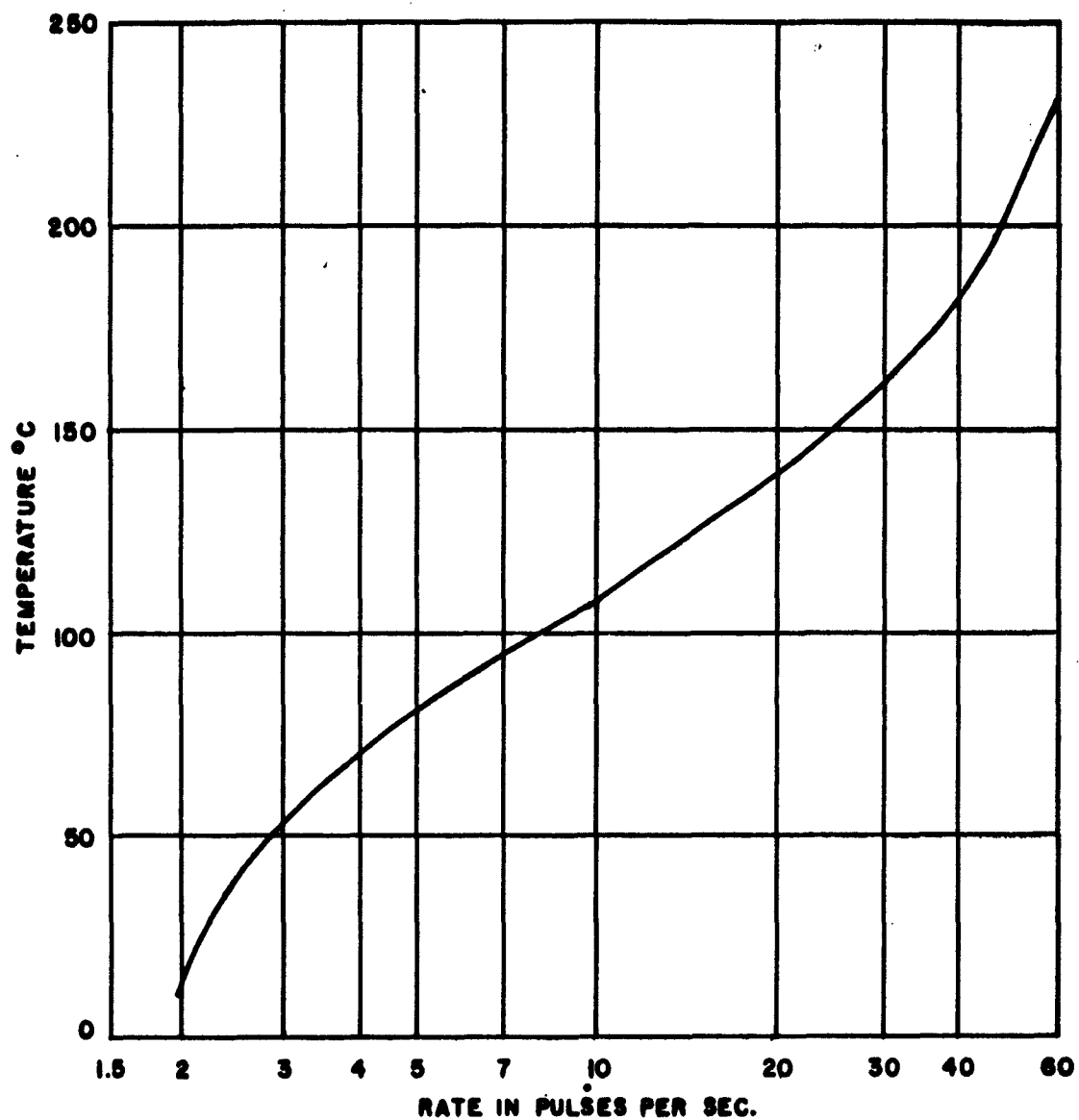


FIG. 5-8 148 MC. AMPLIFIER AND TELEMETER GENERATOR





**FIG. 5-9 INTERFACE NOSE -CONE TEMPERATURE VS PULSE RATE.**

#### E. Thermal Design

The frequency stability of the oscillator was a function of the temperature coefficient of the crystal. Figure 5-10 shows the frequency variation of the crystal and the complete circuit when heated separately. Crystals having turning points close to  $47^{\circ}\text{C}$  were temperature stabilized at  $47^{\circ}\text{C}$  by use of the heat-of-fusion method. If the liquid and solid phases of a pure material are present in thermal equilibrium, the temperature remains at the melting point regardless of the direction of heat flow. A eutectic alloy (Cerrolow 117) having a melting point at  $47^{\circ}\text{C}$  was used for this purpose. Three hundred grams of alloy were enclosed in a thermal blanket of foam plastic. The alloy was melted and then allowed to cool in a room, temperature ambient  $25^{\circ}\text{C}$ . Rate of heat loss for these conditions was approximately 16 calories/min/ $^{\circ}\text{C}$ . Under these conditions the rate of temperature change of alloy was  $\approx 0.1^{\circ}\text{C}/\text{min}$ . Figure 5-11 shows the temperature variation of the sample of partially melted alloy. Oscillator frequencies stable to 1 part in  $10^8$  were obtained by this method in the laboratory. One-third of the alloy was melted prior to launch to compensate for the heat losses during the first minute of flight, and the solid alloy remaining absorbed any heat gain thereafter, resulting in a near-constant oscillator temperature.

The 2N1143 transistors were heat-sinked to the aluminum chassis through 0.020 inch thick Teflon sheet.

The proper temperature for battery operation ( $5^{\circ}$ - $75^{\circ}\text{C}$ ) was achieved by use of 100 watt heater ribbon wound on the outside of the package cover, as shown in Figure 5-12. This figure also shows the foamed plastic blanket surrounding the oscillator.

#### F. Temperature Measurements and Control

Temperature circuits in the ground station control console were connected to the 32A84 thermistors in the beacon for monitoring package and oscillator temperatures while the rocket was on the launcher. The package and oscillator heaters were regulated from the console prior to launch.

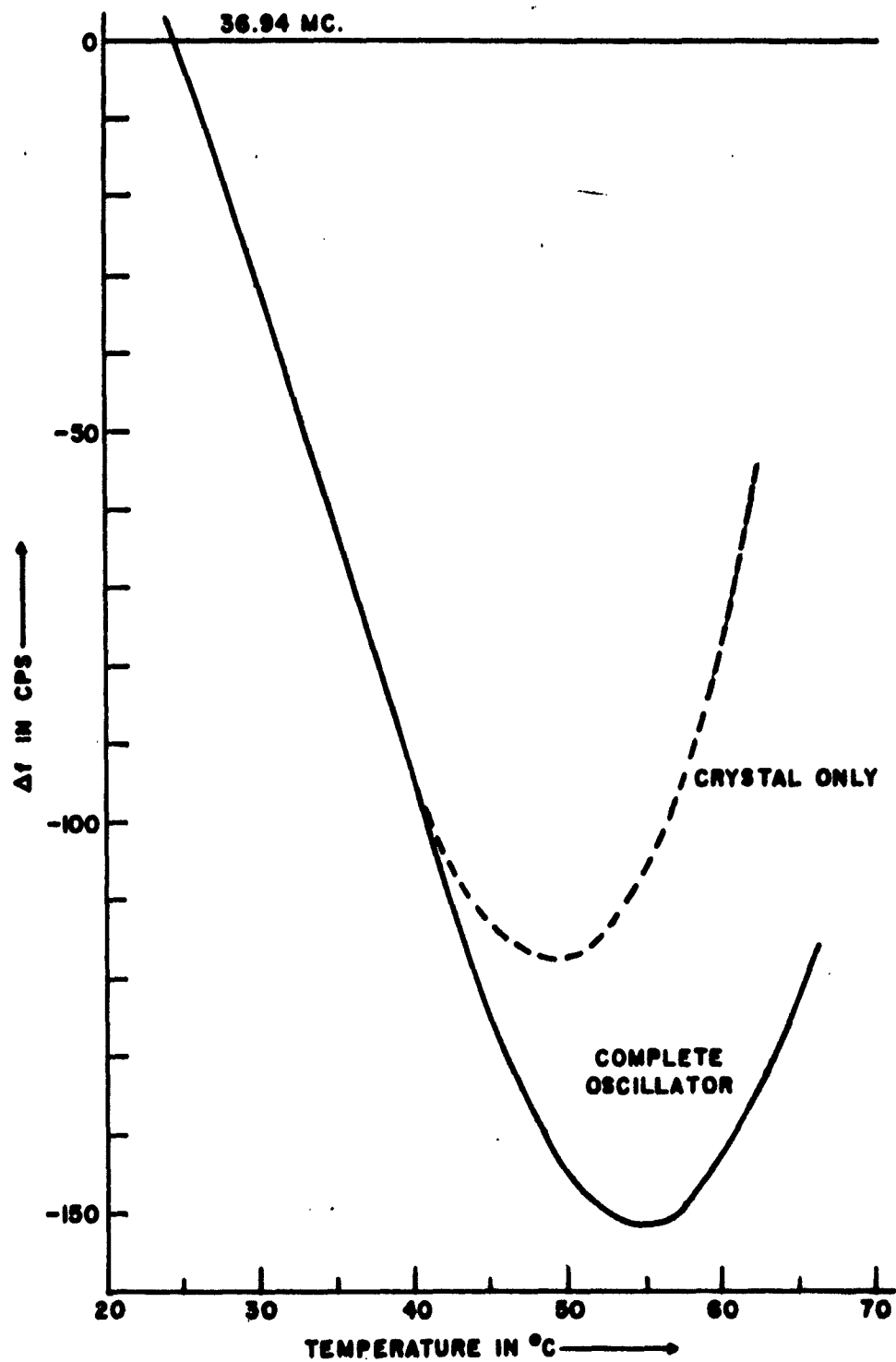
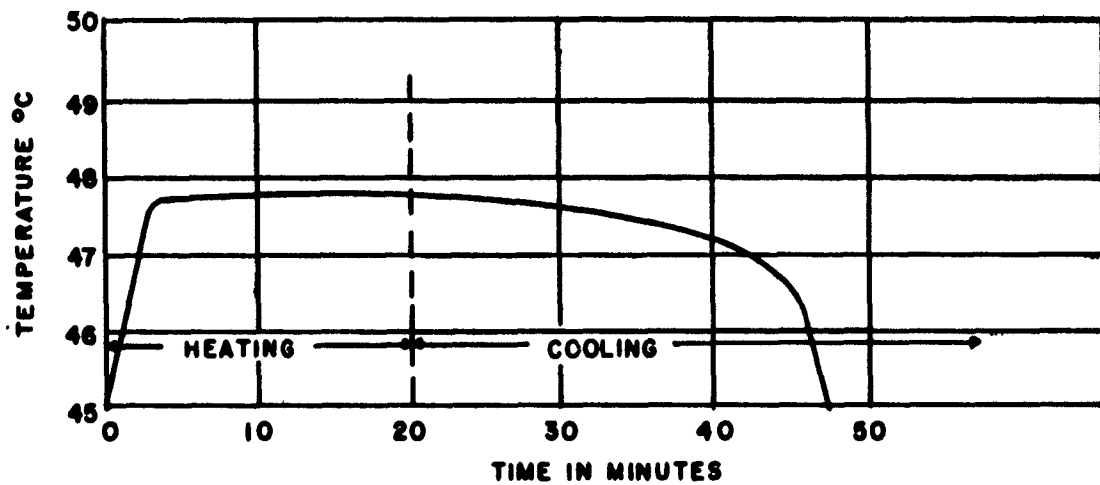


FIG. 5-10 FREQUENCY VARIATION VS TEMPERATURE.



**FIG. 5-11 TEMPERATURE VARIATION OF ALLOY**



FIG. 5-12. BEACON ASSEMBLY WITH FOAM

## VI. GROUND INSTRUMENTATION

### A. Receiving and Recording Stations

The primary ground receiving and recording station for the Strongarm firings was located at Wallops Island, Virginia. This station, which was constructed at the Ballistic Research Laboratories, consisted of a large complex of precision equipment in two 8 X 26 foot semitrailers, and an array of antennas in an adjacent field, as shown in Figures 6-1, 6-2 and 6-3. A pictorial view of the equipment in one of the trailers is shown in Figure 6-4. An auxiliary receiving and recording station was located 110 miles away at Spesutie Island, Aberdeen Proving Ground, Maryland.

### B. System Description

A simplified block diagram of the instrumentation system is shown in Figure 6-5. Each radio frequency (rf) signal transmitted from the moving rocket was received by a pair of helical antennas having circular polarity of opposite sense. This antenna configuration allowed frequency errors caused by rocket spin and Faraday effect to add to the biased Doppler frequency in one side of the dual channels, and to subtract from it in the other side. After the two harmonically related signals were received and filtered, they were applied to differential mixers. The output of these mixers contained twice the spin frequency and Faraday effect. This error output from two harmonically related signals was again mixed to give the Faraday differential frequency. This frequency was used to compute the total electron content of the atmosphere between the transmitting antennas on the rocket and the receiving antennas on the ground. The signals from the tracking filters were also applied to adder networks in a similar combination to that above, thereby eliminating spin and Faraday rotation error at each of the two radio frequencies. The 37 mc adder output, which was a 7 kc bias plus twice the Doppler frequency, was multiplied by two. The 148 mc adder output, which was a 28 kc bias plus twice the Doppler frequency, was divided by two. After this multiplication and division was performed the resultant frequencies were compared in a differential mixer. The output of this differential mixer was then used to compute electron density.

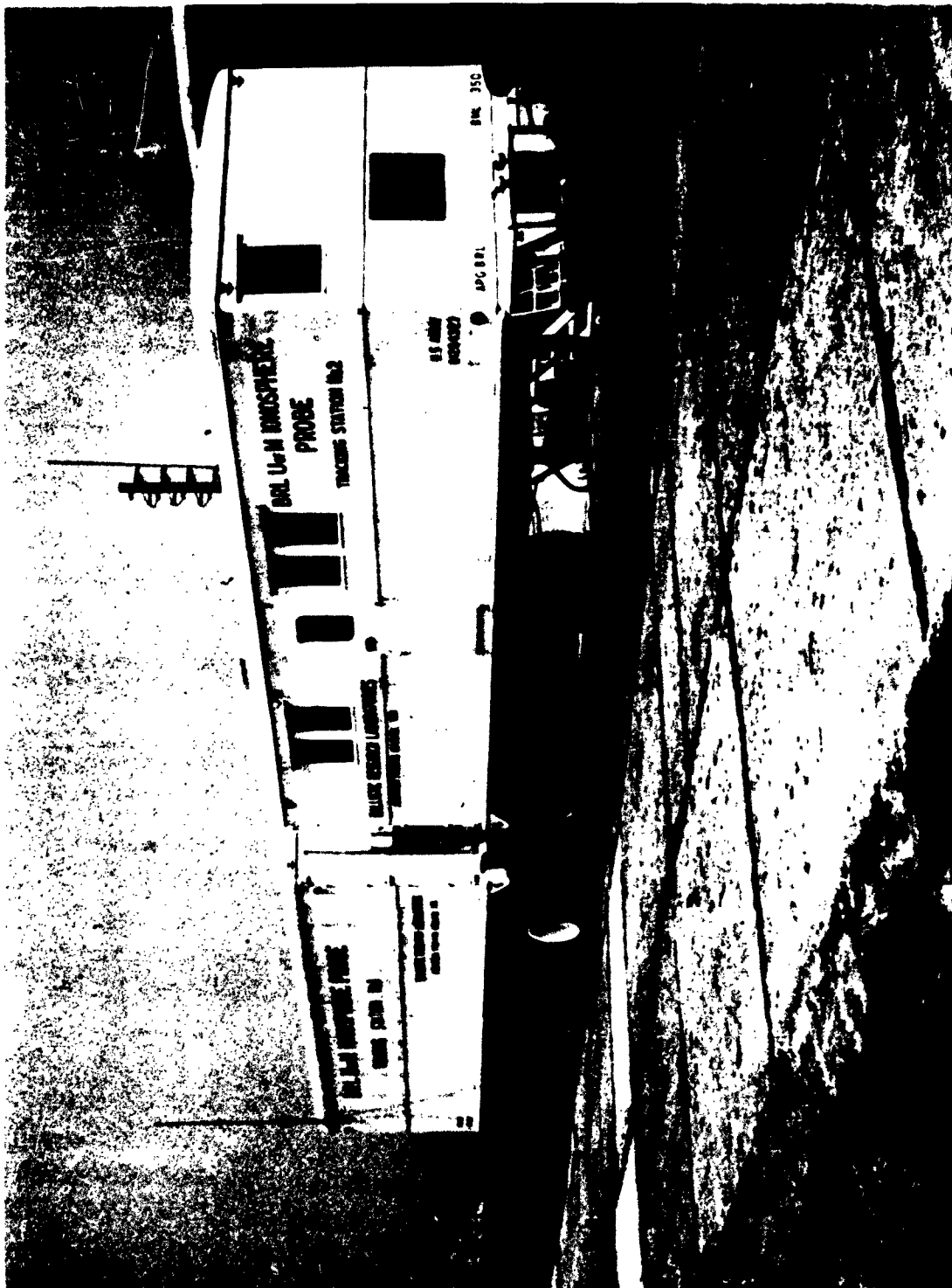


FIG. 6-1. GROUND STATIONS AT WALLOPS.

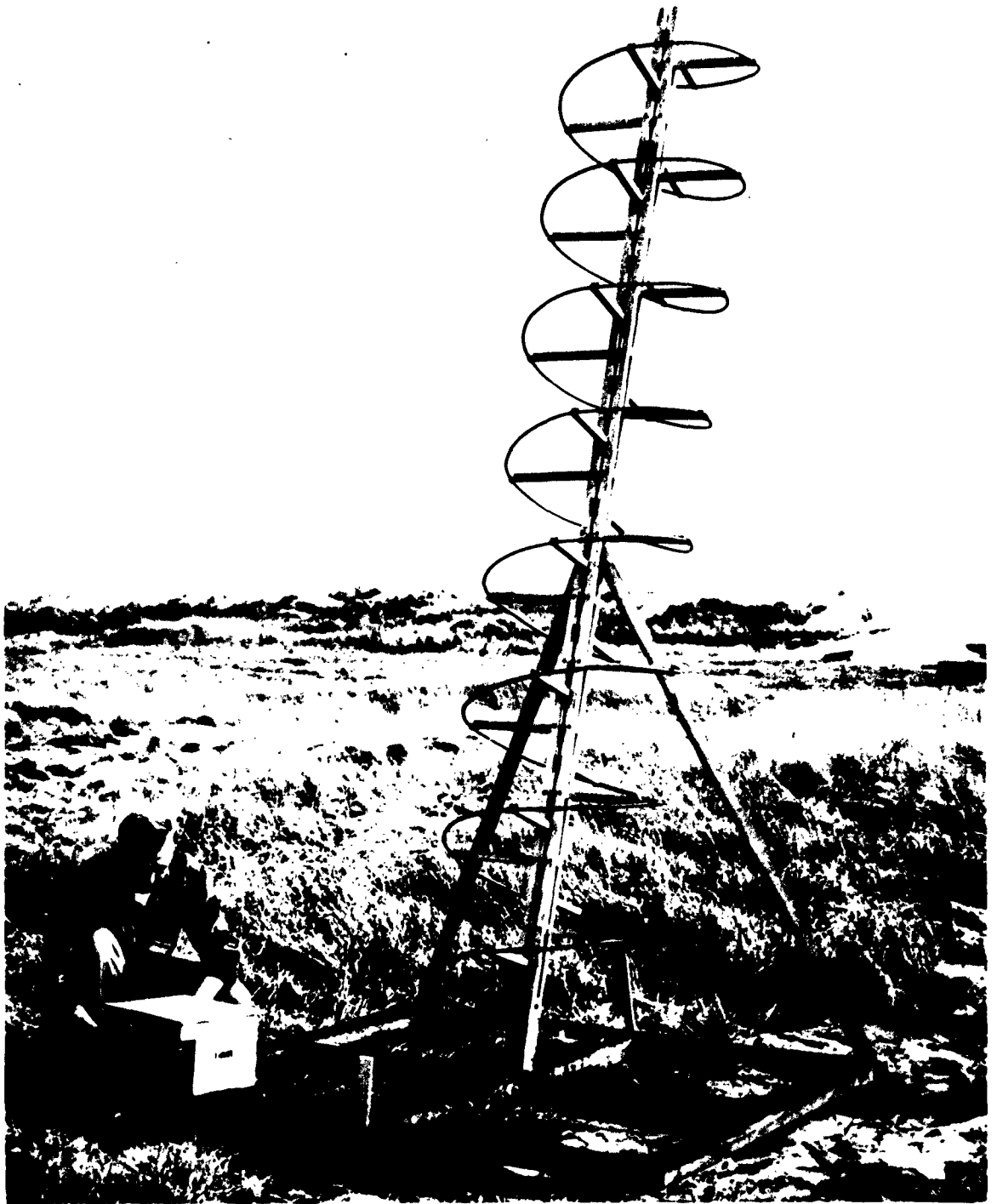


FIG. 6-2. HELICAL ANTENNA



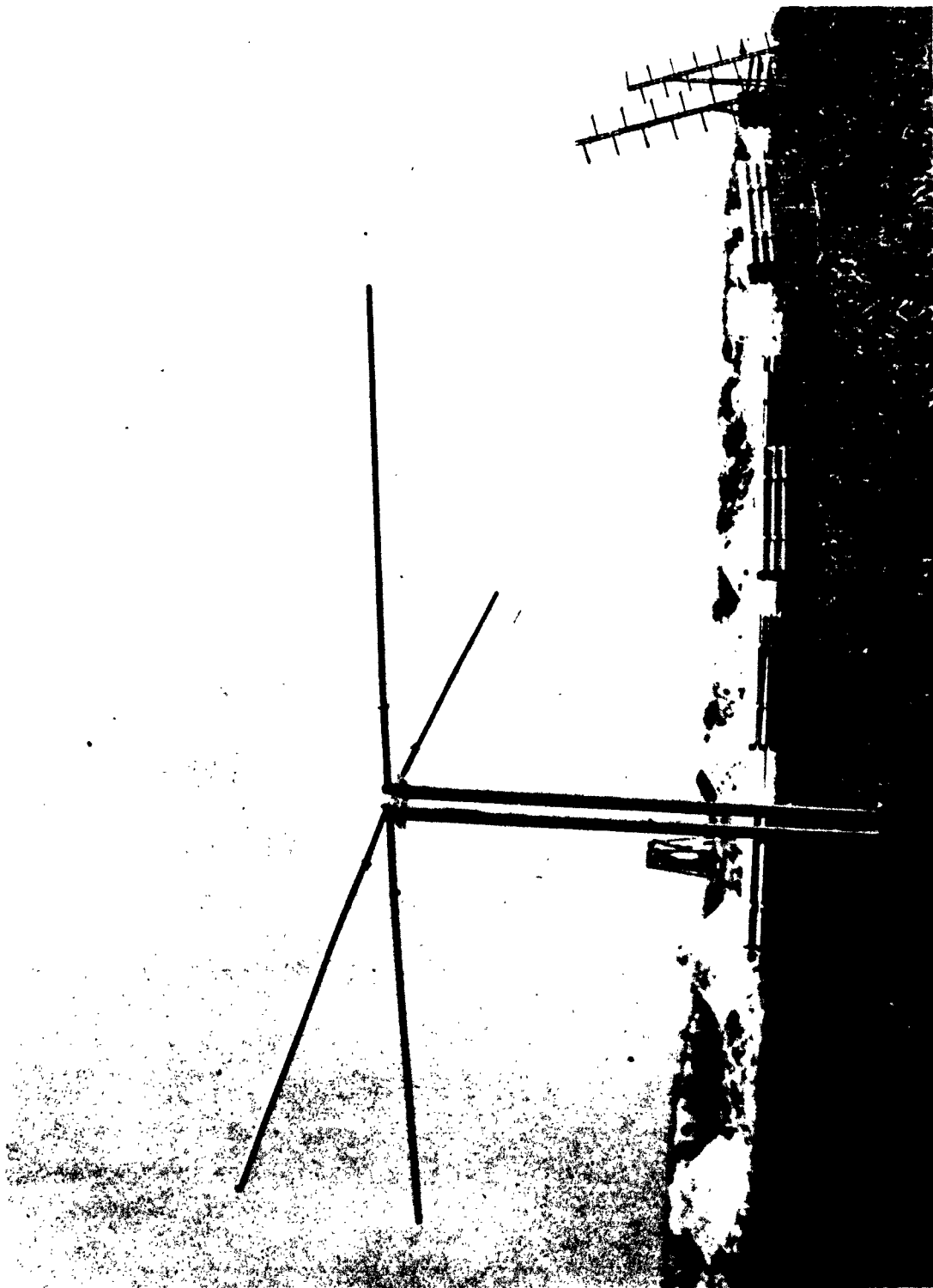


FIG. 6-3. CROSS-DIPOLE ANTENNA

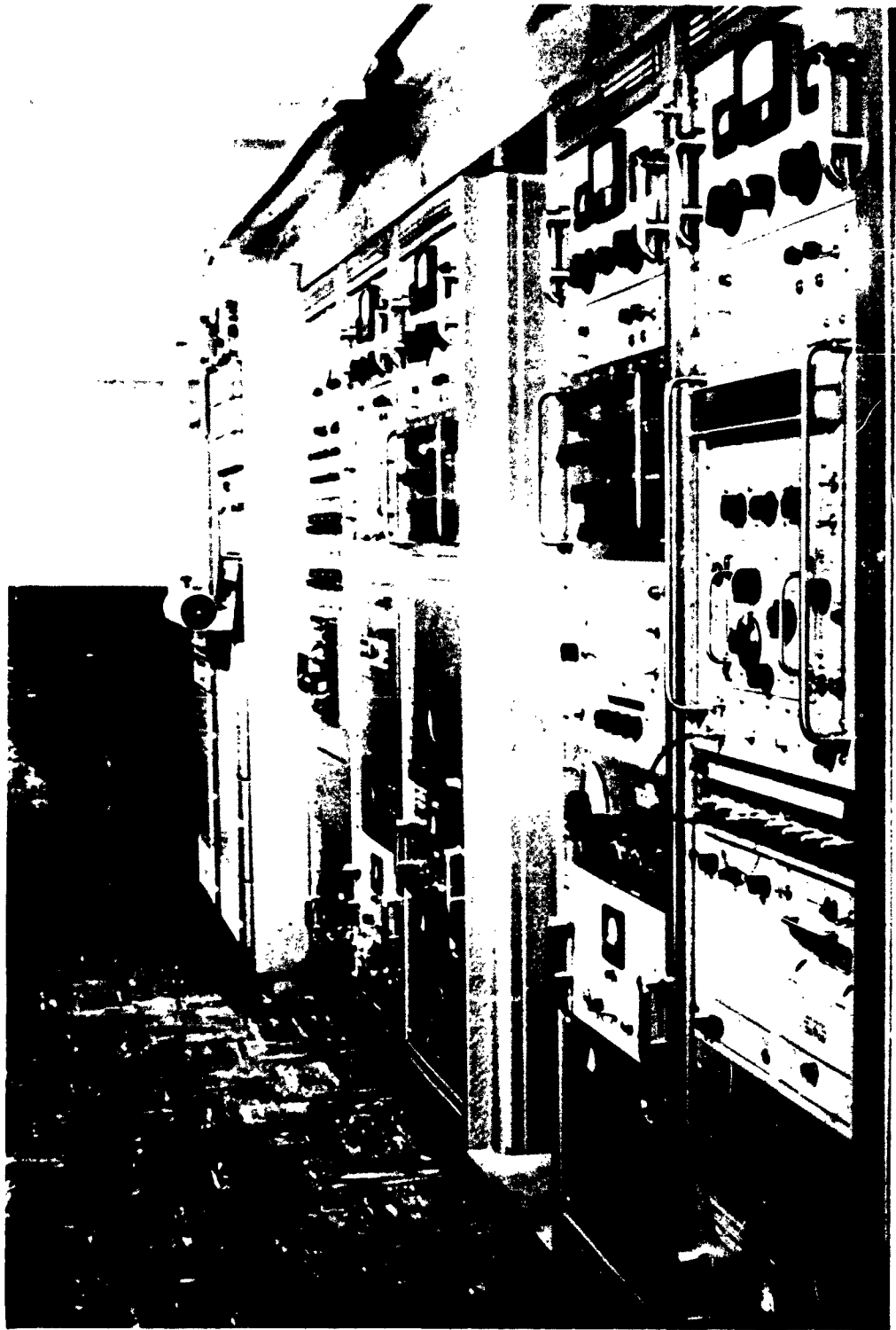


FIG. 6-4. GROUND STATION INTERIOR

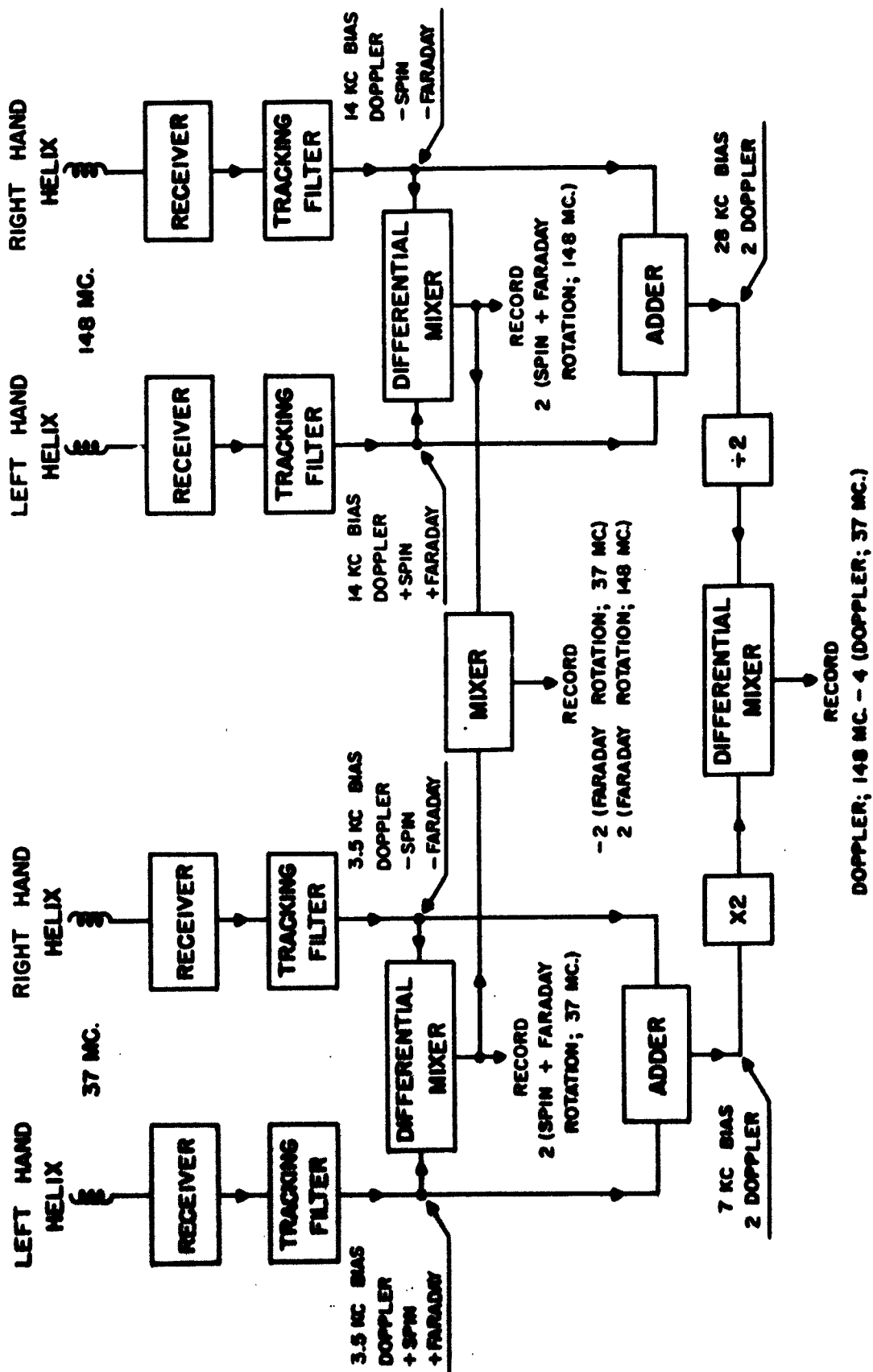


FIGURE 6-5 GROUND STATION BLOCK DIAGRAM

### C. Receiving Antennas

The helical receiving antennas used for the Strongarm I and II firings had desirable features such as circular polarization and relatively high gain. The characteristics of the 37 mc units were as follows: 2.5 turns, 8.5 feet in diameter, 14.5 feet in length,  $70^\circ$  beamwidth, and a gain of 6 db over an isotropic radiator for linearly polarized signals. The 148 mc antennas shown in Figure 6-2, had 8 turns, a diameter of two feet, a length of 12 feet, a beamwidth of  $40^\circ$ , and a gain of 11 db over an isotropic radiator. Each pair of antennas was placed four wavelengths apart at its particular frequency. Both pairs of antennas were placed in a single line perpendicular to the rocket firing azimuth. This placement cancelled parallax effects that would be encountered in frequency reception.

Cross-dipole antennas, shown in Figure 6-3, were used in place of the 37 mc helical antennas for the Strongarm III, IV and V firings. These antennas had essentially the same features as the helical antennas, but were much more portable, easier to assemble, and less affected by high winds.

In addition to the four main antennas there was a helical antenna for reception at 148 mc and a half-wave dipole antenna for reception at 37 mc. The particular function of these two additional antennas will be explained in subsection G below.

### D. Receivers and Preamplifiers

The ground receivers were specifically designed and built at the Ballistic Research Laboratories for making dispersive Doppler measurements. A block diagram of the receivers is shown in Figure 6-6. Four triple conversion superheterodyne receivers were used, all driven by common local oscillators through appropriate multipliers and isolation networks. This triple conversion superheterodyne system was used for increased stability, high gain, and better signal-to-noise ratio at the output. The first two local oscillators were crystal controlled and had a stability of one part in  $10^7$  after 30 minutes warm up time. The third local oscillator was a highly stable but adjustable unit used to precisely set the bias frequency. This adjustable oscillator was necessary because the various mixers and adders used for data handling depended upon a bias of  $3.5 \text{ kc} \pm 1\%$  for the low frequency Doppler and  $14 \text{ kc} \pm 4\%$  for the

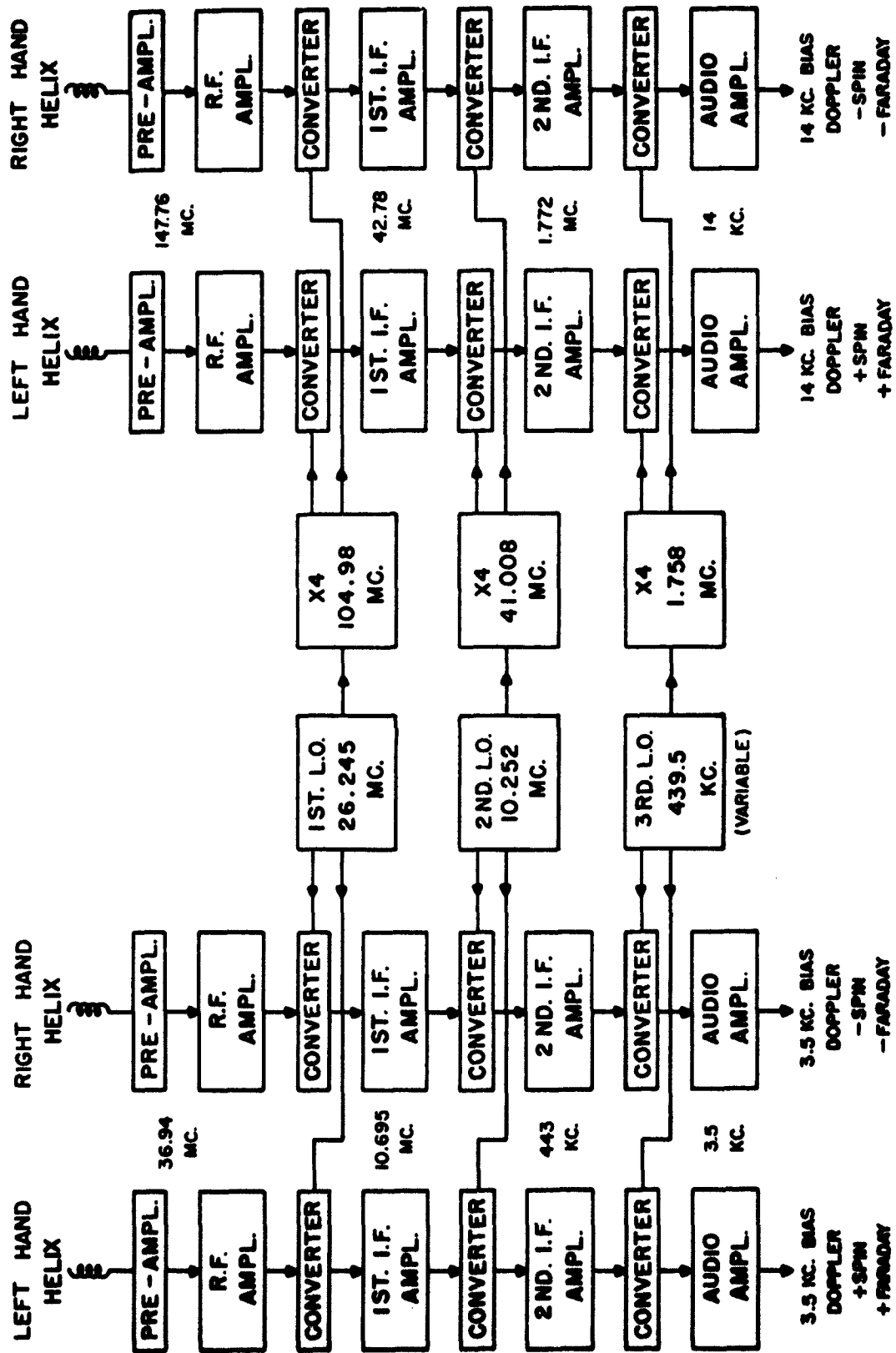


FIGURE 6-6 BLOCK DIAGRAM OF RECEIVERS

high frequency Doppler. The stability of the local oscillators was essential for keeping the bias frequencies within tolerance; however, the data outputs (Figure 6-5) were not dependent upon local oscillator or radio frequency stability since any frequency shifts were cancelled out. The bandwidths of the receivers were 5 kc and 20 kc for the 37 mc and 148 mc frequencies, respectively.

In the Strongarm experiments, preamplifiers were used at each antenna. This combination of preamplifiers and receivers resulted in an approximate system input sensitivity of 0.1 microvolts for a receiver output signal-to-noise ratio of unity.

#### E. Tracking Filters

Audio electronic tracking filters were used on the output of each receiver channel to obtain greater improvement in the signal-to-noise ratio. These devices were very narrow bandpass filters in which the output frequency follows or tracks the input frequency. This result was accomplished automatically by the use of a high-gain, phase-locked servo-controlled loop. Large signal-to-noise improvement in the output, as compared to the input, was obtained. The bandwidth used was dependent upon the dynamic change of the input frequency. Bandwidths of 50 cps and 25 cps were used on the high and low frequency channels respectively, during the burning phases of the Strongarm rockets; 5 cps and 2.5 cps were used thereafter. The filter enabled tracking of signals to approximately 30 db below the receiver output noise, thereby giving an overall system sensitivity of 3 nano-volts ( $3 \times 10^{-9}$  volts).

Another feature of the filters was a constant amplitude output which was necessary for the adding and differential data networks.

#### F. Data Separation and Recording

The data circuits in the instrumentation system were composed of adders, differencing networks, mixers, multipliers and dividers. Spin, Faraday rotation, dispersive Doppler, and signal strength data were presented in the form of an eight-channel chart record. Figure 6-7 shows a section of the original chart record from Strongarm III. Reading from top to bottom and referring also to Figure 6-5, the first two channels show a frequency that is twice the rate of rotation of the plane of polarization of the 37 mc and 148 mc signals. This rotation is a combination of rocket spin and changing Faraday rotation along

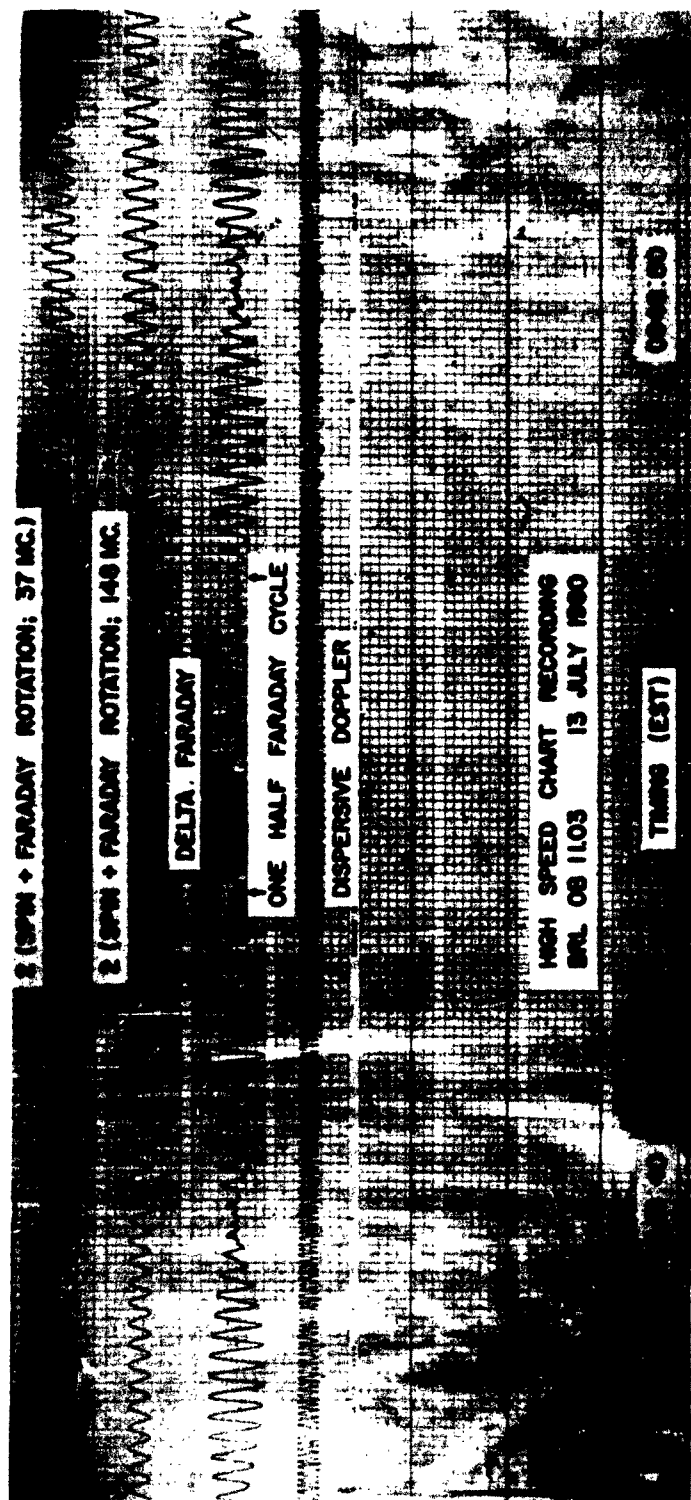


FIG. 6-7. SECTION OF ORIGINAL CHART RECORDING, STRONGARM III

the ray path. The amplitude modulation on the channel labeled "Delta Faraday" is, in effect, a beat frequency produced by mixing the inputs to channels One and Two. The modulation rate is equal to twice the rate of change of Faraday rotation at 37 mc minus twice the rate of change of Faraday rotation at 148 mc. The fourth channel is the dispersive Doppler where each cycle corresponds to a change of  $7.36 \times 10^{13}$  electrons per square meter column along the rocket to receiver ray path. Channels Five through Eight are the tracking filter AGC outputs from the 37 mc left, 37 mc right, 148 mc left, and 148 mc right receivers, respectively. This tracking filter AGC output indicated the received signal level, even though operating below receiver noise level. It also gave definite indication of non-lock of the tracking filters. This arrangement was necessary since one non-locked tracking filter would cause three of the four chart recorded data channels to become useless. Timing marks appear along both edges of the chart.

Magnetic tape recording was used for backup. In the Strongarm experiments described, tape recordings were made of the receiver outputs, tracking filter outputs, and the two biased Doppler frequencies from the adder circuits. A master frequency standard and timing generator, synchronized to the NBS station WWV, was used as the source for all frequency, period, and timing measurements. Local standard time in hours, minutes, and seconds was recorded on all records. These tape recordings could be used to produce additional chart recordings to recover missing data or to enable detailed examinations of certain parts of the record.

#### G. Telemetry and Miscellaneous Instrumentation

The telemetry data from the Strongarm rockets were received and recorded at the Wallops Island and Spesutie Island stations. These data were encoded in a pulse amplitude modulated signal, and a conventional AM receiver was used during the Strongarm I and II firings for data recovery. A 148 mc helical antenna and preamplifier, identical to those previously described, was used with the AM receiver. Increased signal-to-noise ratio at the receiver output was achieved by restricting the output bandwidth with a low pass filter. The tracking filters, described previously, had an auxiliary correlation output which was essentially an AGC output that was sensitive to amplitude variations



of the input signal. This correlation output gave an excellent indication of the pulse rate of the airborne telemeter. The correlation output was used as a back-up recording method for Strongarm rockets I and II, and as the sole recording method for Strongarm rockets III, IV and V.

In order to resolve any possible ambiguity in determination of rocket spin rates, it was thought desirable to determine rocket spin rates independently of the system previously described. The rocket antennas radiate linearly polarized signals toward the ground stations and a dipole on the ground receives linearly polarized signals. The received rf amplitude variations resulting from this polarization effect is an excellent indication of rocket spin rate. Therefore, a system which consisted of a 37 mc dipole antenna, preamplifier and receiver was set up to obtain these data. No ambiguities resulted from the Strongarm I and II firings, consequently this system was abandoned thereafter.

Each of the adder networks in the data circuits contained output signal frequencies which were twice the biased Doppler frequency (Figure 6-5). These output frequencies were divided by two resulting in a low-channel biased Doppler frequency ( $3.5 \text{ kc} \pm 625 \text{ cps}$ ) and a high-channel biased Doppler frequency ( $14 \text{ kc} \pm 2500 \text{ cps}$ ). A printed tabulation of the period for both of the biased Doppler frequencies was made at one second intervals prior to and during the rocket flights. A "quick-look" plot of Doppler frequency versus time was made by integrating the low-channel biased Doppler frequency and recording this analog frequency output on a slow speed chart recorder. When the bias was subtracted, a true plot of Doppler frequency versus time was obtained.

A slight attenuation of the 37 mc rf signal and a slight increase of the 148 mc rf signal level was observed at about 38 seconds, or 5th stage burnout, on Strongarm I. To enable a more precise determination of the amount of change of these signal levels, a recording was made of the receiver AGC voltages on the left side of each dual channel. These signals were recorded on a low frequency chart recorder, and also recorded on tape for backup and replay purposes.

## VII. VEHICLE PERFORMANCE DATA

### A. Strongarm I

The first Strongarm rocket was fired from the NASA launching facility at Wallops Island, Virginia, on 10 November 1959 at 0700 EST. The elevation angle was  $80^{\circ}$ , and the azimuth was  $127^{\circ}$ . All five rocket stages functioned normally. A maximum velocity of 17,000 ft/sec was reached at the fifth stage burnout altitude of 215,000 feet. Peak altitude was approximately 1120 miles, a new Wallops Island record. Impact occurred some 26 minutes later about 920 miles out in the Atlantic Ocean.

Plots of the velocity versus time, acceleration versus time, and spin rate versus time during the first 50 seconds of the Strongarm I flight are shown in Figures 7-1, 7-2, and 7-3.

The predicted velocities of Figure 7-1 are instantaneous tangential velocities computed for a vertical firing. The Doppler velocities are radial velocities averaged over a one second interval surrounding the plotted point. For a vertical firing with the receiving station directly under the rocket, tangential and radial velocities would be equivalent. However, for a non-vertical firing radial velocities would have a tendency to be lower than tangential velocities.

The accelerations plotted in Figure 7-2 were obtained by differencing velocities over a one second interval and consequently are average accelerations for a one second interval.

There is a possibility that the beacon transmitter may have shifted in frequency during periods of high acceleration, and even during periods of change from acceleration to deceleration. Such a frequency shift would obviously introduce errors into the velocities obtained from the Doppler data and these errors would tend to be magnified in the accelerations because of the way in which the accelerations were obtained.

The possibility also exists that any frequency shift might be recovered during the coast periods. However, the possibility is just as strong that any such frequency shifts would not be fully recovered.

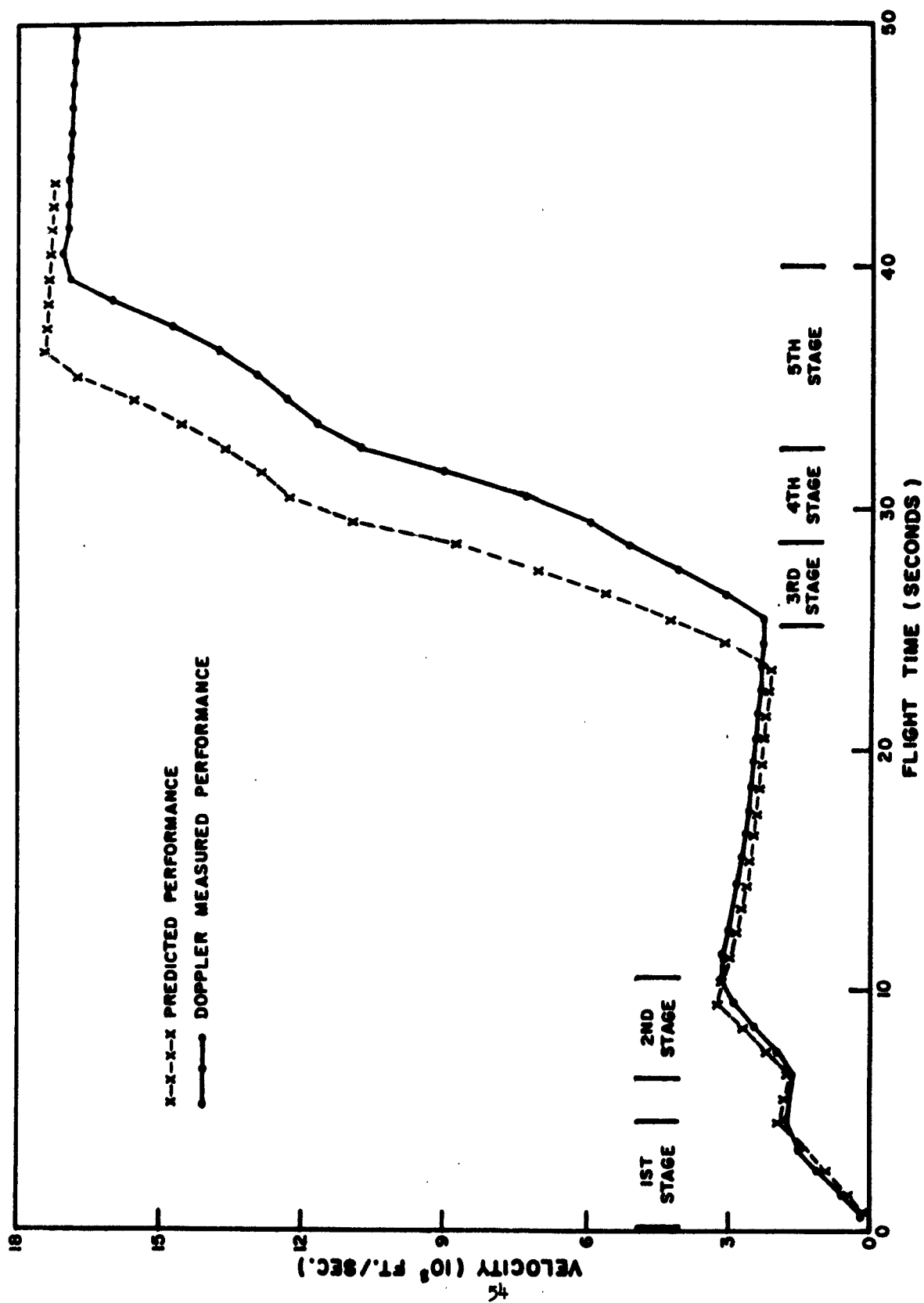
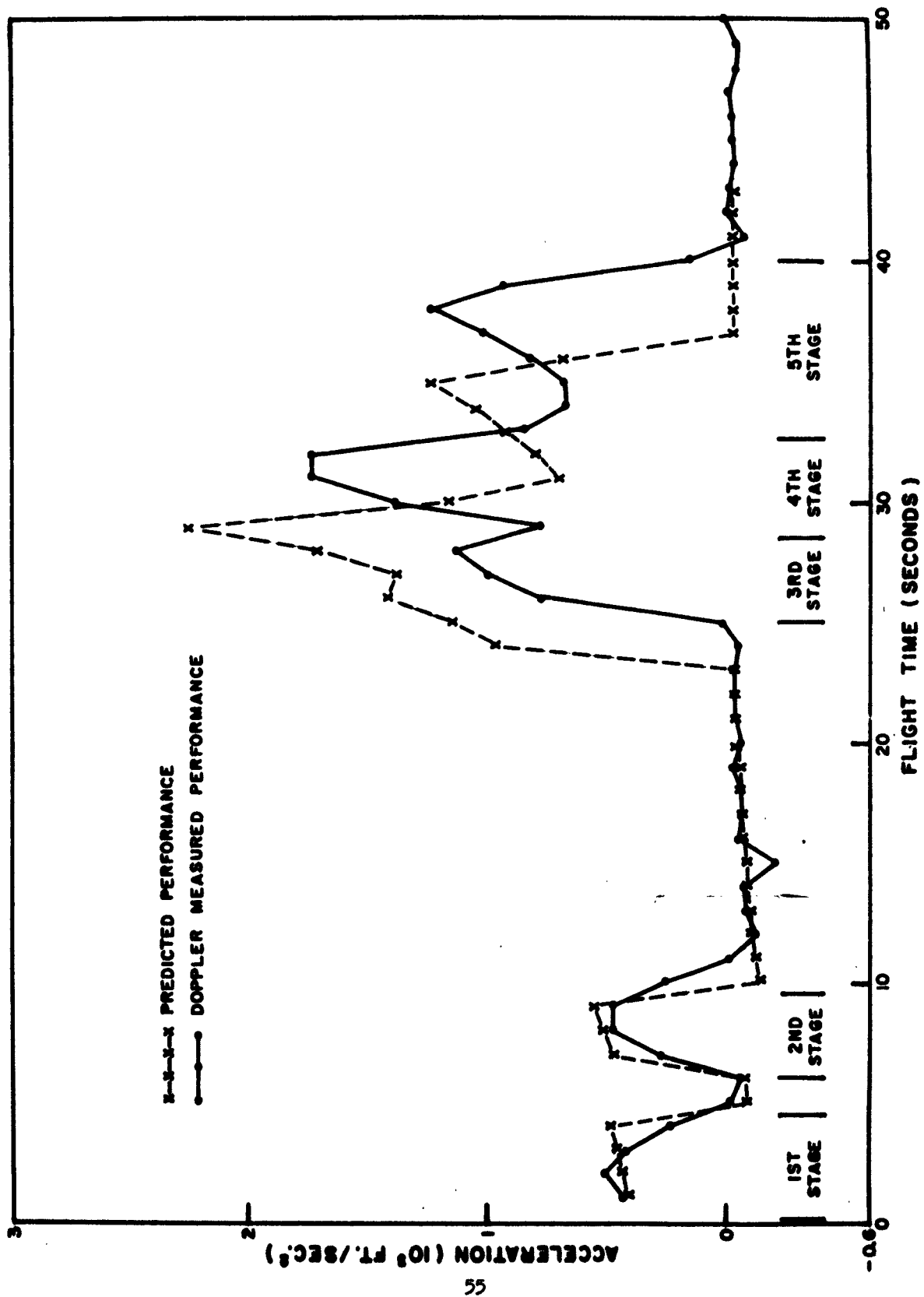


FIG. 7-1. VELOCITY VS TIME, STRONGARM I.



**FIG. 7-2. ACCELERATION VS TIME, STRONGARM I.**

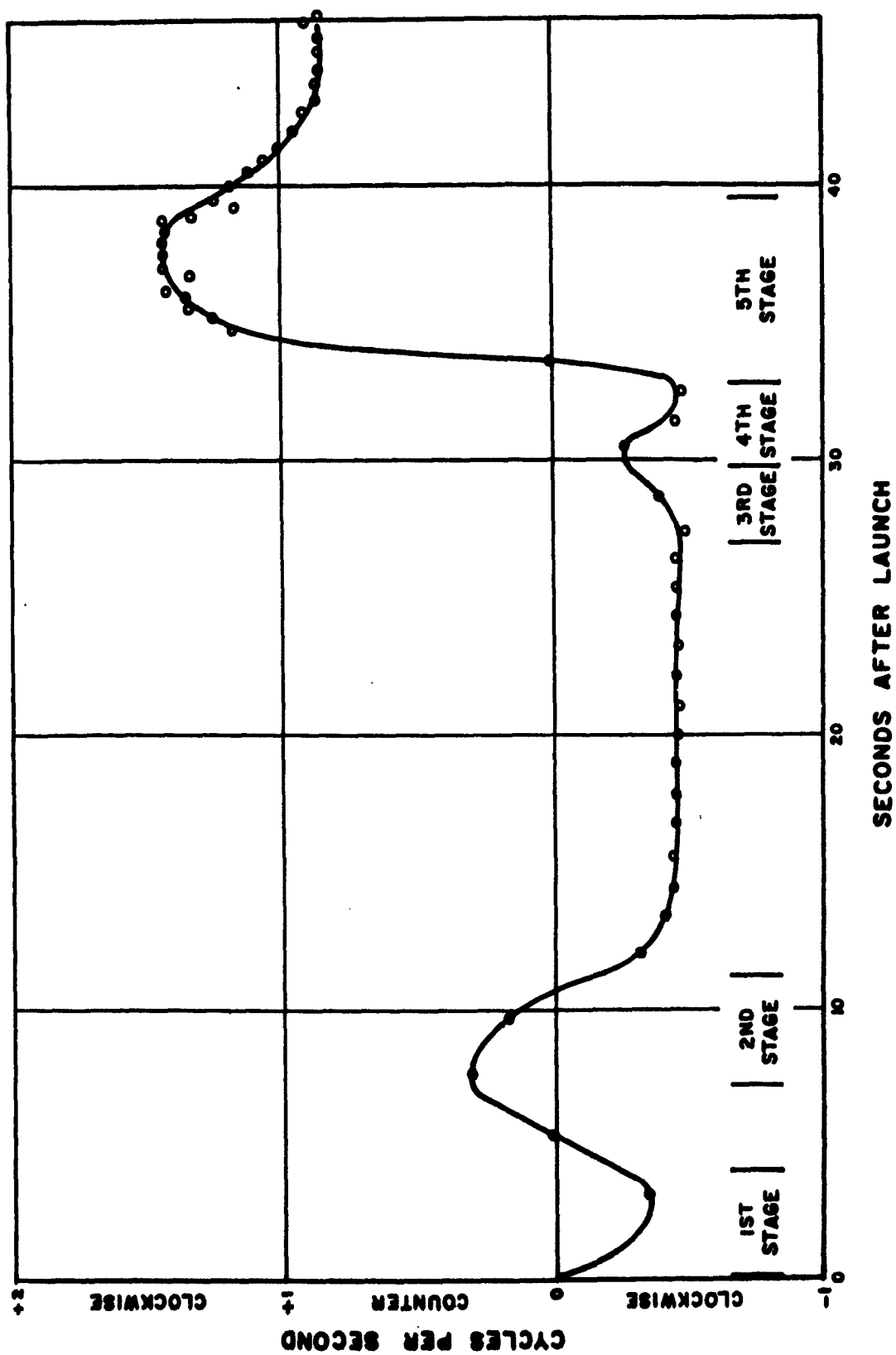


FIG. 7-3. SPIN RATE VS TIME, STRONGARM I

The data plotted in Figure 7-3 show that Strongarm I changed spin direction several times during the first 33 seconds of flight, but the spin rate did not exceed 0.5 rev/sec. The first four rocket stages burned during this time interval. The spin direction reversed during fifth stage burning, and the spin rate increased to 1.5 rev/sec. The spin rate then dropped to a steady 0.9 rev/sec rate thereafter.

The chart recording of the spin and Faraday rotation data (Figure 9-1) indicated that the Strongarm I rocket also precessed with a 47.2 second period.

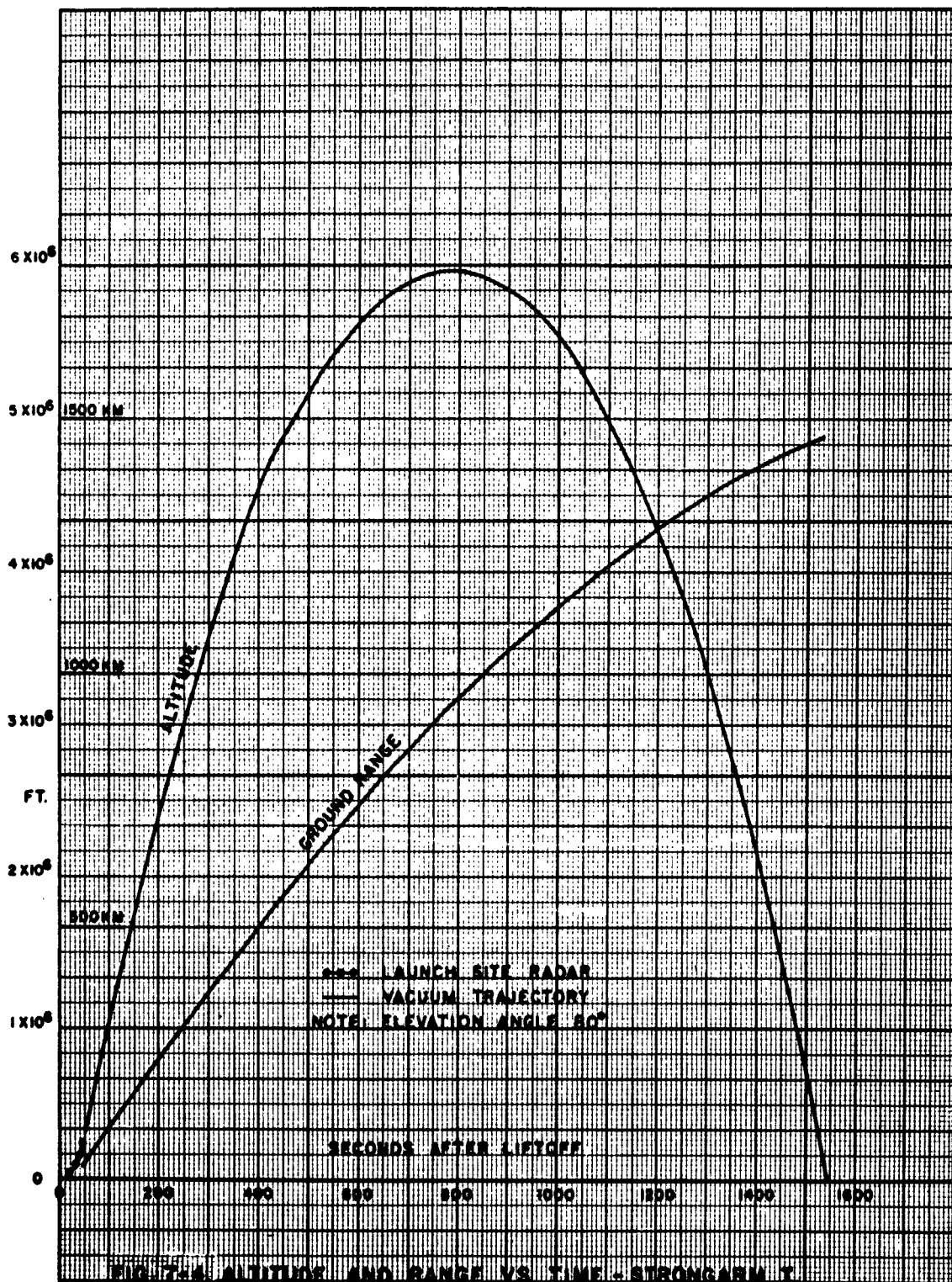
A plot of the Strongarm I trajectory is given in Figure 7-4. This trajectory was determined by altering vacuum trajectory initial conditions, which were obtained from the launch site radar data, so that the times of zero and maximum radial velocities, as determined from the trajectory for both the Wallops Island and the Spesutie Island Doppler receiving sites, compared favorably with the times of zero and maximum Doppler shift recorded at those two sites.

It had been hoped that the Millstone Radar Facility at Westford, Mass., would provide additional trajectory data, but this equipment was inoperative at the time of the Strongarm I firing.

#### B. Strongarm II

The second Strongarm rocket was fired from the Wallops Island Facility on 18 November 1959 at 2200 EST. The elevation angle was  $80^{\circ}$  and the azimuth was  $127^{\circ}$ . It was immediately evident from visual observation that, while the first and second stages functioned normally, the third stage, and hence the fourth and fifth stages failed to ignite. This conclusion was confirmed by the three radar plotting boards and the beacon Doppler frequency. The maximum velocity was 3,000 ft/sec, and the peak altitude only 20 miles.

It was thought that this failure may have resulted from a broken firing line to the third stage, or from a forward movement of the Nike grain in the third stage during coast, which could have broken the delay squibs.



### C. Strongarm III

The third Strongarm rocket was fired from the Wallops Island Facility 13 July 1960 at 0947 EST. The elevation angle was  $83^{\circ}$ , and the azimuth was  $90^{\circ}$ . The radar plotting boards indicated a maximum velocity of 11,000 ft/sec, and the peak altitude was approximately 400 miles.

The 11,000 ft/sec velocity corresponded to the predicted velocity at fourth stage burnout, and the immediate conclusion was that the fifth stage had not burned. From the beacon Doppler, however, it was noted that the period of acceleration beginning at third stage ignition was about 8-1/2 to 9 seconds in duration. This period appeared to be abnormally long for a Nike booster and a Yardbird rocket which each have burning times of 3-1/4 seconds. Thus, since the Scale Sergeant burns about 6 seconds, the hypothesis was advanced that the actual rocket combination which burned was the third stage Nike, and the fifth stage Scale Sergeant.

The spin rate versus time data for Strongarm III are plotted in Figure 7-5. The pattern of this spin rate plot is quite similar to the spin rate plot of Strongarm I (Figure 7-3) with the exception that the maximum spin rate of Strongarm III rose to 2.2 rev/sec during fifth stage burning and remained at that level.

The chart recording of the Strongarm III spin and Faraday Rotation data (Figure 9-4) shows no effects due to precession.

A plot of the Strongarm III trajectory is given in Figure 7-6. This trajectory was obtained by adjusting the initial conditions of the vacuum trajectory obtained from the launch site radar so that the vacuum trajectory compared favorably with the data supplied by the Millstone Radar Facility, Westford, Massachusetts. This comparison is shown in Figure 7-7, and was made in terms of height (Z) above a plane tangent to the earth at the launch site.

### D. Strongarm IV

The fourth Strongarm rocket was fired from the Wallops Island Facility on 13 July 1960 at 2143 EST. The elevation angle was  $83^{\circ}$ , and the azimuth was  $90^{\circ}$ . The radar plotting boards indicated a maximum velocity of 11,250 ft/sec, and the peak altitude was approximately 430 miles.



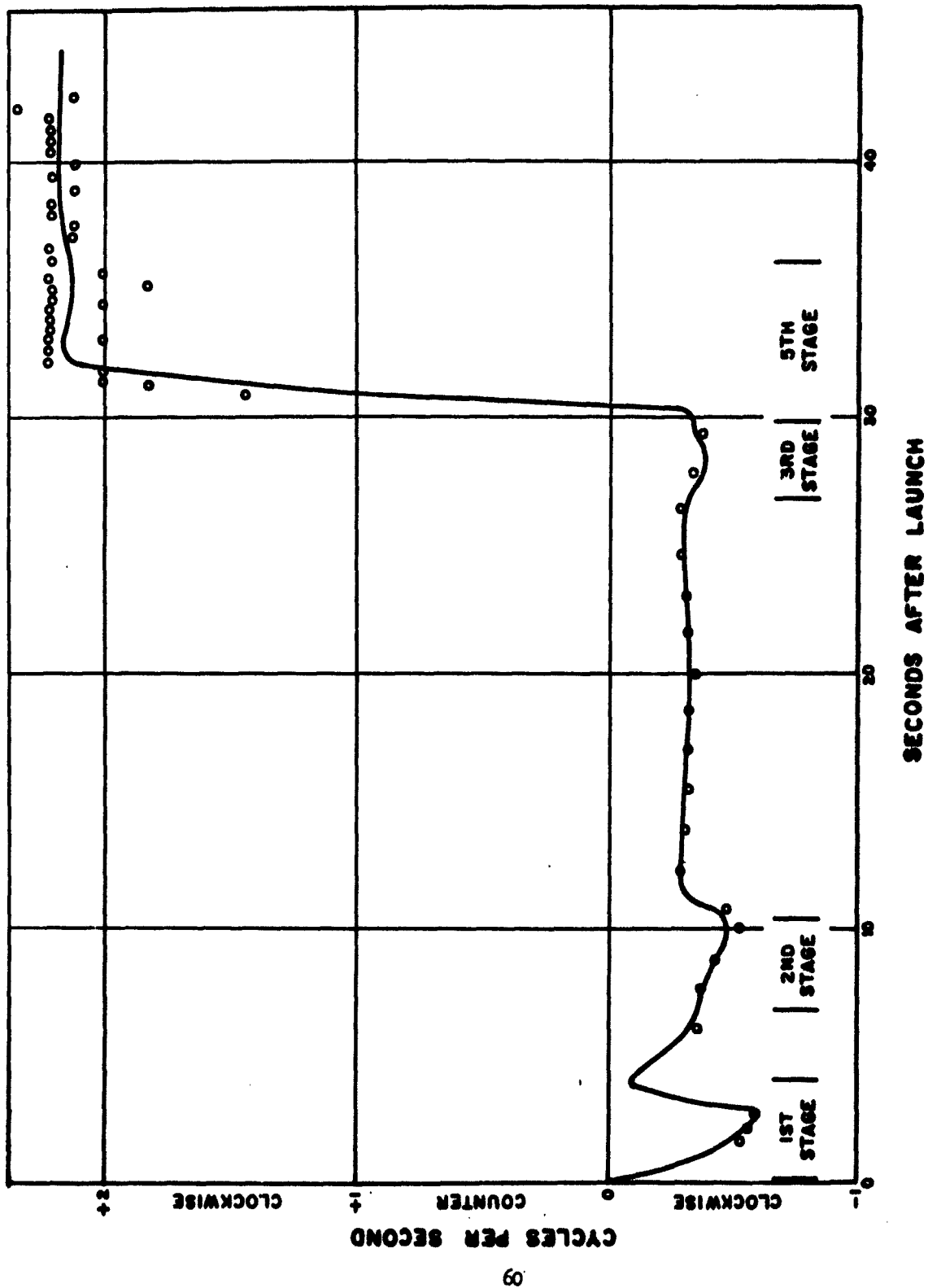
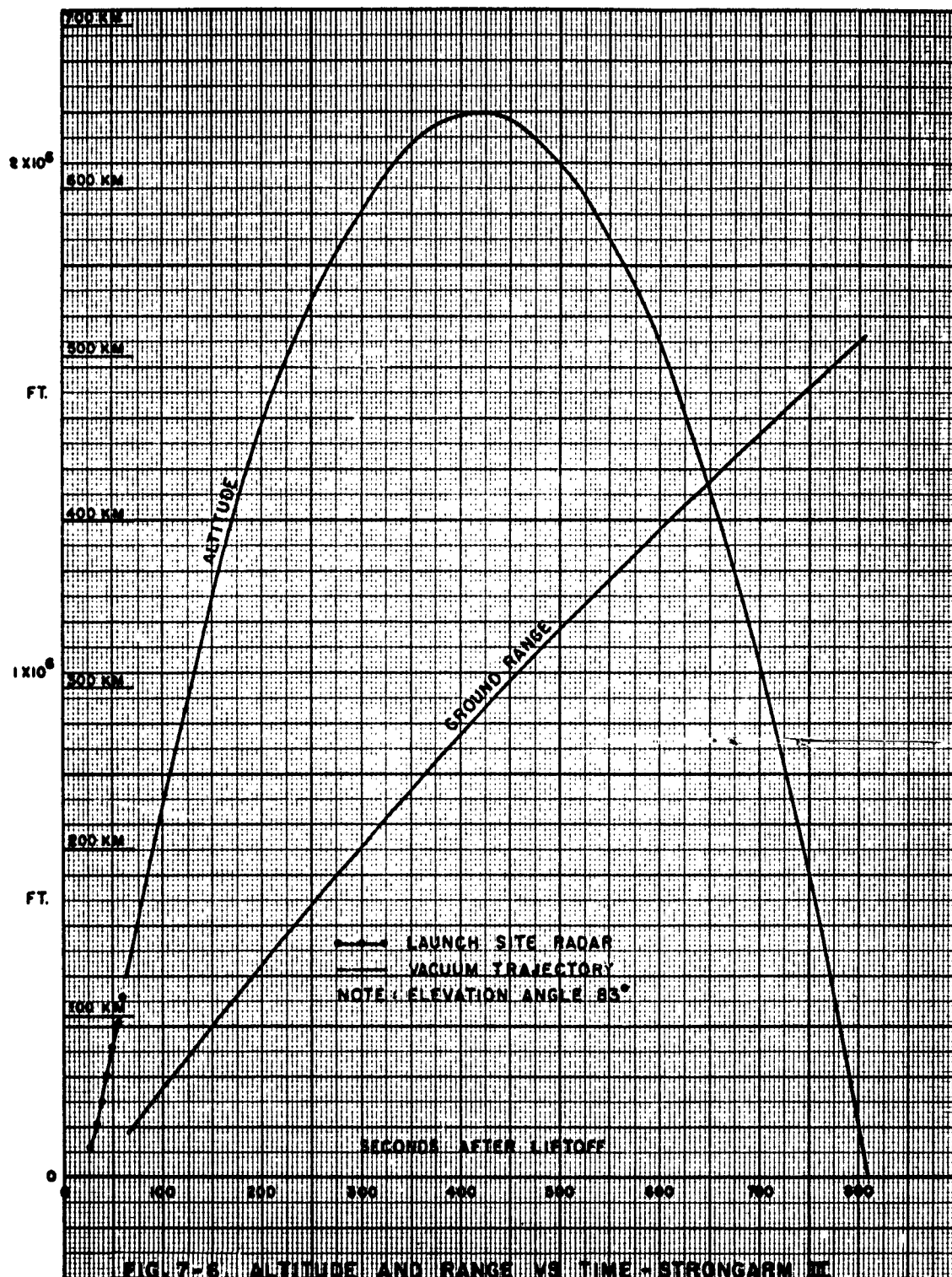
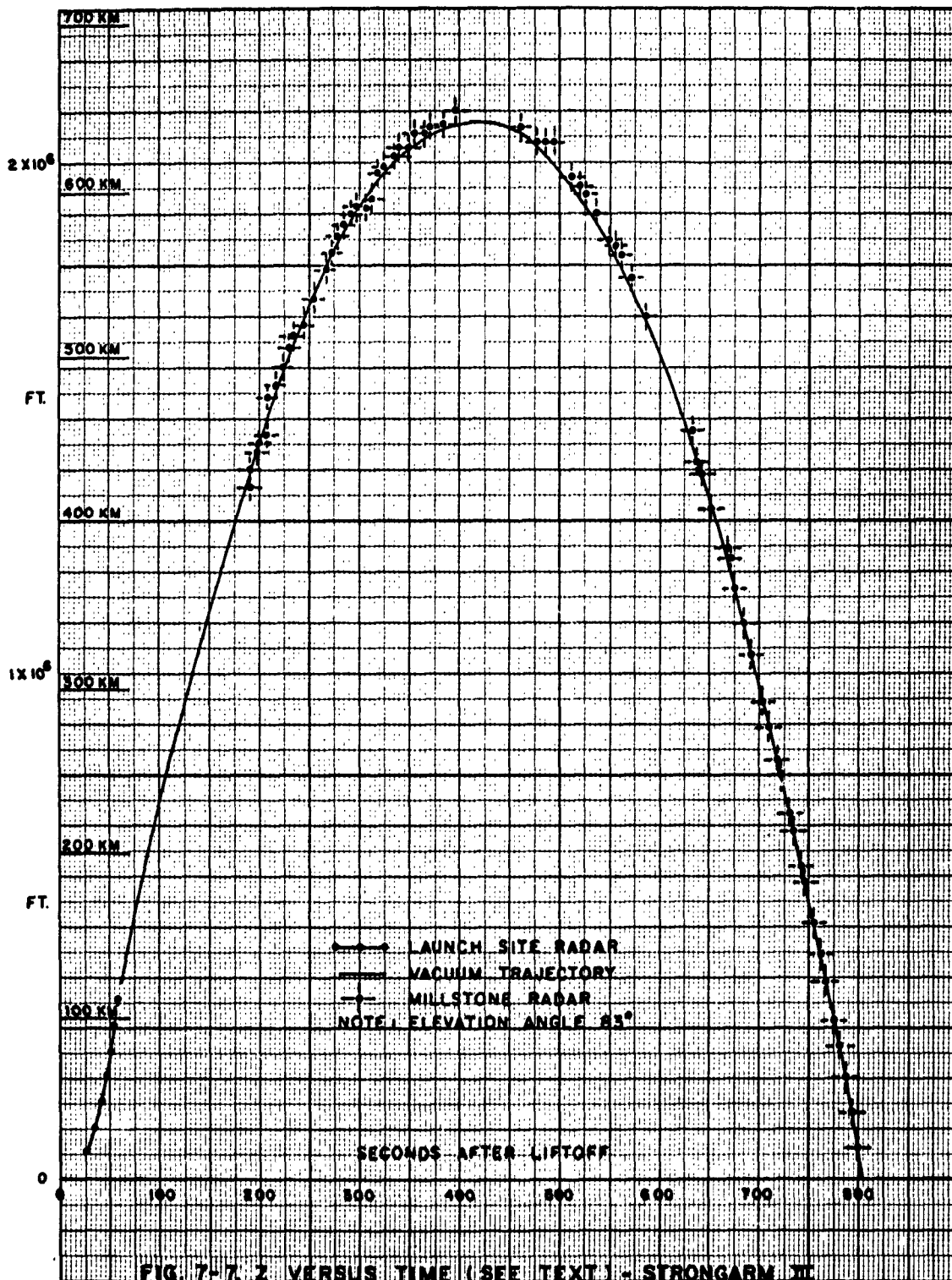


FIG. 7-5. SPIN RATE VS TIME, STRONGARM III





The 11,250 ft/sec velocity corresponded to the normal operation of four stages, and the immediate conclusion was that the fifth stage had failed to ignite. All subsequent data were consistent with the hypothesis that the rocket performed normally through the first four stages, and that the fifth stage did not burn.

The spin rate versus time data for Strongarm IV are plotted in Figure 7-8. It can be seen that this is a fairly typical spin rate pattern if a comparison is made with the spin data of Strongarm I (Figure 7-3) and Strongarm III (Figure 7-5). The maximum spin rate leveled off at 1.1 rev/sec after fourth stage burning.

The chart recording of the spin and Faraday rotation data indicated that the Strongarm IV rocket precessed with a period which varied from 118 to 145 seconds.

A plot of the Strongarm IV trajectory is shown in Figure 7-9. This trajectory was determined by the same method that was employed to obtain the Strongarm III trajectory. A comparison of the height (Z) above the tangent plane and the Millstone radar data is given in Figure 7-10.

#### E. Strongarm V

The fifth Strongarm rocket was fired on 1 August 1960 at 2214 EST. The elevation angle was  $83^{\circ}$ , and the azimuth was  $90^{\circ}$ . The radar plotting boards indicated a maximum velocity of 9,350 ft/sec, and showed that a sharp change of course occurred during fourth stage burning, the flight path changing  $5^{\circ}$  upward and  $14^{\circ}$  to the left. Multiple radar targets then indicated that the rocket had broken up. Subsequent reduction of radar range data and Doppler telemetry fixed the time of failure at 2.6 to 2.8 seconds after Yardbird ignition.

A malfunction of a Yardbird motor in an Exos rocket launched during November 1959 at Eglin Air Force Base, Florida, resulted in the same catastrophic yaw and failure. Photographs of the Exos showed a separation at the time of failure which suggested that the nozzle of the Yardbird or a portion of it had burned off. This failure occurred at the identical burning time (2.6 seconds) as in the Strongarm V, and it was therefore concluded that the two failures were identical in nature.

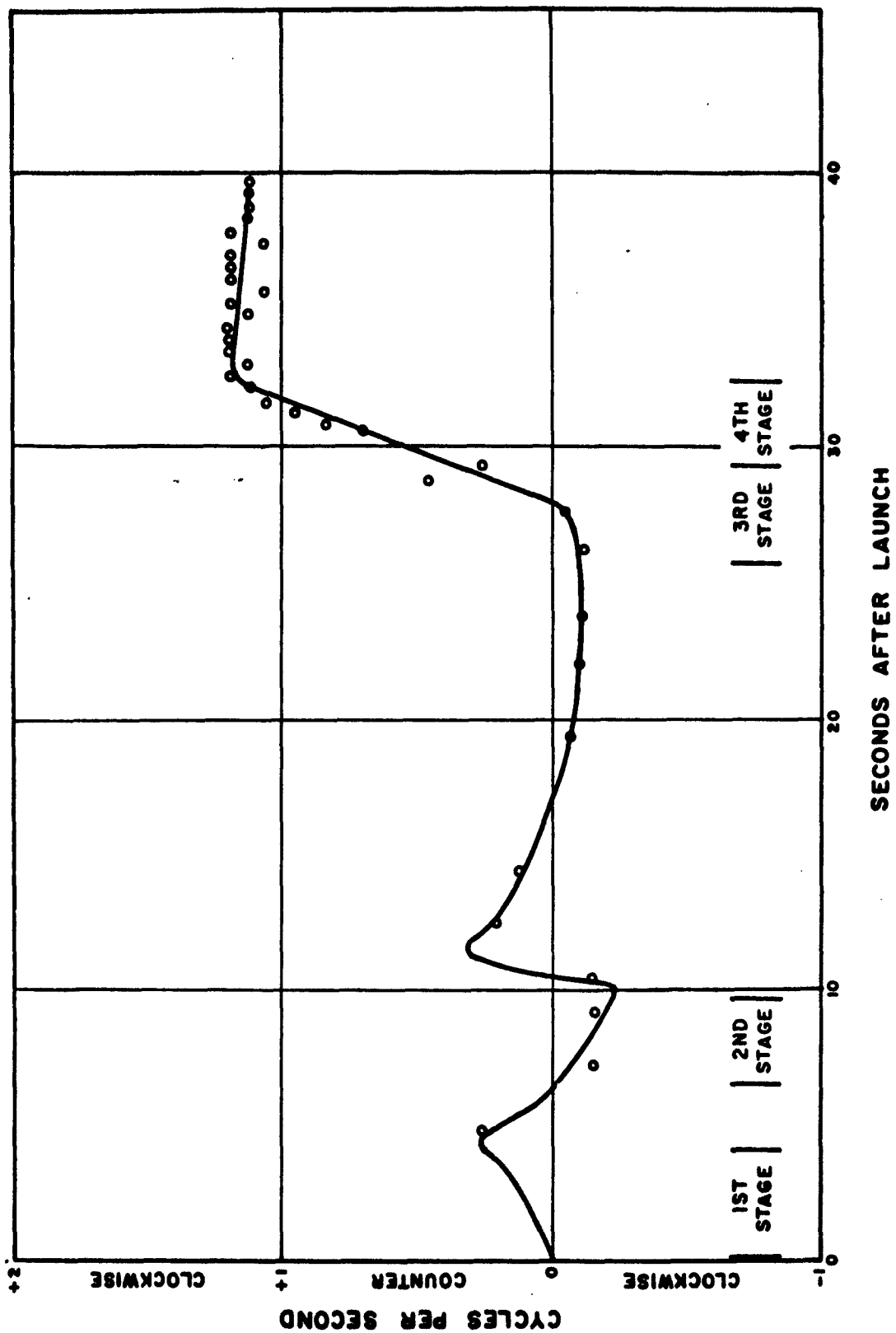
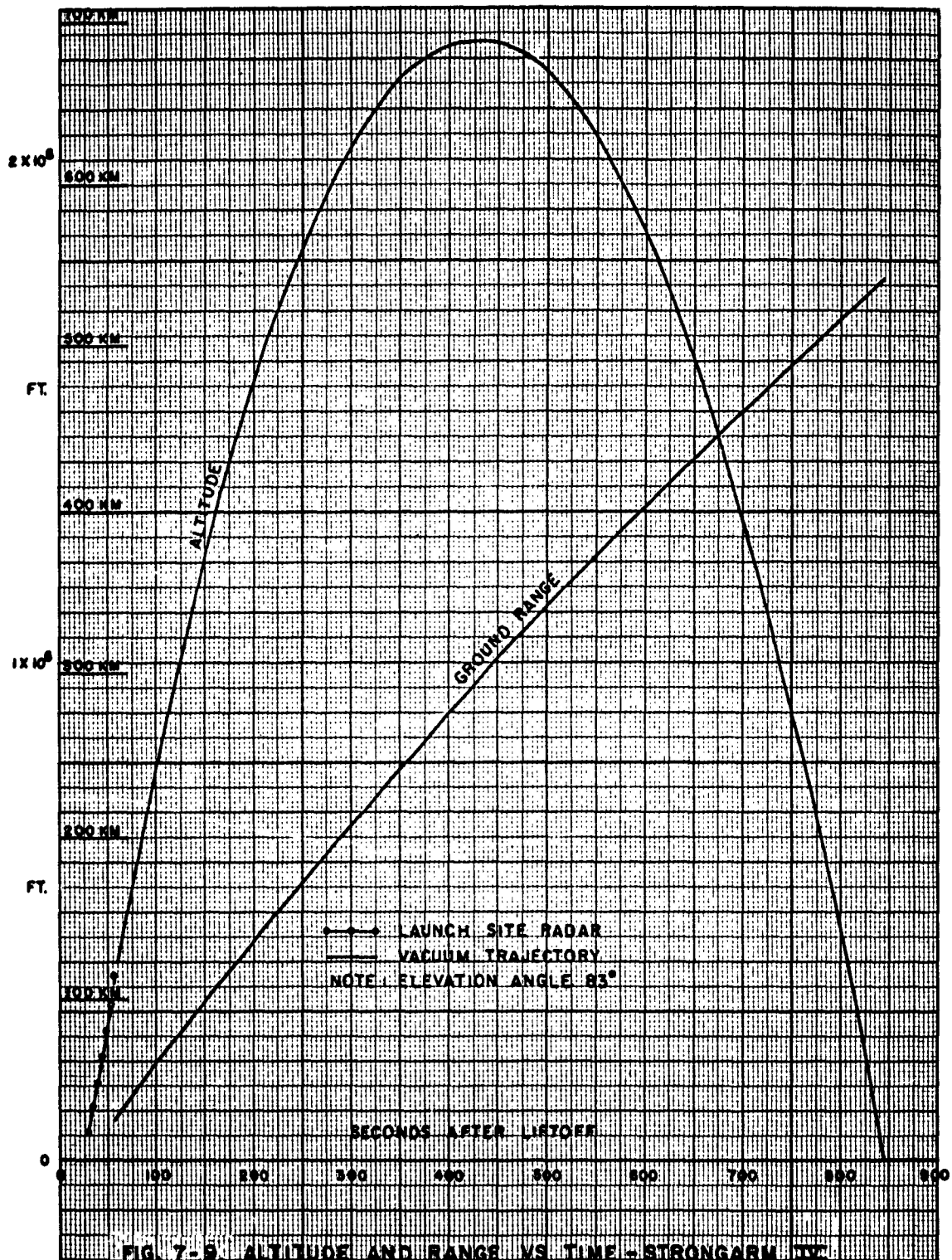
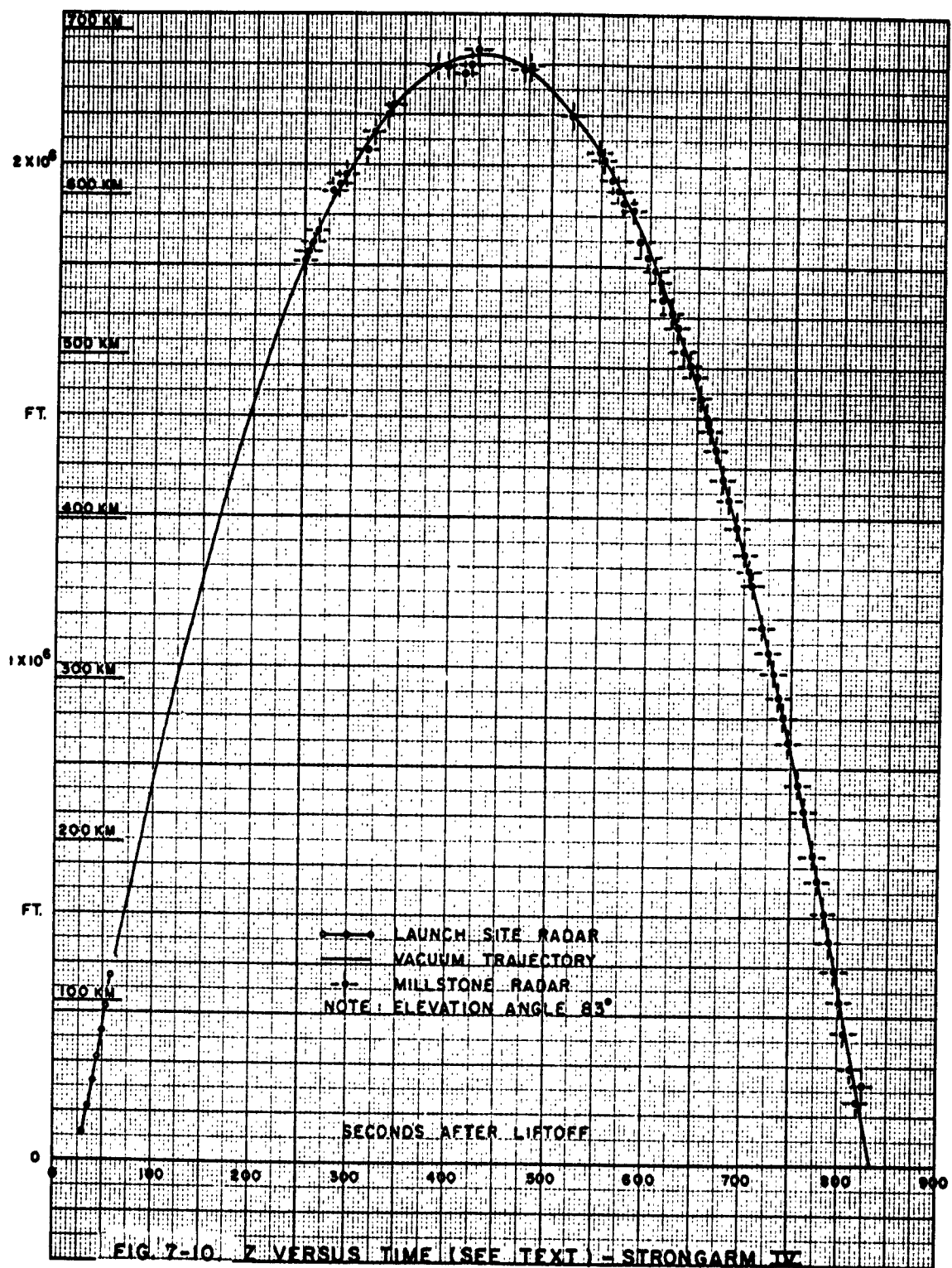


FIG. 7-8: SPIN RATE VS TIME, STRONGARM IV





## VIII. NOSE CONE AND BEACON TEMPERATURE DATA

### A. Nose Cone Temperature Data

The temperatures of the teflon-fiberglass interface at a point 28.8 inches from the nose tip of the Strongarm I and III rockets are plotted in Figure 8-1.

The temperature of the interface at this point on the nose cone of the Strongarm I rocket was  $2.2^{\circ}\text{C}$  at launch. The telemeter record showed an intermittent thermistor circuit for the first 76 seconds of flight, after which the circuit recovered, and indicated a maximum temperature of  $160^{\circ}\text{C}$  after 100 seconds of flight. The temperature then slowly declined to  $115^{\circ}\text{C}$  after 500 seconds of flight. At this time, the temperature of the beacon package reached  $47^{\circ}\text{C}$ , and the planned telemeter cut-off occurred.

The temperature of the nose cone interface of the Strongarm III rocket was higher at launch than that of the Strongarm I rocket, being approximately  $25^{\circ}\text{C}$  as compared with  $2.2^{\circ}\text{C}$ . However, the temperature of the nose cone interface of the Strongarm III rocket only reached a maximum of  $90^{\circ}\text{C}$  during flight as compared with  $160^{\circ}\text{C}$  for the Strongarm I rocket. This result reflects the fact that fewer of the Strongarm III rocket stages fired, and the maximum velocity was lower than that of the Strongarm I rocket.

### B. Beacon Temperature Data

Beacon package temperatures for the Strongarm I, III and IV rockets are plotted in Figure 8-2. Two point measurements were made in the case of the Strongarm I and III rockets by measuring the temperatures immediately prior to launch and employing a temperature fuze in the beacon package to turn off the telemeter when the temperature of the beacon package reached  $47^{\circ}\text{C}$ . The telemeter thermistor was removed from the nose cone interface and mounted in the beacon package on the Strongarm IV rocket, thus, providing a continuous measurement of the temperature in the beacon package during this flight. It would appear from Figure 8-2 that the temperatures in the beacon packages did not exceed  $60^{\circ}\text{C}$  during the first 800 seconds of the Strongarm I, III and IV flights. Thus, the beacon package temperatures were lower than the maximum allowable operating temperature of  $75^{\circ}\text{C}$  during this time interval. Reference to Figures 7-4, 7-6 and 7-9 shows that this time interval coincided with the time from launch to peak altitude for Strongarm I and to the entire flight times of Strongarm III and IV.



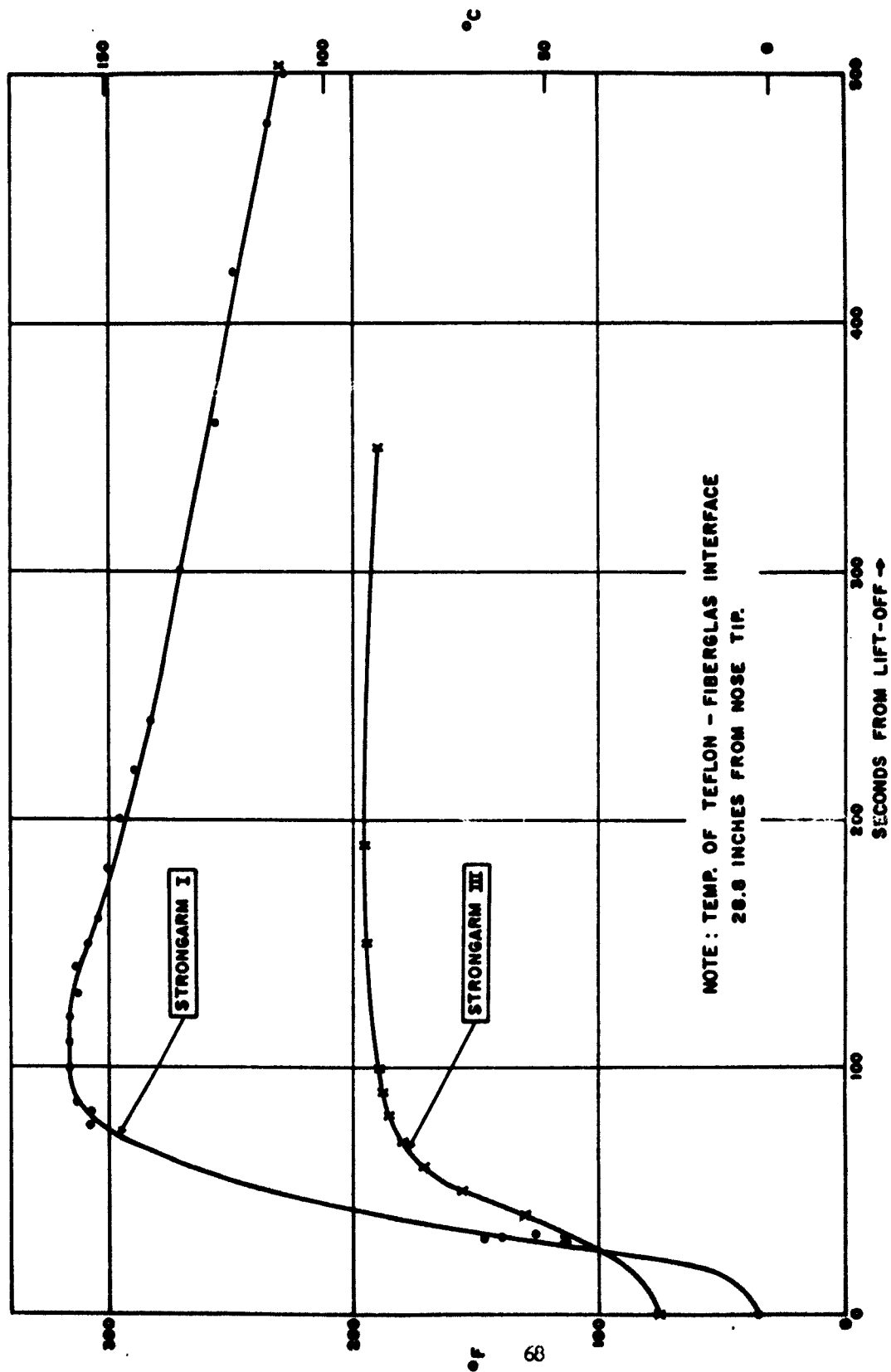


FIG. 8-1. NOSE CONE TEMPERATURES, STRONGARM I, III.

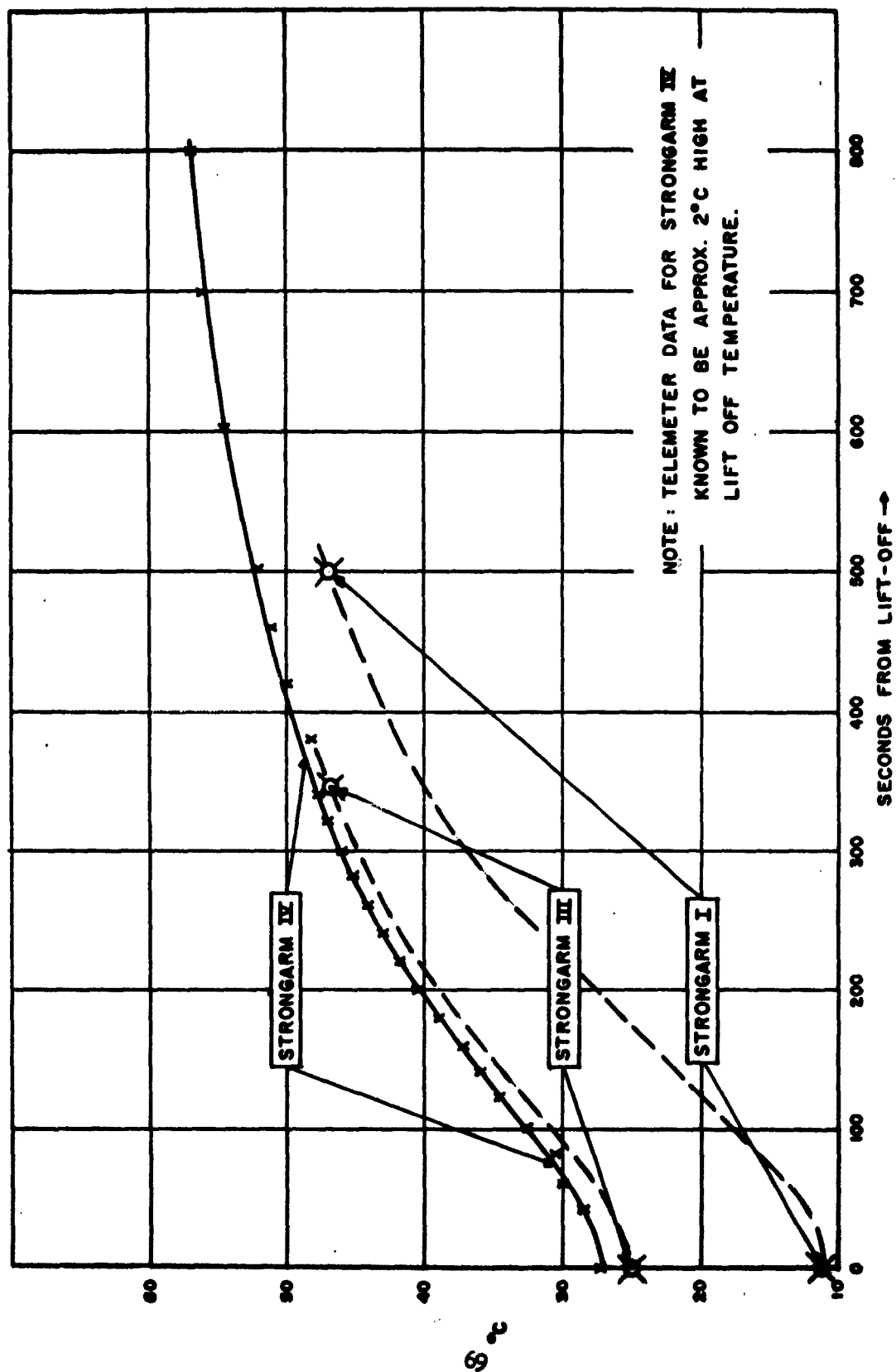


FIG. 8-2. BEACON PACKAGE TEMPERATURES, STRONGARM I, II, III.

## IX. ELECTRON DENSITY PROFILES AND INHOMOGENEITIES

### A. Strongarm I

Strongarm I was fired at 0700:04 EST on 10 November 1959 during a geomagnetically quiet period.

Figure 9-1 shows a section of a chart record from this flight. The effect of the 48 second period precession is clearly evident on the spin channels. This precession also caused sections of the dispersive Doppler record to be unreadable and necessitated interpolation through the distorted sections.

Since the flight took place shortly after sunrise, the ionization was increasing rapidly so that the correction for temporal variations in integrated content described in the theory section was necessary. Figure 9-2 shows the variation in  $N_{\max}$  during the period as determined from ionograms made at Fort Belvoir, Virginia, about 115 miles northwest of the launch site. As a result of the difference in longitude between Fort Belvoir and Wallops Island, the diurnal variation at Wallops Island could be expected to lead that at Fort Belvoir by approximately 6 1/2 minutes. The times in Figure 9-2 have been adjusted to take into account this 6 1/2 minute difference in solar time. The  $N_{\max}$  values used to compute the no-elapsed-time profile are shown by the solid line. The dashed lines have slopes differing by  $\pm 10\%$  from that of the solid line and were used to determine the effects of changes in  $dN_{\max}/dt$  on the derived electron density profile.

Figure 9-3 is the "no-elapsed-time" electron density profile at 0700:50 EST obtained from Strongarm I ascent data. The time for the Fort Belvoir profile shown in Figure 9-3 would correspond to approximately 0653:30 at Wallops Island if an adjustment were made for the solar time differential. The error bars illustrate the effect of the  $\pm 10\%$  variation in  $dN_{\max}/dt$  where the higher rate of increase of  $N_{\max}$  leads to decreased electron densities. The effect is only 1%-2% at 700 km and decreases rapidly below this altitude.\*

---

\* This rocket flight is believed to be the first to yield an electron density profile to an altitude of 1500 kilometers.

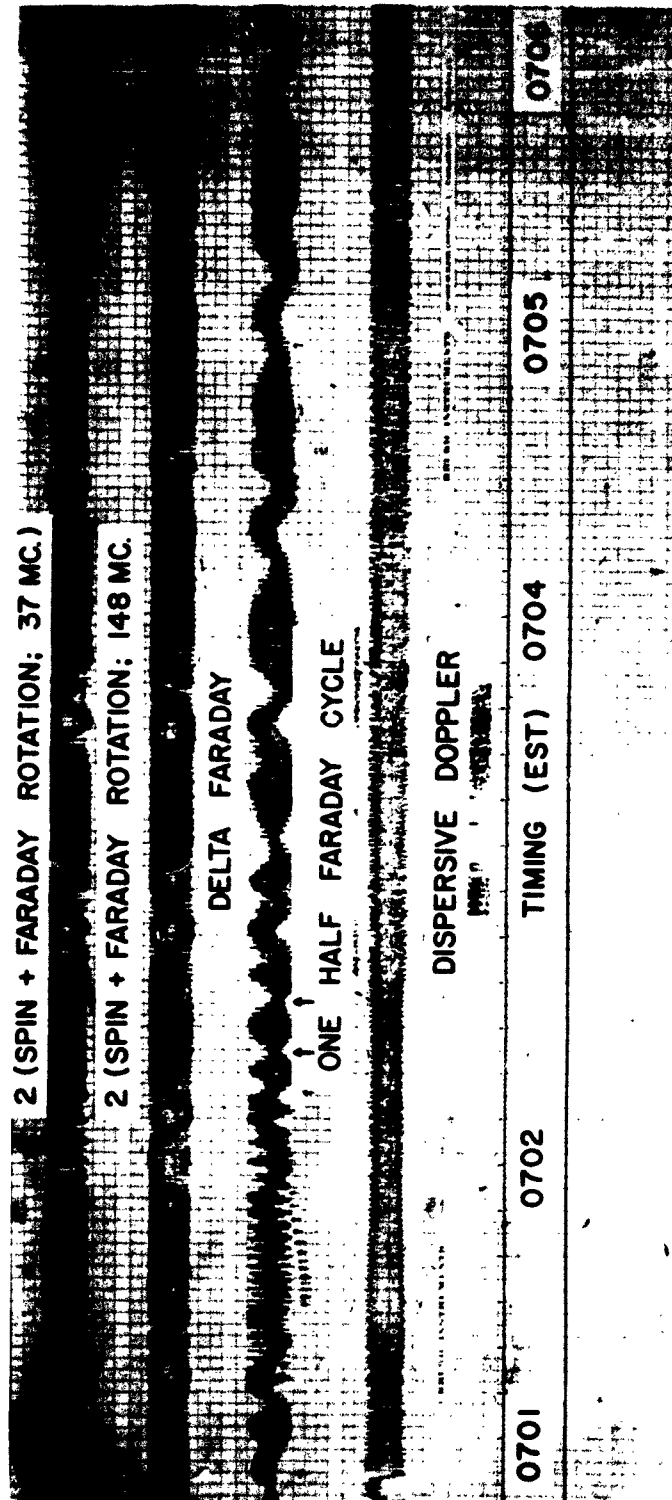


FIG. 9-1. SLOW SPEED CHART RECORDING, STRONGARM I

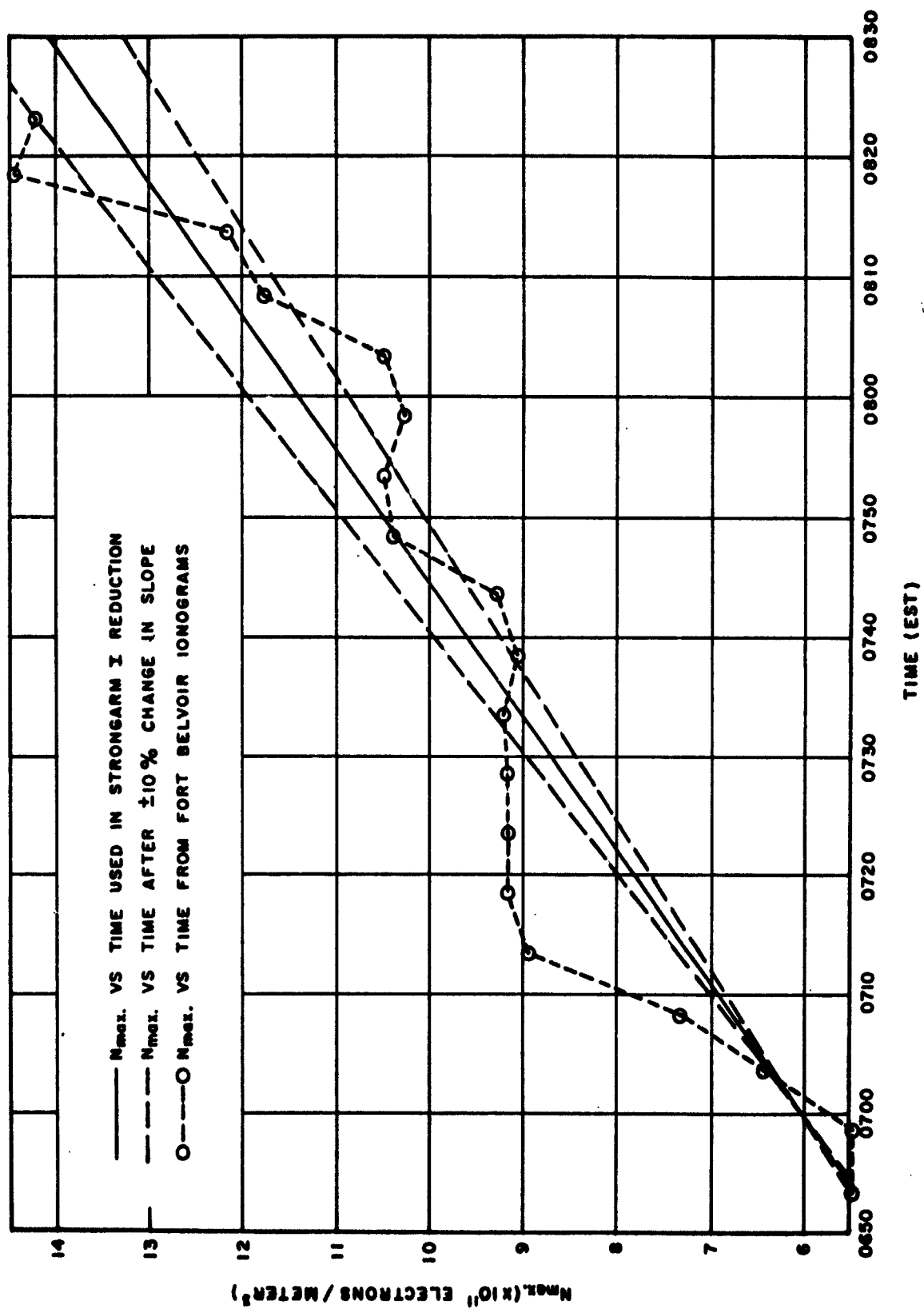
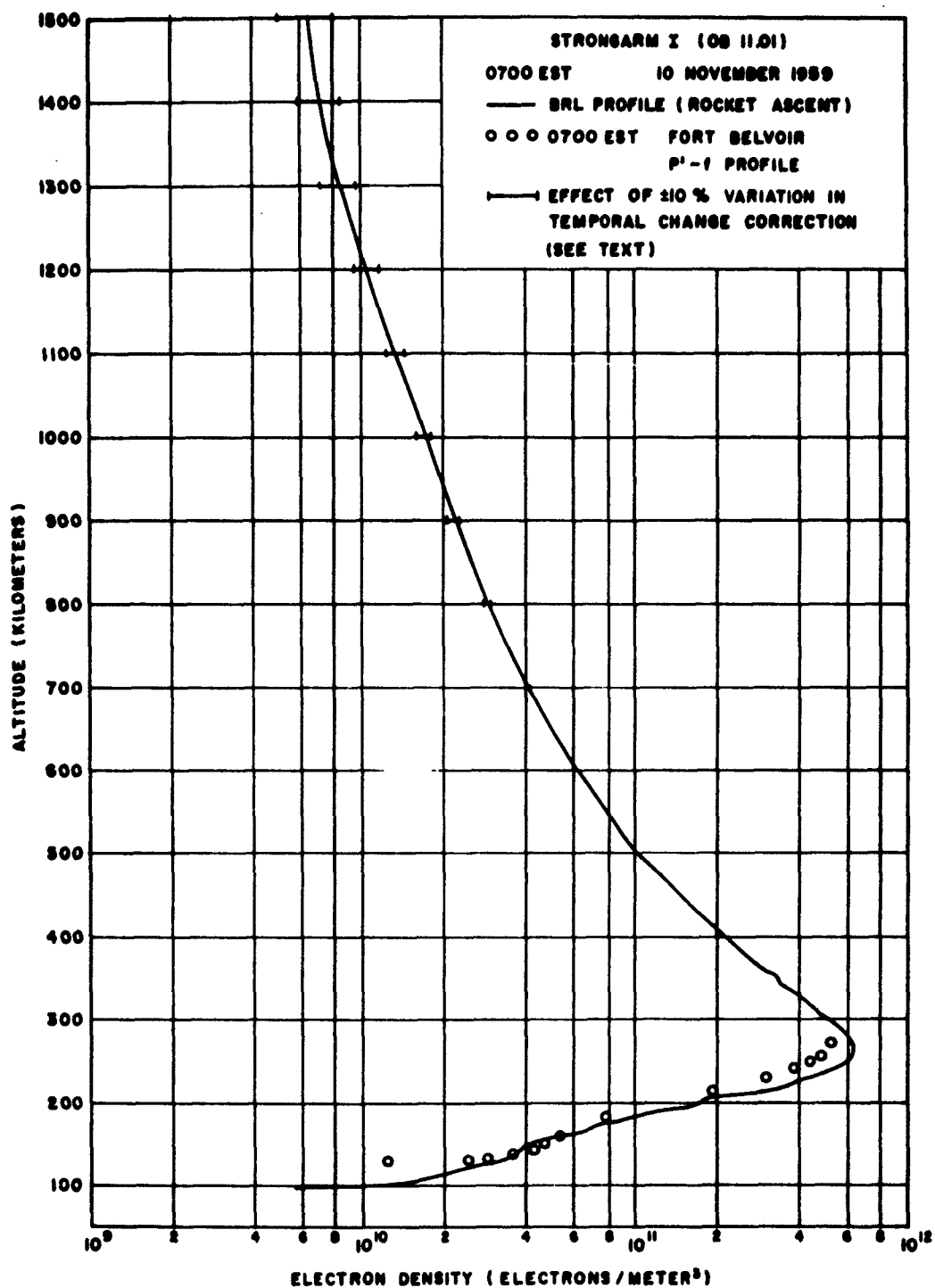


FIG. 9-2.  $N_{max}$  VERSUS TIME AT FORT BELVOIR (STRONGARM I FLIGHT)



**FIG.9-3. ELECTRON DENSITY PROFILE, STRONGARM I.**

An interesting study of the effects of temporal changes in ionization on a propagation experiment has been reported by Joosten et al.<sup>8</sup>. The authors used as one of their examples the preliminary Strongarm I electron density profile published by Cruickshank<sup>9</sup>. (This was the same profile reported by Berning<sup>7</sup>). Unfortunately, in drawing conclusions regarding that profile, Joosten apparently assumed that a correction for temporal variation had not been made in computing the profile. This assumption was in error since corrections were indeed applied as described by Berning<sup>7</sup>. The difference that may be noted between that preliminary profile and the one presented in this report arises from two sources, (1) the basically different methods of analysis of the dispersive Doppler data and (2) the use of a preliminary  $N_{\max}$  versus time profile in the earlier reduction rather than the more recently obtained electron density profiles from the Central Radio Propagation Laboratory (CRPL) that were used for the analysis reported here.

#### B. Strongarm III

Strongarm III, fired at 0946:53 EST on 13 July 1960, preceded by twenty-six hours the sudden commencement magnetic storm of 14-17 July. Geomagnetic conditions for a week prior to, and at the time of the flight were undisturbed.

Since Strongarm III did not tumble, good dispersive Doppler and Faraday rotation data were obtained throughout the flight. Figure 9-4 shows a section of a chart record from this flight which can be compared with Figure 9-1, a section of the Strongarm I chart. Part of Figure 9-4 was shown in greater detail in Figure 6-7.

Ionograms made at Fort Belvoir on the morning of the flight, show a strong, sometimes blanketing, sporadic E layer. One of these ionograms is shown in Figure 9-5. Since the  $N_{\max}$  versus time profile, Figure 9-6, seems to exhibit no significant, long term trend in  $N_{\max}$ , no temporal change correction was applied in computing the electron density profile.  $N_{\max}$  does appear to have undergone sharp variations at intervals of about 70 minutes. The variations are attributed to the movement of inhomogeneities in the ionosphere. These variations are further discussed below.

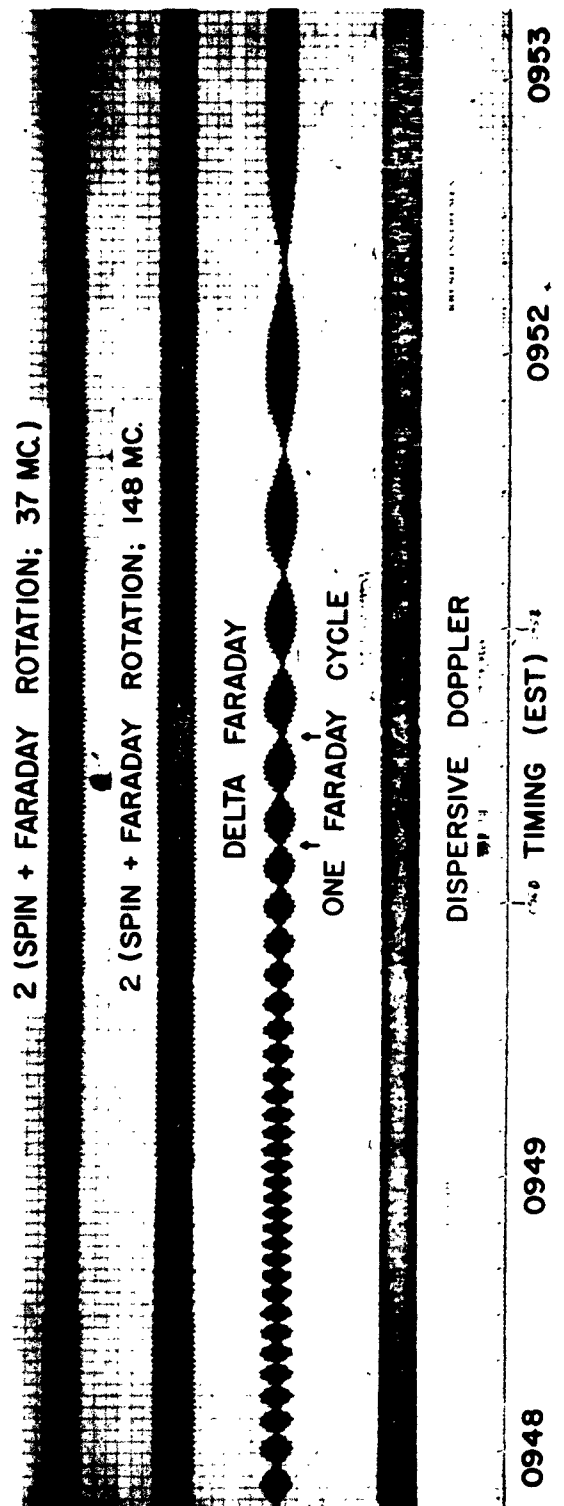


FIG. 9-4. SLOW SPEED CHART RECORDING, STRONGARM III



13 JUL 13 9 50 AM 1960

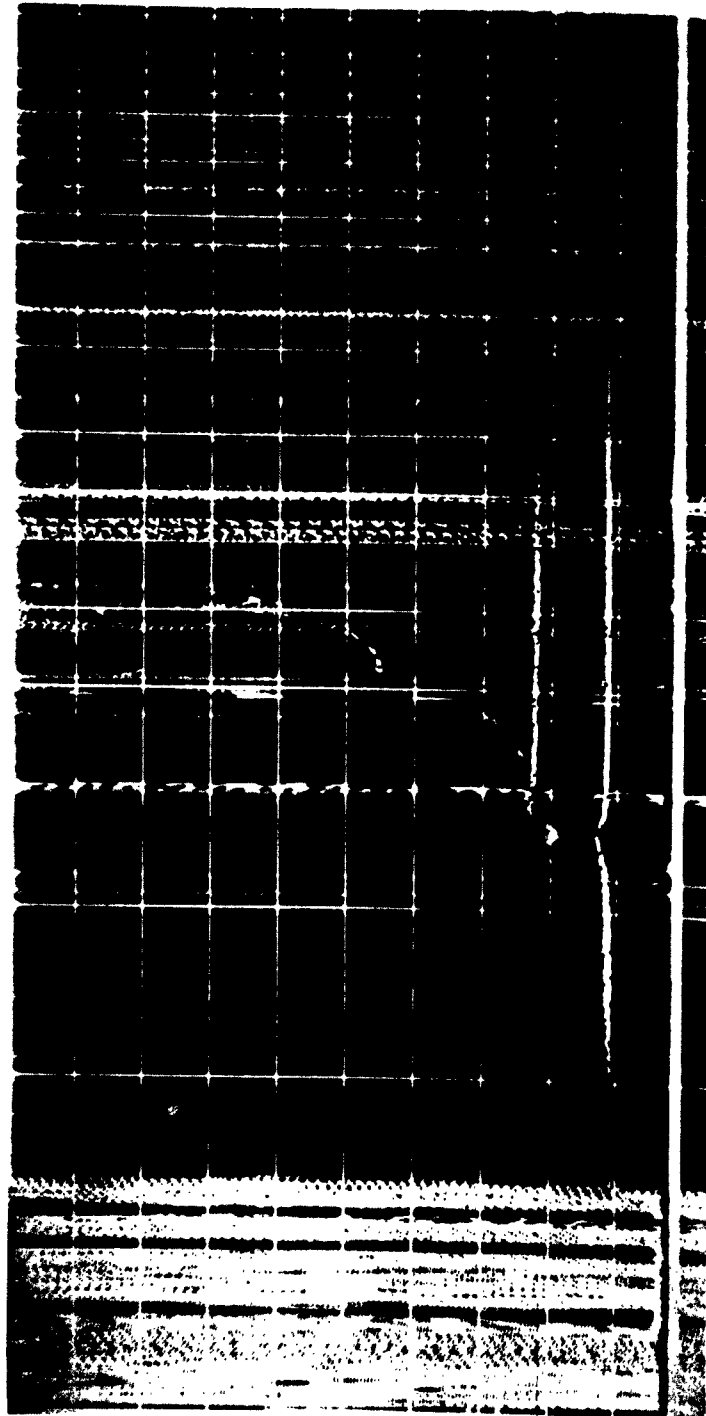


FIG. 9-5. IONOGRAM TAKEN AT FT. BELVOIR, STRONGARM III FLIGHT

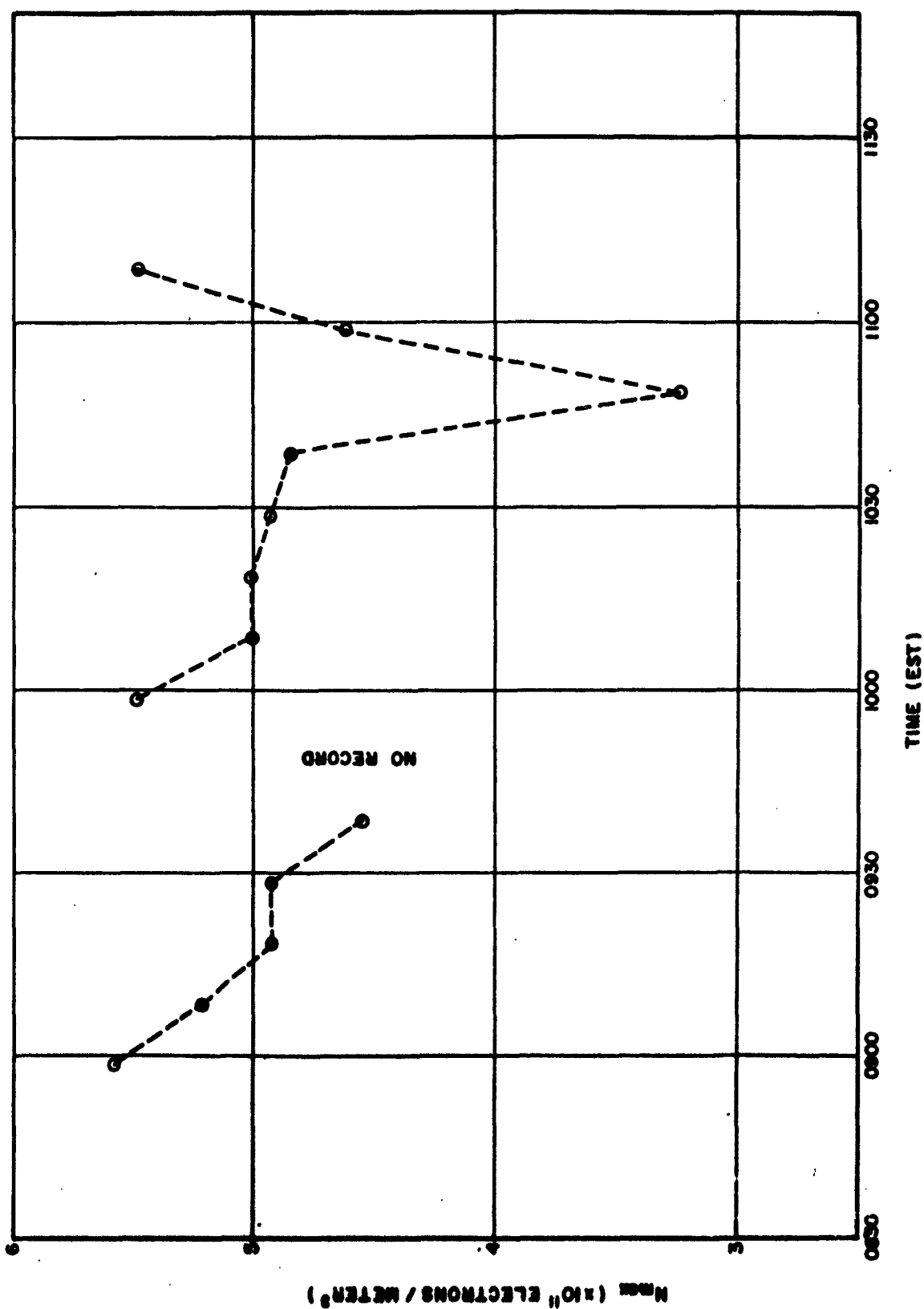
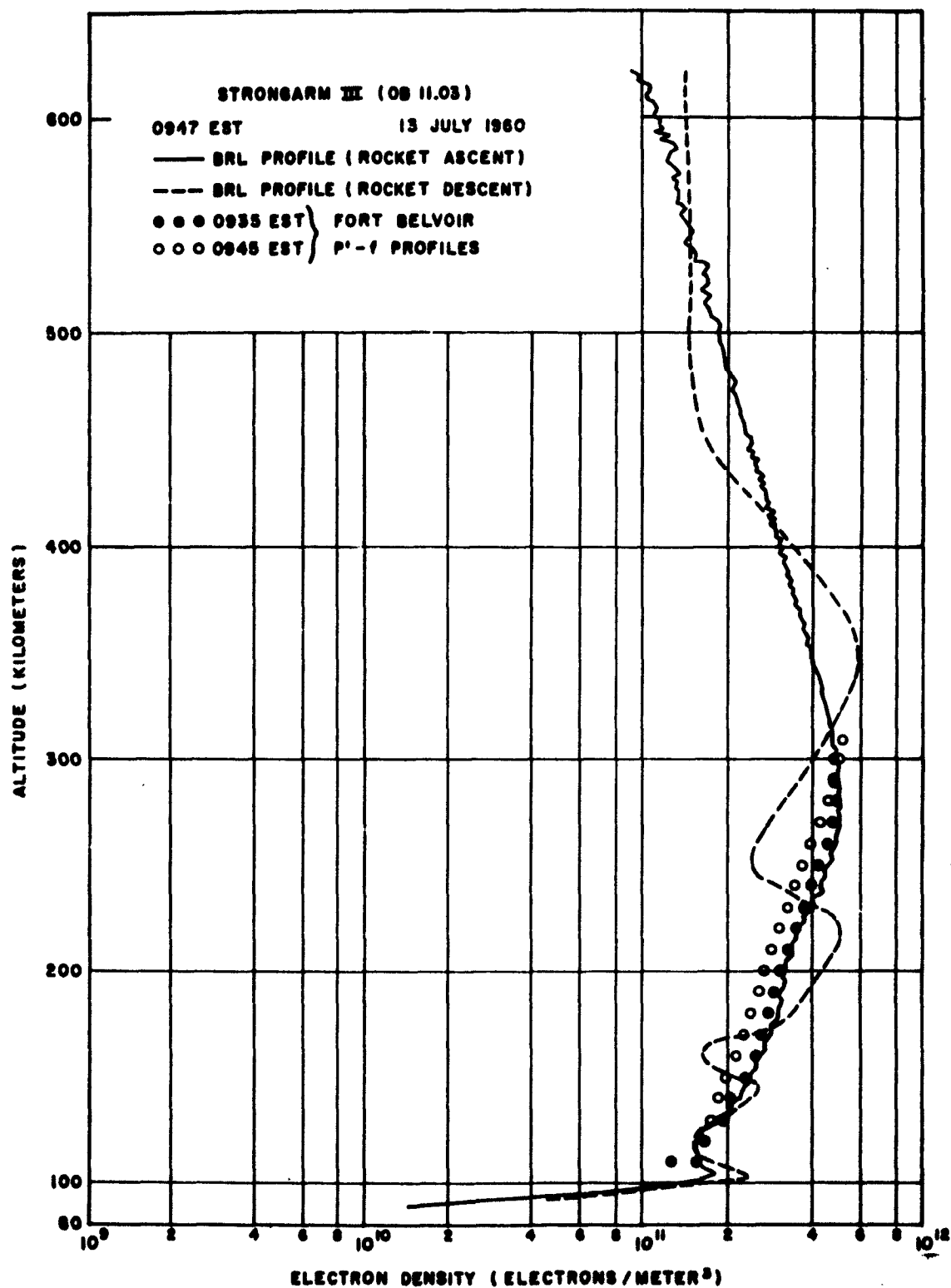


FIG. 9-6.  $N_{max}$  VERSUS TIME AT FORT BELVOIR (STRONGARM III FLIGHT)

Figure 9-7 shows the electron density profiles from the Strongarm III flight and the Fort Belvoir profiles at 0935 and 0945. These times would correspond to approximately 0928:30 and 0938:30, respectively, at Wallops Island if an adjustment were made for the solar time differential. No 0955 profile was available. Individual rocket data points are connected on the ascending profile and show the extent of scatter in the data. The descending profile, which is smoothed through the individual points, shows large variations in apparent electron density which are attributed to horizontal variations in ionization.

A preliminary attempt has been made to determine the probable nature of the horizontal variations. First, the upleg electron density profile shown in Figure 9-7 was used for the input to a ray tracing program. The program was used to compute the integrated dispersive Doppler and Faraday rotation for various rocket positions along the ascending part of the trajectory. Small adjustments (less than  $\pm 3\%$ ) were then made in the electron density profile until the computed integrated dispersive Doppler agreed within one cycle with the observed values throughout the entire ascent. Second, this new profile was used to trace rays on the descending part of the trajectory. Discrepancies of as many as 200 dispersive Doppler cycles were found between the computed and observed values. It was noted that the last major discrepancy corresponded in altitude to the lower portion of the F1 region and that the ascending profile seemed to show a pronounced F1 layer. The electron density model used in the ray tracing program was modified by increasing or decreasing the ionization in the model F1 region in a manner to bring the observed and computed integrated dispersive Doppler values into better agreement. This was done for a number of rocket positions during descent so that excellent agreement between the computed and observed integrated dispersive Doppler and Faraday rotation was obtained. The resulting regions of enhanced and diminished ionization, at an altitude of approximately 150-200 kilometers, were separated by approximately 150 kilometers horizontally (peak to peak), with a maximum variation of about two to one in local electron density at a given altitude. If the rocket descent data represent a cross section of field aligned inhomogeneities whose motion is responsible for the sharp variations in  $N_{\text{max}}$  observed at Fort Belvoir (Figure 9-6), this would imply that the inhomogeneities were moving with a



**FIG. 9-7. ELECTRON DENSITY PROFILE, STRONGARM III**

velocity of approximately 36 meters per second. A modification of the ray tracing program to permit use of a more sophisticated ionosphere model is presently being developed. When completed, the method will be applied to the Strongarm III data and the horizontal structure of the ionosphere more accurately determined.

Since the rocket vertical velocity in the E region was about 3 kilometers per second, the electron densities derived by differencing the integrated content at one second intervals are average electron densities over the three kilometer intervals. As a result, any fine structure with a thickness of much less than three kilometers is largely masked. In an attempt to find any fine structure that might be related to the sporadic E layer observed on the ionograms, the E region profile was recomputed using the much smaller time intervals required for 1 1/2 dispersive Doppler cycles instead of the one second intervals normally used. The result of this computation is shown in Figure 9-8 where the circles are the points obtained using the periods of 1 1/2 dispersive Doppler cycles and the crosses are those obtained using the usual one second interval. The sporadic E layer appears as a region approximately one kilometer thick in which the electron density is about 50% higher than that immediately above and below the layer. The electron density at the peak of the sporadic E layer is believed to be at least as high as that shown. Finer resolution might show the electron density to be as much as 15-20% higher still and the layer to be correspondingly thinner.

#### C. Strongarm IV

Strongarm IV was launched at 2143:24 EST on 13 July 1960, about twelve hours after the Strongarm III flight and fourteen hours before the magnetic storm of 14-17 July. Geomagnetic conditions at the time were still undisturbed.

Figure 9-9 shows the electron density profile from the Strongarm IV flight and the Fort Belvoir profiles at 2145 and 2159. These times would correspond to approximately 2138:30 and 2152:30 respectively at Wallops Island after adjustment for the solar time differential. No temporal change correction was applied in computing the Strongarm IV profile since the rate of change of  $N_{max}$ , as determined from P'-f profiles, was quite slow.

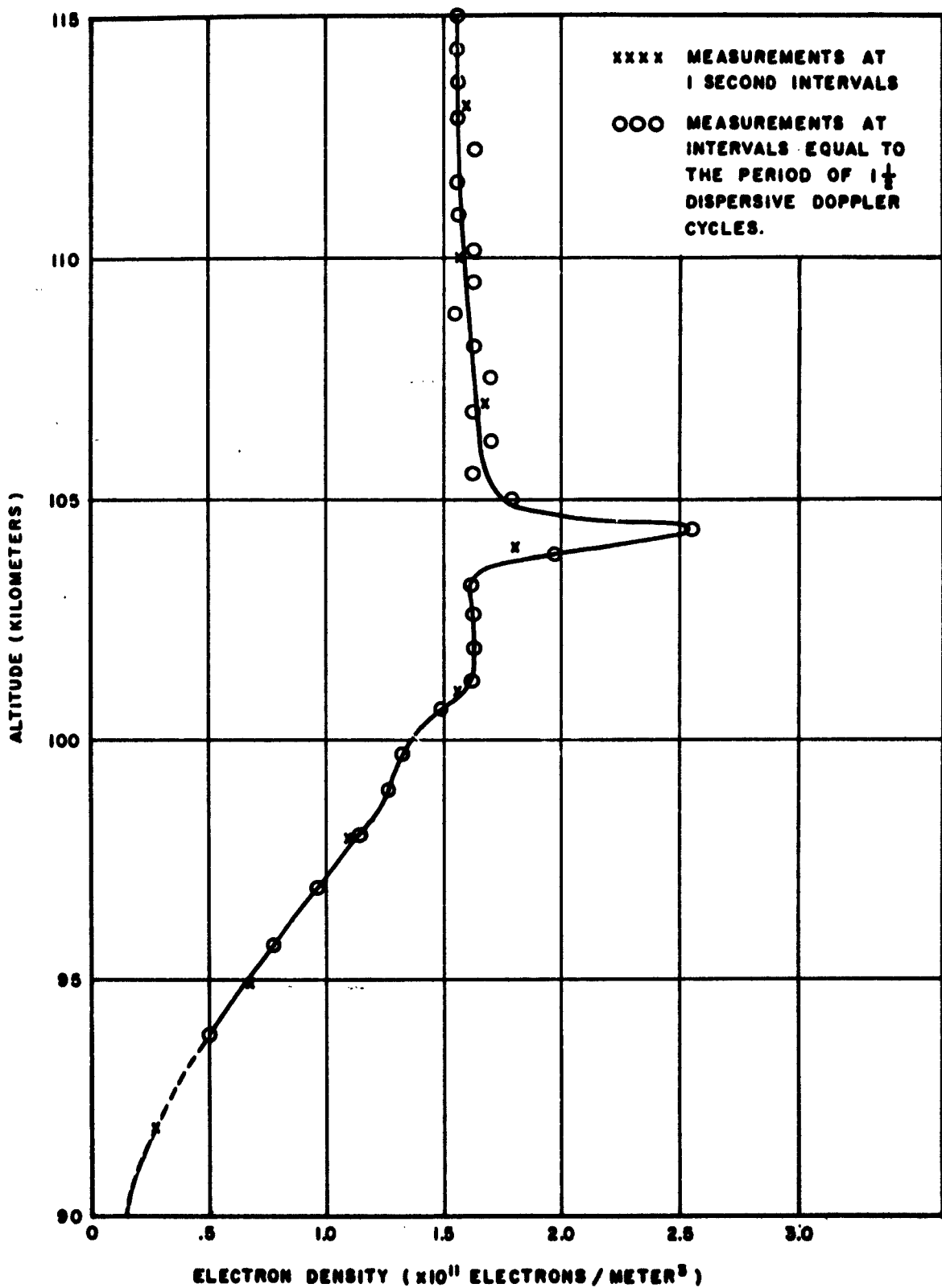
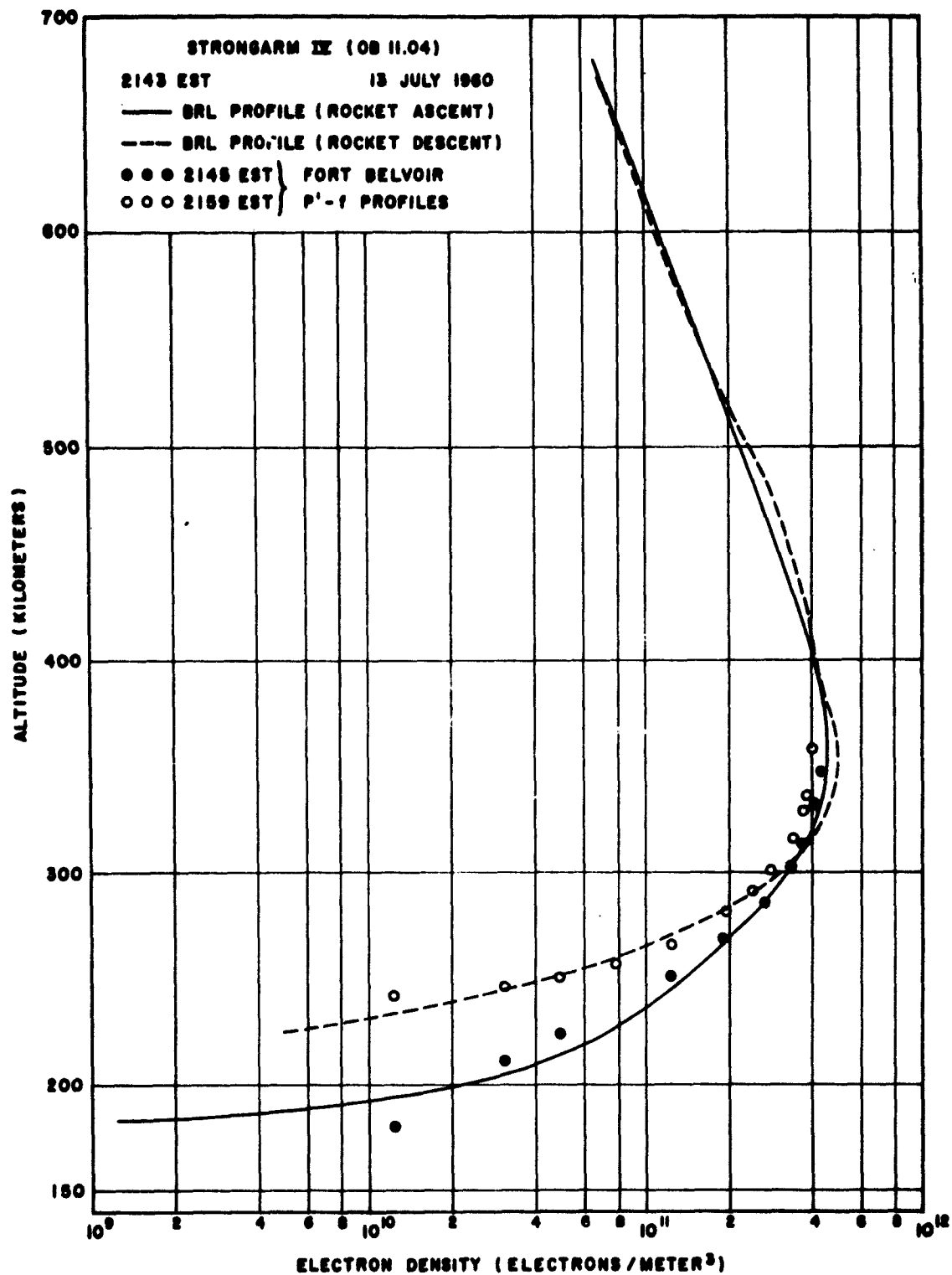


FIG. 9-B. E REGION ELECTRON DENSITY PROFILE, STRONGARM III



**FIG. 9-9. ELECTRON DENSITY PROFILE, STRONGARM IX**

The Strongarm IV precession, whose period varied from 118 to 145 seconds, caused the dispersive Doppler chart record to be unreadable periodically. Since the precession period was much longer than that for Strongarm I the sections of the dispersive Doppler data that could not be read from the chart were correspondingly longer making interpolation impractical. As a result, integrated dispersive Doppler data from the Transistorized Data Translator (TDT) were interspersed with data which could be read directly from the chart. Since the TDT integrated dispersive Doppler cycle counts have a scatter at least ten times that obtained using good chart data, only smoothed results are shown. The sections of the profile in Figure 9-9 requiring the least amount of smoothing occur at 360-495 kilometers during ascent, and 420-500 kilometers and above 580 kilometers during descent. Since the exact shape of the ascending profile above 495 kilometers is uncertain it has been shown as a straight line through the data points. While the exact shape of the ascending and descending profiles below  $F_{\max}$  is uncertain owing to scatter in the data a difference between the two is clearly evident. There were approximately 30-35 minutes difference in solar time between the points during ascent and descent when the rocket was at an altitude of 220 kilometers.



## X. DERIVED SCALE HEIGHTS AND EXOSPHERIC TEMPERATURES

### A. Derived Scale Heights

Several studies have recently been conducted in an effort to match experimental electron density profiles with various theoretical or empirical models of the ionosphere.<sup>10,11</sup> The familiar Chapman distribution with a constant scale height is usually the first approximation in these studies. The equation is:

$$N = N_{\max} \exp 1/2 (1-Z-e^{-Z}) \quad \text{where } Z = \frac{h-H_{\max}}{H}, \quad (12)$$

$H_{\max}$  is the height of the F2 peak,  $N_{\max}$  is the electron density at  $H_{\max}$ ,  $H$  is the "effective" or "Chapman" scale height, and  $N$  is the electron density at height  $h$ . Wright<sup>12</sup> stated that this simple Chapman distribution with a scale height of 100 km provides good agreement with data available up to 1960. Since that time there have been several experimental profiles of the ionosphere extending several hundred kilometers above the height of the F2 peak, and, except at night, the profiles vary considerably from the simple Chapman model. An example of this variation is shown in Figure 10-1, where the Strongarm III profile is compared with three Chapman models of effective scale height 60 km, 76.5 km, and 100 km, respectively. The curve of 60 km scale height provides a fairly good fit for about 100 km above  $H_{\max}$  but then lies to the left of the experimental data. The 76.5 km scale height curve lies to the right of the experimental data over most of the range above  $H_{\max}$  but crosses it at about 500 km. The 100 km scale height curve, though to the right of the experimental profile, when far above  $H_{\max}$  has nearly the same slope as the experimental profile.

For some purposes it is desirable to use geopotential altitude in place of the standard geometric altitude and to express scale heights in geopotential kilometers. It turns out that with proper choice of the scale heights in the two systems, the profile in terms of geopotential kilometers is essentially the same as that in terms of the geometric system. This is illustrated in Figure 10-1, where points calculated using the Chapman scale height of 87 geopotential kilometers are superimposed on the profile of scale height 100 km. Except in the lowest altitude range there is little difference. Therefore, unless otherwise specified, the quoted scale heights and altitudes are in terms of standard kilometers which are more convenient for calculations.

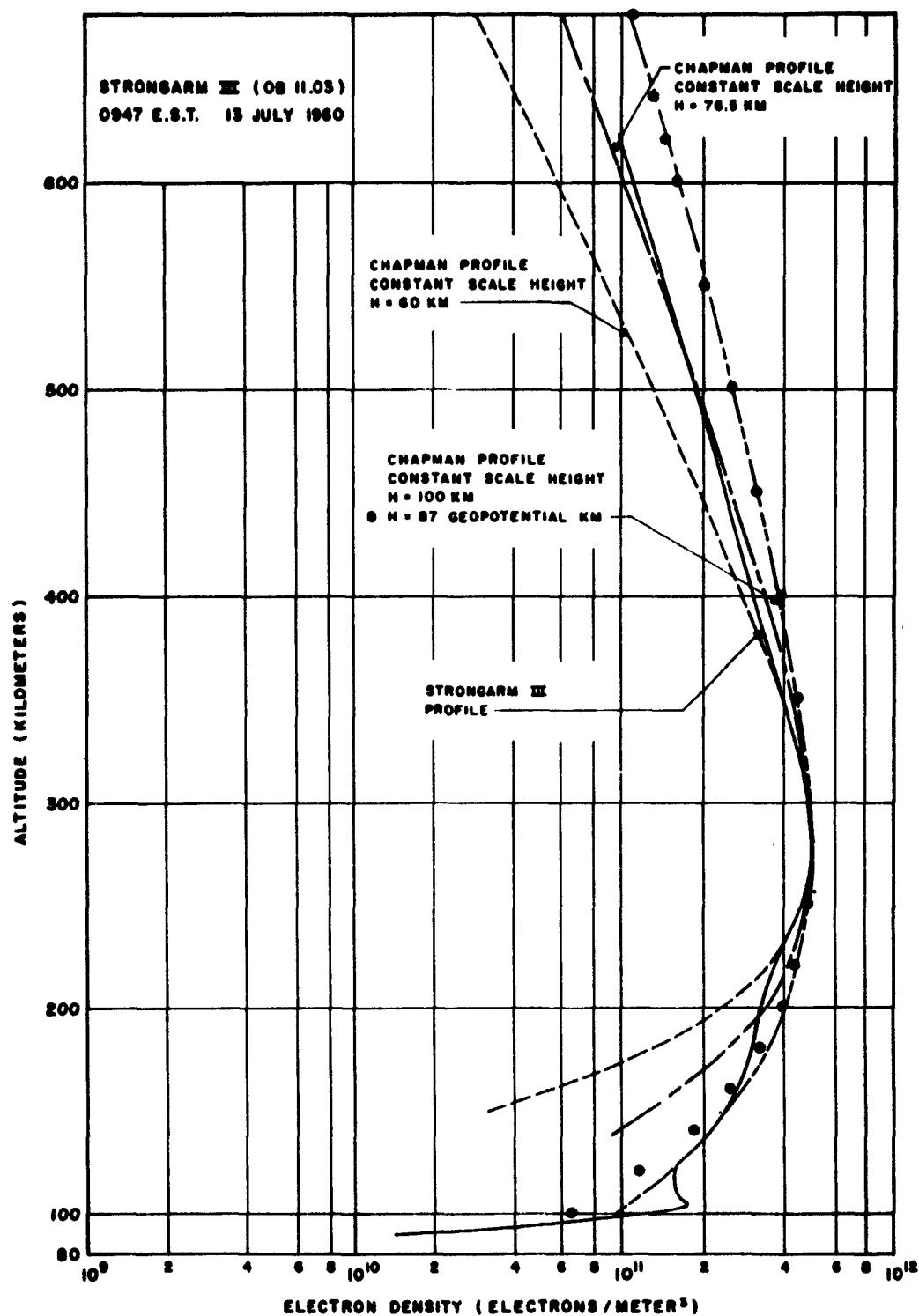


**FIG.10-1.COMPARISON OF STRONGARM III PROFILE WITH  
CHAPMAN LAYERS OF CONSTANT SCALE HEIGHT**

It has been found that an improved fit of the Chapman type profiles to the observed data is obtained if a gradient of the effective scale height is introduced into the Chapman formula (12), generalized by defining

$$Z = \int_{H_{\max}}^h \frac{dh}{H(h)} \quad (13)$$

In the case of the simple Chapman layer considered earlier,  $H$  is constant so that  $Z = \frac{h-H_{\max}}{H}$ . When the scale height gradient is constant,  $H = H_m + \gamma (h-H_{\max})$ , where  $H_m$  is the effective scale height near  $H_{\max}$ . Then for  $\gamma \ll \frac{H_m}{h-H_{\max}}$  (which is usually valid to about 1000 km), we have

$$Z = \frac{h-H_{\max}}{H_m + \frac{\gamma}{2} (h-H_{\max})} \quad (14)$$

The curves resulting from the use of the constant scale height gradient show excellent agreement with the experimental data to altitudes greater than 700 km. The major objection to its use is that the observed profiles appear to have a constant electron scale height at the higher altitudes, whereas the electron density derived from the Chapman formula with a constant scale height gradient has an increasing electron scale height. However, when the scale height gradient in the Chapman formula is not too large (less than .15 km/km) the departure of the derived profile from a constant electron scale height is negligible below 700 km, and at higher altitudes is consistent with a transition to a lighter ion as the predominant species.

It is now generally believed that in middle latitudes, within a few scale heights above  $H_{\max}$ , diffusion becomes the chief loss process and the region becomes isothermal.<sup>13, 14</sup> Also, in the altitude range from 200 km to approximately 1000 km, the predominant ion is the atomic oxygen ion.<sup>15</sup> In such an isothermal region with a single predominant ionized species, whenever diffusion of ions from a region is the dominant loss process, the downward diffusion tends to restore the hydrostatic gradient of concentration of the species, and hence tends to produce an exponential decrease of electron density, corresponding to the constant scale height of the ionized species. The scale

height should continue to be a constant up to altitudes where helium ions or protons become predominant. The altitude where the changeover occurs varies with temperature but is sufficiently high that it is of no concern here.<sup>16</sup>

The shape of the electron density profile near and below  $H_{\max}$  is dependent upon several factors. Whereas far above  $H_{\max}$ , downward diffusion is probably the chief loss mechanism, near  $H_{\max}$ , loss due to recombination or attachment, electromagnetic drift, and diffusion may all be important, since these several mechanisms act to produce the characteristic shape of the profile. Because the relative importance of the various processes is unknown, a theoretical model for the shape of the profile cannot yet be determined. Therefore, the most that can be expected is an empirical model with parameters describing the main features of the profile.

The advantages of using Equations (12), (13) and (14) to describe the electron density above  $H_{\max}$  are several:

1. The insertion of the scale height gradient of Equation (14) into Equation (12) produces an altitude range where the electron density decrease is exponential. This interval corresponds to the region where atomic oxygen is the predominant ionized species and diffusion is the predominant loss mechanism.
2. Near  $H_{\max}$  the distribution is nearly parabolic, in agreement with the models of F2 region consistent with ionogram data.
3. When  $\gamma = 0$  the formula reduces to the usual Chapman form.
4. The equations provide a very accurate fit to observed profiles as high as 1200 km and are convenient for machine computation. It is possible to derive values of  $H_m$  and  $\gamma$  to provide a good fit to an observed profile, or a profile can be found corresponding to known or assumed values of  $H_m$  and  $\gamma$ . Analysis of more data can determine the diurnal variation of  $H_m$  and  $\gamma$  and their variation throughout the sunspot cycle.

Figure 10-2 shows the agreement between the observed profiles of the Strongarm rocket series and the generalized Chapman formula. In all cases the Chapman curve is virtually indistinguishable from the observed data above  $H_{\max}$ . Below  $H_{\max}$  the electron density from the Chapman formula falls off more rapidly than does the observed electron density. The falloff is most rapid when the scale height gradient,  $\gamma$ , is large.

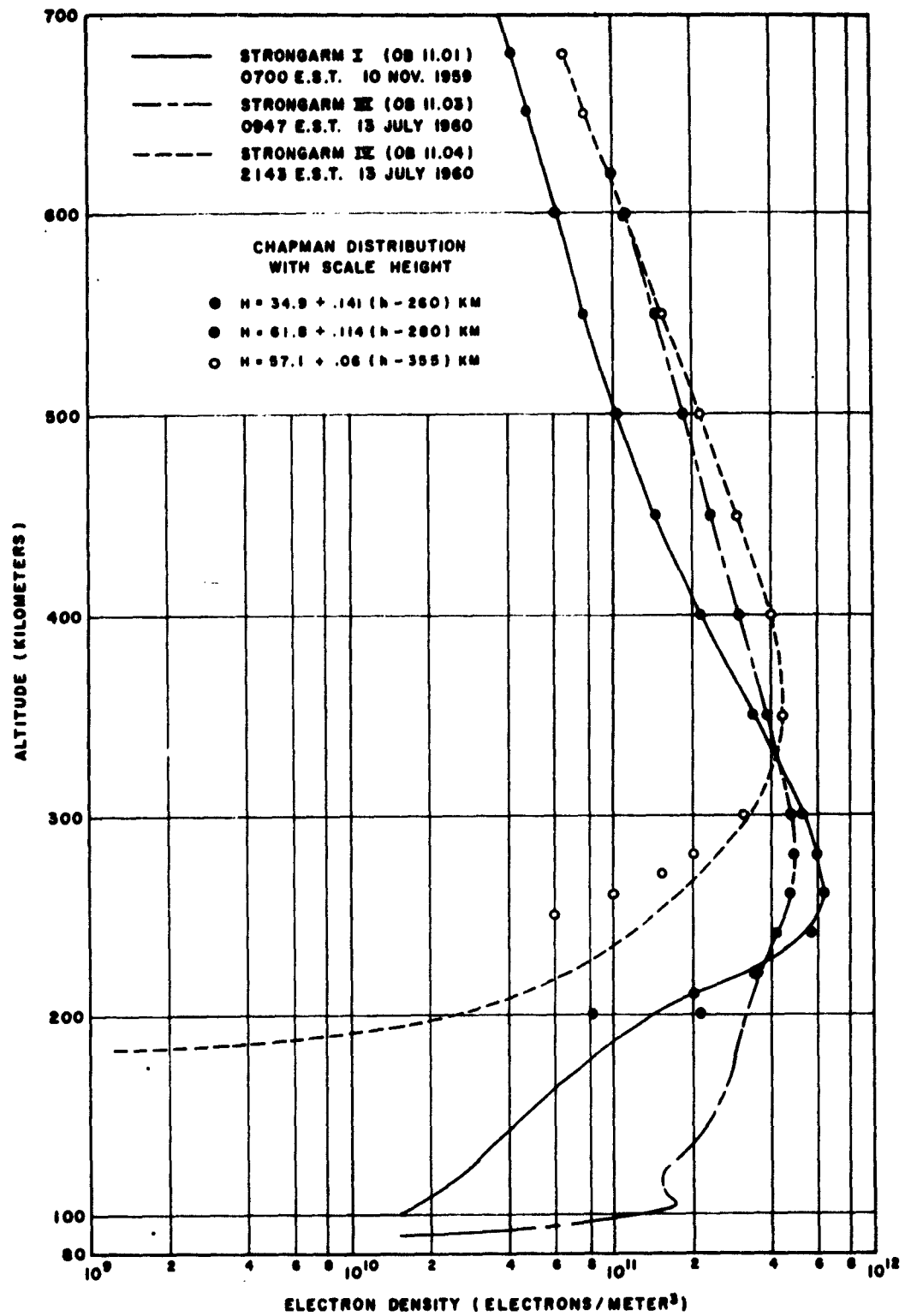


**FIG.10-2.COMPARISON OF STRONGARM PROFILES  
WITH CHAPMAN DISTRIBUTIONS.**

The nighttime profile (Strongarm IV) shows a nearly constant slope above about 450 km, corresponding to a constant scale height of the ionizable species. A similar result was obtained by Hanson and McKibben<sup>17</sup>, with an ion trap measurement at about 2000 hrs. In order to obtain a good fit of a Chapman type profile with the observed data above  $H_{\max}$ , it is necessary to introduce a small scale height gradient of .06 km/km. Below  $H_{\max}$  the fit is better with the scale height gradient equal to zero. Long<sup>18</sup> concludes from ionosonde data that the bottom side of the nighttime F region is closely approximated by a simple Chapman type distribution, which is in agreement with the present data.

The magnetically quiet daytime profile of Strongarm III is compared with the generalized Chapman profile in Figure 10-2. The agreement indicates that there is a gradient of the Chapman formula scale height of .114 km/km. From 350 km to 600 km there is an exponential decrease of electron density (constant slope on the semi-log plot). This exponential decrease is in agreement with the results of Jackson and Bauer<sup>19</sup>, and the model proposed by Seddon<sup>20</sup>, and indicates that diffusion is predominant above approximately 350 km.

The Strongarm I profile, being obtained about sunrise, is more complicated than the other two. The agreement of the observed data with a Chapman layer of constant scale height gradient is shown in Figure 10-2. At the time of the observation the ionosphere was not in equilibrium as evidenced by the fact that the electron density at  $H_{\max}$  as observed on a series of ionograms was changing rather rapidly. Hence, it would not be expected that the Chapman formula would apply. Figure 10-3 shows the Strongarm I profile and two additional curves similar to the Strongarm III and IV results and hence typical of the equilibrium nighttime and daytime profiles. Comparison of the curves illustrates that the transition from nighttime to daytime ionosphere in the F region is strikingly similar to the transition postulated from theoretical considerations by Watanabe and Hinteregger.<sup>21</sup> The slope of the profile above about 500 km is similar to that of a daytime profile, indicating that the transition to daytime temperatures is attained quite rapidly at higher altitudes. However, the low electron densities observed indicate that the build-up of ionization is considerably slower.

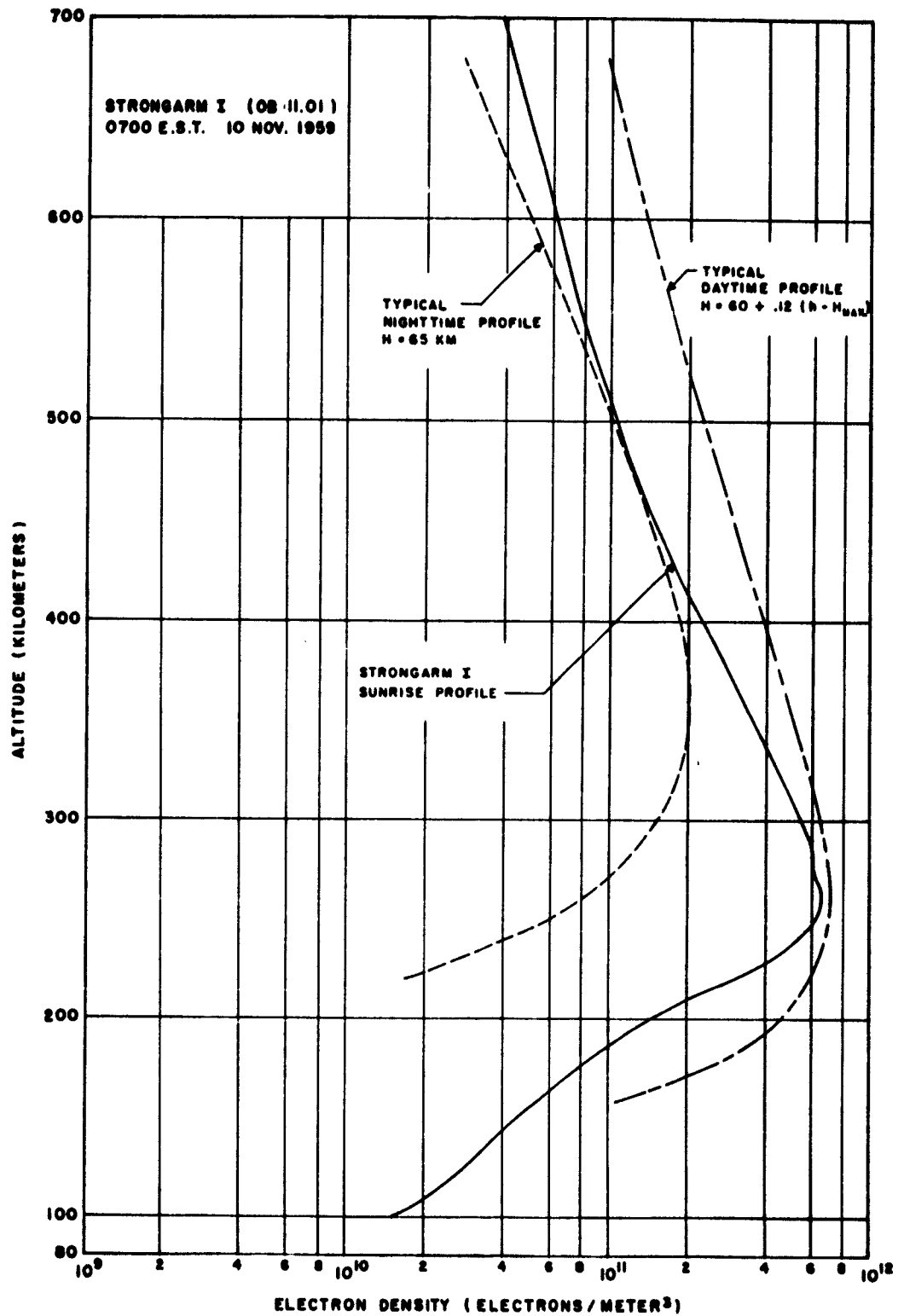


**FIG.10-3. COMPARISON OF STRONGARM I SUNRISE PROFILE  
WITH TYPICAL DAYTIME AND NIGHTTIME PROFILES**

### B. Exospheric Temperatures

The relationship between scale height and temperature is straightforward only when the region is isothermal, is in diffusive equilibrium, and when the magnetic dip angle is not close to zero. Then the scale height of the ionizable species is given by the equation:

$$H_i = \frac{k (T_e + T_i)}{(m_i + m_e) g} = \frac{2k}{mg} \frac{(T_e + T_i)}{2} \quad (15)$$

where  $k$  is the Boltzmann constant,  $m_e$  is the mass of the electron,  $m_i$  is the mass of the (oxygen) ion,  $m \doteq m_i$ ,  $T_i$  is the temperature of the ions (and neutral particles),  $T_e$  is the electron temperature, and  $g$  is the gravitational acceleration. The non-constancy of  $g$  can be compensated for by introducing "reduced" or "geopotential" altitudes by the formula  $h' = \frac{R_E h}{R_E + h}$  where  $R_E$  is the earth's radius.

In Table I are shown the values of diffusive scale height and temperature derived from the observed electron density profiles by use of Equation (15). Harris and Priester have shown that the upper atmosphere temperature is correlated with the observed 10.7 cm solar flux.<sup>22</sup> The temperatures derived from the values of flux observed at the time of the rocket flights are also given in Table I, and are seen to be somewhat lower than those derived from Equation (15). The reason for the discrepancy may be (1) that thermal equilibrium did not exist at the time of flight, or (2) that the derivation of temperature from solar flux data is not accurate at the present time. If the former case be true, the electron temperature can be estimated by assuming that the neutral gas temperature and the ion temperature are equal and by comparing the values of  $(T_e + T_i)/2$  with the gas temperature from 10.7 cm flux data. It is probable that the inaccuracy of the derivation of the temperature from solar flux data would make numerical estimates unreliable; however, it is indicated that electron temperatures are higher than gas temperatures by a factor of about 1.4.

Below the region where diffusion is predominant, the relation between the scale height of the Chapman formula and the atmospheric temperature is not simple. For a non-isothermal region, or a region in nonthermal equilibrium,



TABLE I

## DIFFUSIVE SCALE HEIGHTS AND TEMPERATURES

ROCKET	Temp. Derived From Electron Density Profile (deg. K) **	Temp. Derived From 10.7 cm Solar Flux (deg. K)	10.7 cm Solar Flux *	Chapman Scale Height at $H_{max}$ (km)	Ionizable Species Scale Height $H_i$ (geopotential km)	Chapman Scale Ht. Gradient (km/km)
Strongarm I	1600	1400	190	34.9	85	0.141
Strongarm III	1600	1350	140	61.8	85	0.114
Strongarm IV	1180	950	140	57.1	63	0.06

\*  $\frac{\text{Watt}/M^2/\text{Cycle/second}(\times 10^{-22})}{T_e + T_i}$

\*\*  $\frac{T_e + T_i}{2}$

it has been suggested by Van Zandt (private communication) that a temperature correction term should be applied to the Chapman formula Equation (12). It is probable that the region near  $H_{\max}$  is not a true  $\alpha$  Chapman type with recombination as the primary loss mechanism<sup>24,25</sup>. Therefore, it is fortuitous that the Chapman formula provides a good model near  $H_{\max}$ , but one cannot say that Equation (15) expresses the correct relationship between the scale height in the Chapman formula and the atmospheric temperature. For this reason temperatures are quoted only in the isothermal region where diffusion is pre-dominant.

#### ACKNOWLEDGMENTS

The Ballistic Research Laboratories wish to express their appreciation to the National Aeronautics and Space Administration for the use of their Wallops Island launching facility; to the personnel of the North Atlantic Radio Warning Service and ionosphere station at Fort Belvoir, Virginia, who provided a special series of ionosphere soundings in support of each Strongarm flight; to personnel of the Central Radio Propagation Laboratory, National Bureau of Standards, who carried out the reduction of the Fort Belvoir ionograms to provide the true height profiles used in this report; and to the personnel of the Millstone Hill Radar Station of Lincoln Laboratory, Massachusetts Institute of Technology, whose tracking results were of great value in determining the trajectories of Strongarms III and IV.

*Spence T. Marks*  
SPENCE T. MARKS

*Charles E. Shafer*  
CHARLES E. SHAFER

*William J. Cruickshank*  
WILLIAM J. CRUICKSHANK

*Raymond E. Prenatt*  
RAYMOND E. PRENATT

*George A. Dulk*  
GEORGE A. DULK  
Capt, Ord Corps

## XI. BIBLIOGRAPHY

1. Berning, W. W. Determination of Ionospheric Charge Densities from DOVAP Records. Ballistic Research Laboratories Report No. 745, November 1957.
2. Berning, W. W. Charge Densities in the Ionosphere From Radio Doppler Data. Journal of Meteorology, 8: 175-181, June 1961.
3. Berning, W. W. The Determination of Charge Density in the Ionosphere by Radio Doppler Techniques. (Rocket Exploration of the Upper Atmosphere, Boyd, R. L. F. and Seaton, M. J., Editors, pp. 261-273. London, Pergamon Press, 1954).
4. Berning, W. W. Earth Satellite Observations of the Ionosphere. Proc. IRE, 47: 280-288, February 1959.
5. Prenatt and Mester. Measurements of Electron Density From IGY DOVAP Records. Ballistic Research Laboratories Report in Preparation.
6. Seddon, J. C. Propagation Measurements in the Ionosphere with the Aid of Rockets. Journal of Geophysical Research, 58: 323-335, September 1953.
7. Berning, W. W. A Sounding Rocket Measurement of Electron Densities to 1500 Kilometers. Journal of Geophysical Research, 65: 2589-2594, September 1960.
8. Joosten, W. L., Atmore, R. F. and Telles, D. S. A Study of Time Errors Introduced Into Electron Density Profiles Measured by Rocket Borne Propagation Techniques. Physical Science Laboratory, New Mexico State University, October 26, 1960.
9. Cruickshank, W. J. Instrumentation Used For Ionosphere Electron Density Measurements. Ballistic Research Laboratory Technical Note No. 1317, May 1960.
10. Garriott, O. K. Proc. of the First International Space Science Symposium. Nice, 1960.
11. Chandra, S. Electron Density Distribution in the Upper F region. NASA Publication X-615-62-90, 14 June 1962.
12. Wright, J. W. A Model of the F Region Above  $H_{\max}$  F2. Journal Geophys. Res., 65: 1, 185-192, January 1960.
13. Bauer, S. J. On the Electron Density Distribution Above the F2 Peak (Revised). NASA Technical Note D-1171, January 1962.
14. Sissenwine, N., Dubin, M. and Wexler, H. The U. S. Standard Atmosphere, 1962. Journal of Geophys. Res., 67: 9, 3627-3630, August 1962.

15. Hanson W. B. Upper Atmosphere Helium Atoms. *Journal Geophys. Res.*, 67: 1, 183-188, January 1962.
16. Bourdeau, R. E. and Bauer, S. J. Structure of the Upper Atmosphere Deduced from Charged Particle Measurements on Rockets and the Explorer VIII Satellite. Presented at the Third International Space Sciences Symposium, Washington, D. C., May 1962. (NASA Publ. X-615-62-18)
17. Hanson, W. B. and McKibbin, D. D. An Ion Trap Measurement of the Ion Concentration Profile Above the F2 Peak. *Journal of Geophys. Res.*, 66: 6, 1667-1672, June 1961.
18. Long, Audrey R. The Distribution of Electrons in the Nighttime Ionosphere. *Journal Geophys. Res.*, 67: 989-998, March 1962.
19. Jackson, J. E. and Bauer, S. J. Rocket Measurement of a Daytime Electron Density Profile up to 620 km. *Journal of Geophys. Res.*, 66: 9, 3055-3057, September 1961.
20. Seddon, J. C. The Quiet Ionosphere. Presented at the Spring Meeting of U.R.S.I., Washington, D. C., May 1962.
21. Watanabe, K. and Hinteregger, H. E. Photoionization Rates in the E and F Regions. *Journal Geophys. Res.* 67: 3, 999-1006, March 1962.
22. Harris, I. and Priester, W. Theoretical Models for the Solar-Cycle Variation of the Upper Atmosphere. *Journal Geophys. Res.*, 67: 12, 4585-4592, November 1962.
23. Evans, J. V. Diurnal Variation of the Temperature of the F Region. *Journal of Geophys. Res.* 67: 12, 4914-4920, November 1962.
24. Ratcliffe, J. A., editor. *Physics of the Upper Atmosphere*. New York: Academic Press, 1960.
25. Rishbeth, H. and Barron, D. W. Equilibrium Electron Distributions in the Ionospheric F2-layer. *Journal Atm. and Terr. Phys.*, 18: 213, 234-244, June 1960.

## XII. APPENDIX

### STRONGARM ASSEMBLY\*

A. The Preliminary Strongarm Assembly Procedures were as follows:

1st Stage. (1) The warhead pedestal (which contains four live spin rockets) was removed from the Honest John rocket; (2) The cant was removed from the Honest John fins by modifying the bolt holes of the fin support fittings; (3) A fin alignment check was conducted; (4) New forward and aft launch fittings were installed; and (5) The first-to-second stage coupling unit was fitted to the first stage. A sketch of this coupling unit is shown in Figure 12-1.

2nd Stage. (1) The thrust structure was removed from the Nike-Hercules booster unit; (2) The fin shroud and fin attachment fittings (including studs) were removed; (3) A new four-fin assembly was installed; (4) A fin alignment check was conducted; (5) A spacer ring and pressure seal were installed in the nozzle; (6) A pressure test was conducted; (7) Grain movement limiting blocks were installed; (8) A forward launch fitting was installed; and (9) The second-to-third stage coupling unit was fitted to the second stage. A sketch of this coupling unit is shown in Figure 12-2.

3rd Stage. (1) The first seven operations listed above for the second stage assembly were repeated for the third stage assembly without change. These operations were followed by the fitting of the second-to-third stage coupling unit to the third stage, and the installation of an interstage locking device on the coupling unit.

4th Stage. (1) The nozzle and flared skirt were installed on the Yardbird rocket; (2) The Yardbird igniter was checked and installed; (3) The nozzle closure was installed; (4) The blowout diaphragm was installed; (5) The third-to-fourth stage coupling unit (Figure 12-3) was installed on the fourth stage; (6) A pressure switch mounting plate was installed on the head end of the Yardbird rocket.

---

\* A condensed version of the Strongarm assembly procedures is given here. More detailed assembly procedures can be obtained from University of Michigan report No. 2816: 004-1-F by W.H.Hansen and F.F.Fischback entitled "The Strongarm Rocket", dated May 1960.

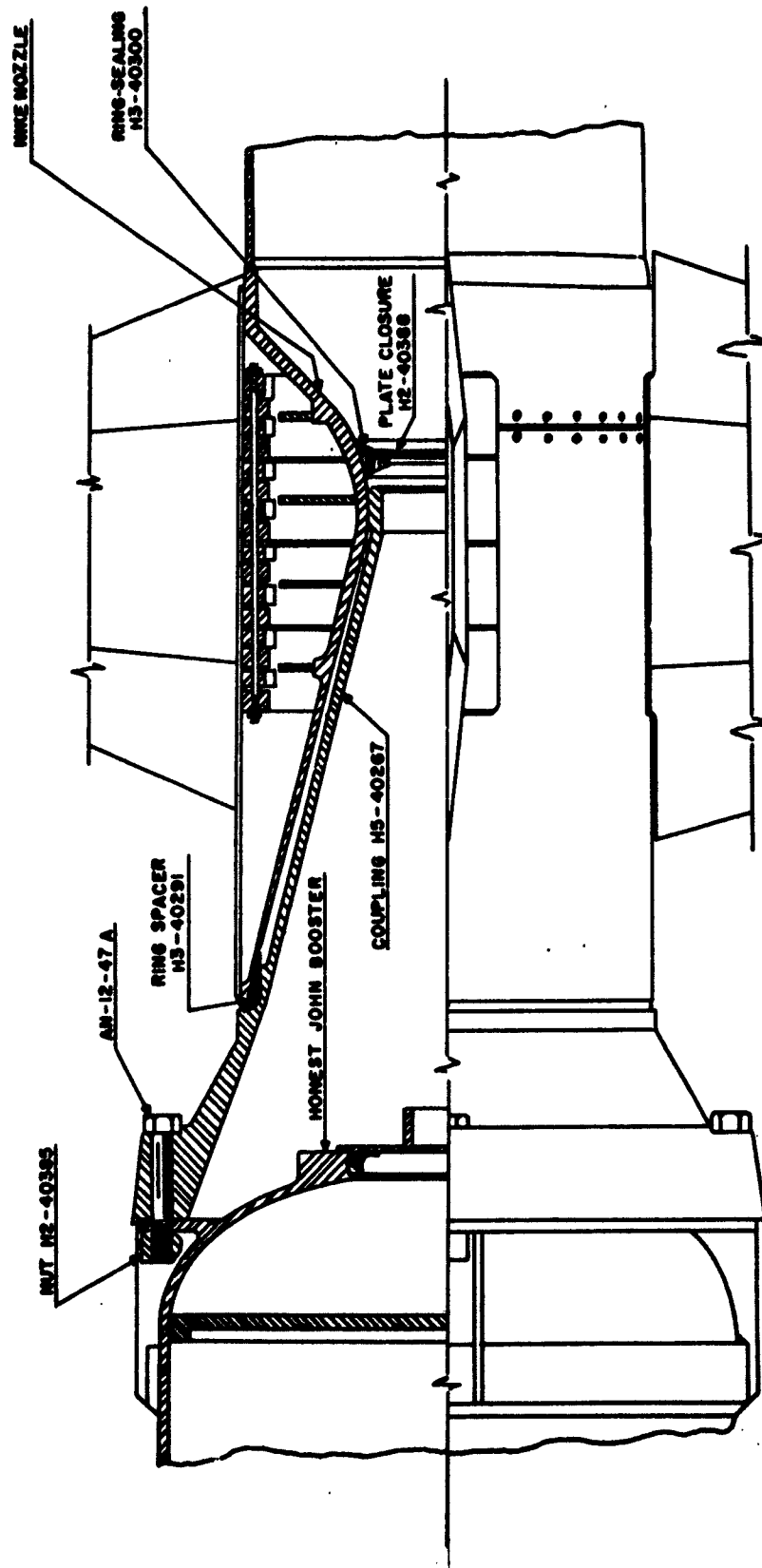


FIG. 12-1-1. FIRST TO SECOND STAGE COUPLING UNIT.

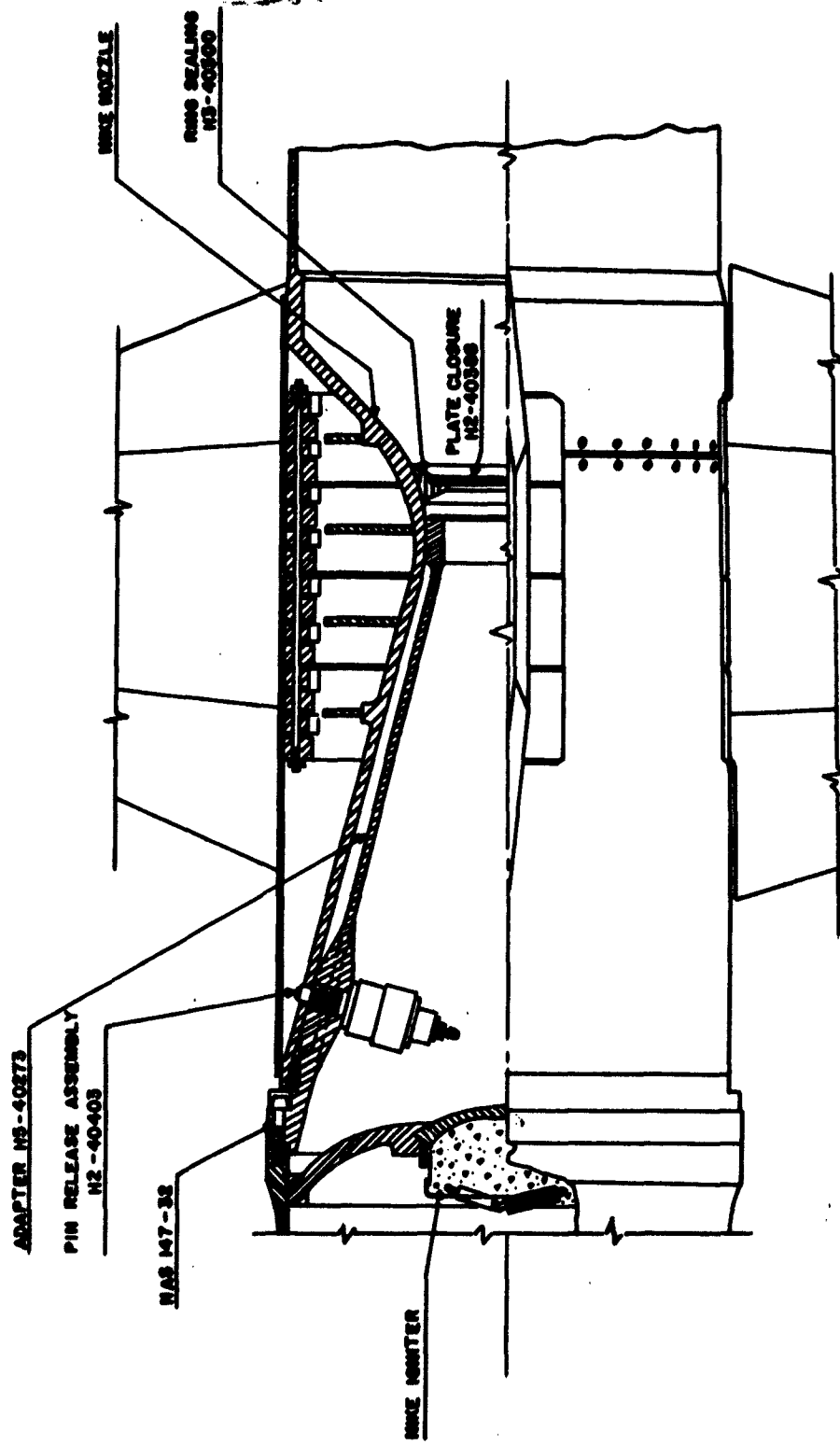


FIG. 12-2. SECOND TO THIRD STAGE COUPLING UNIT.



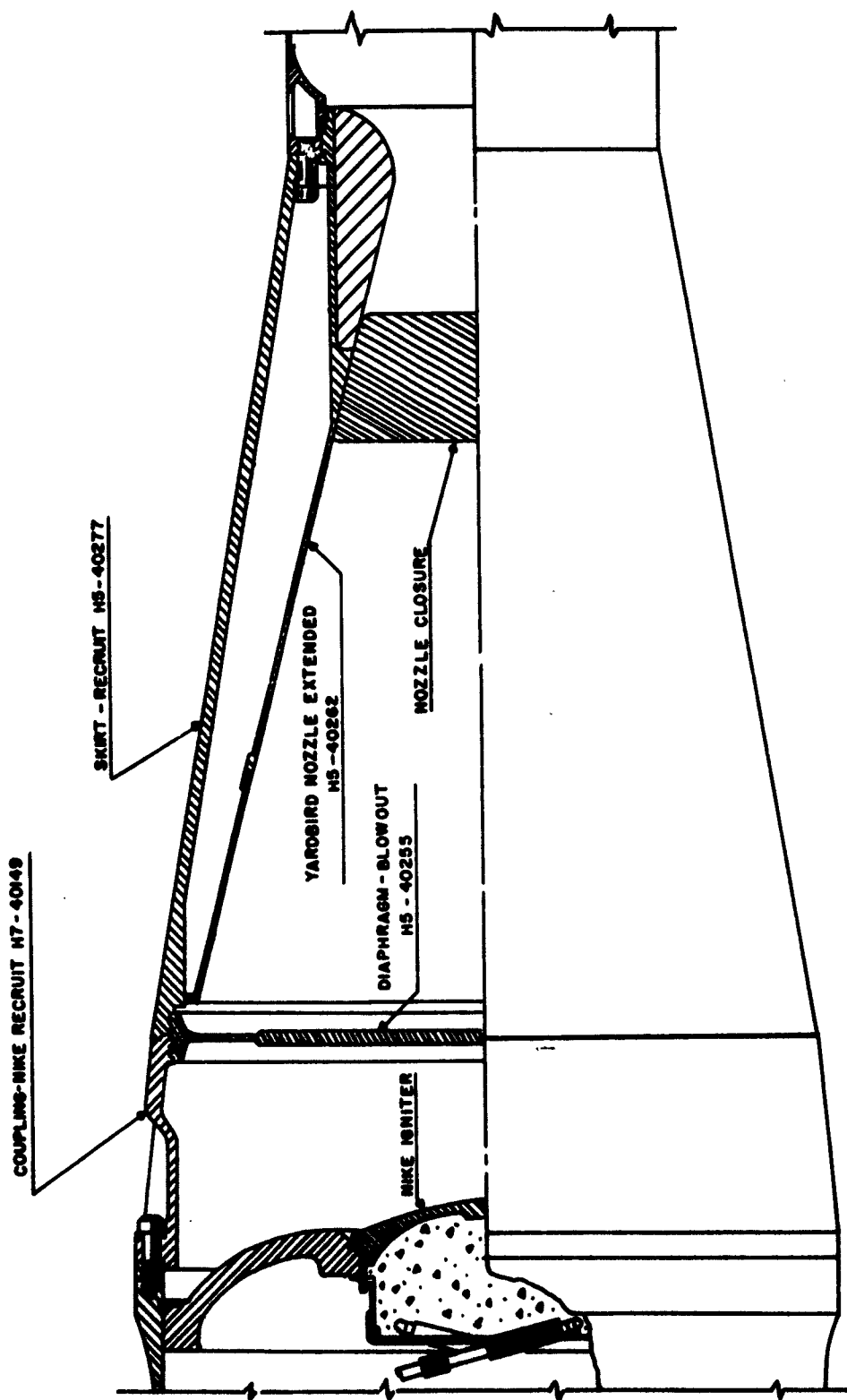


FIG. 12-3. THIRD TO FOURTH STAGE COUPLING UNIT.

5th Stage. (1) The igniter was checked and installed on the Scale Sergeant rocket; (2) The nozzle was installed; (3) A pressure check was conducted; (4) The flared skirt was installed; (5) The nose cone was installed; (6) The blowout diaphragm was installed; and (7) The fourth-to-fifth stage coupling unit was installed on the fifth stage. A sketch of this coupling unit is shown in Figure 12-4.

B. The Final Strongarm Assembly Procedures were as follows:

1st Stage. (1) The first stage was attached to the launcher boom by raising it on a dolly, and engaging the fore and aft launch fittings; (2) The first stage igniter was checked, and installed; (3) The front end closure was installed; and (4) The first-to-second-stage coupling unit was installed on the first stage.

2nd Stage. (1) The second stage was attached to the launcher boom by raising it on a dolly, mating the second stage nozzle with the first-to-second stage coupling unit, and engaging the forward launch fittings; (2) The second stage igniter was checked, and installed; (3) The igniter firing lines were brought out through a rail lug hole, to the launcher boom; (4) The pressure base with stage lock attached was connected to the pressure tap on the second stage; (5) The second-to-third stage coupling unit was installed on the second stage; and (6) The stage lock assembly was threaded into the coupling unit.

3rd Stage. (1) The third stage was mated with the second stage by raising it into position on a dolly; (2) The stage lock pin was screwed into place; (3) The third stage igniter was checked and installed; and (4) The firing lines were installed.

4th and 5th Stages. (1) The fourth and fifth stages were joined together in the assembly building and brought to the launcher as a unit; (2) The Yardbird-Scale Sergeant was raised on a dolly to the level of the first three stages, and positioned six inches away; (3) The pressure base from the pressure switch was connected to the pressure tap on the third stage; (4) The firing line plug and socket were connected; and (5) The third-to-fourth stage coupling unit was bolted to the third stage, completing the assembly.

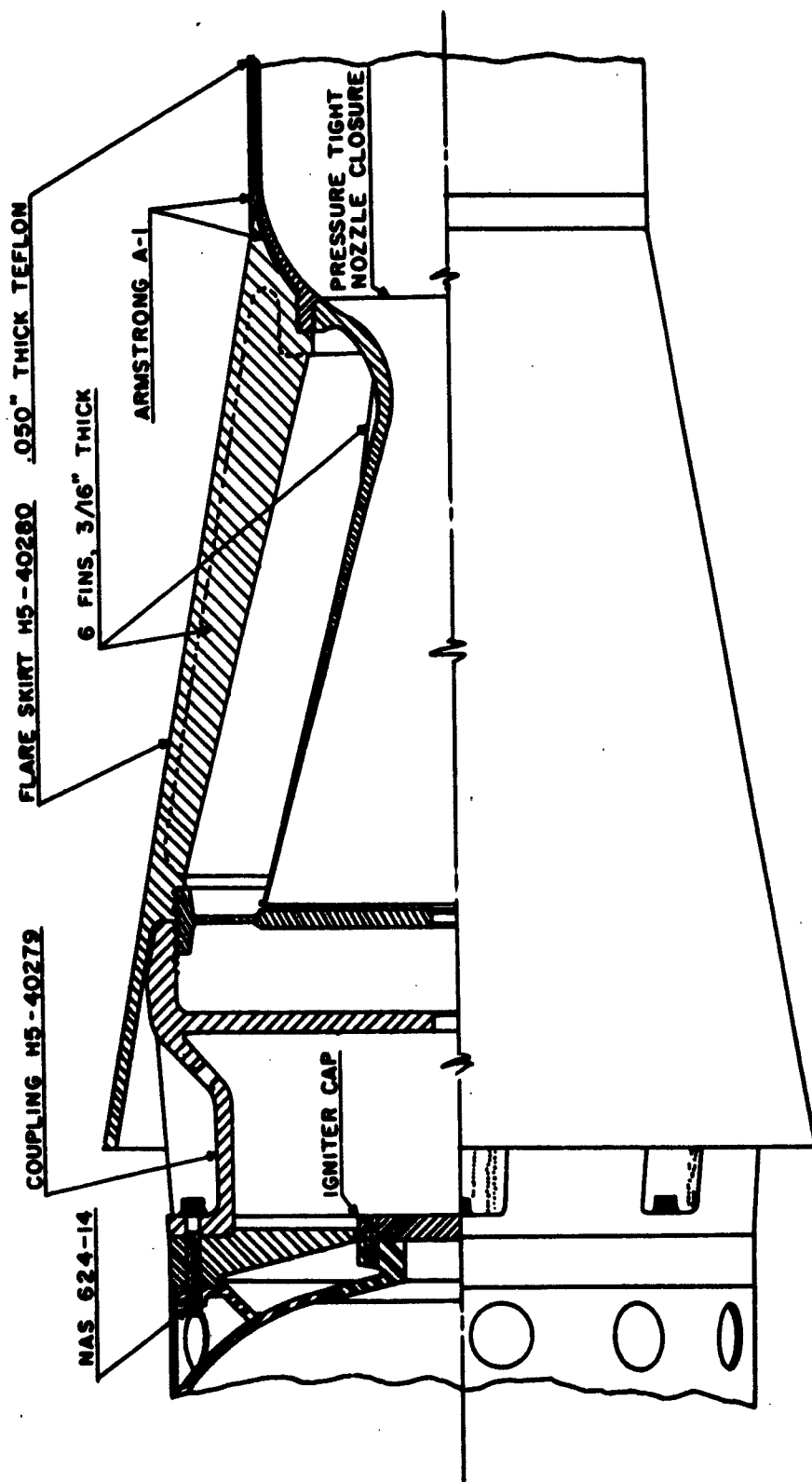


FIG. 12-4. FOURTH TO FIFTH STAGE COUPLING UNIT.

# DISTRIBUTION LIST

<u>No. of Copies</u>	<u>Organization</u>	<u>No. of Copies</u>	<u>Organization</u>
20	Commander Armed Services Technical Information Agency ATTN: TIPCR Arlington Hall Station Arlington 12, Virginia	1	Commanding General U. S. Army Materiel Command ATTN: Development Division, Missile Branch Washington 25, D. C.
2	Director Advanced Research Projects Agency ATTN: Lt Col Roy Weidler Department of Defense Washington 25, D. C.	2	Commanding General U. S. Army Materiel Command ATTN: AMCRD-RS-PE-Bal AMCRD-RS-ES-A Research and Development Directorate Washington 25, D. C.
2	Director IDA/Weapon Systems Evaluation Group Room 1E875, The Pentagon Washington 25, D. C.	1	Commanding Officer Harry Diamond Laboratories ATTN: Technical Information Office, Branch 012 Washington 25, D. C.
7	Chief, Defense Atomic Support Agency ATTN: Document Library Branch (5 cys) Major B. McCormac, Radiation Division Major J. E. Mock Washington 25, D. C.	1	Redstone Scientific Information Center ATTN: Chief, Document Section U. S. Army Missile Command Redstone Arsenal, Alabama
1	Commanding General Field Command Defense Atomic Support Agency ATTN: Major J. G. McCray Sandia Base P. O. Box 5100 Albuquerque, New Mexico	2	Commanding Officer U. S. Army Electronics R&D Activity White Sands Missile Range, New Mexico
1	Chief of Research & Development ATTN: Communications and Electronics Division Department of the Army Washington 25, D. C.	1	Director Research Analysis Corporation ATTN: Library 6935 Arlington Road Bethesda 14, Maryland
1	Commanding General U. S. Army Materiel Command ATTN: Development Division, Nuclear Branch Washington 25, D. C.	1	Chief Signal Officer Department of the Army Washington 25, D. C.
		3	Commanding General U. S. Army Electronics Command Fort Monmouth, New Jersey

# DISTRIBUTION LIST

<u>No. of Copies</u>	<u>Organization</u>	<u>No. of Copies</u>	<u>Organization</u>
1	Director, Office of Special Weapons Developments U. S. Continental Army Command Fort Bliss, Texas	2	Commander Naval Ordnance Laboratory White Oak Silver Spring 19, Maryland
2	Commanding Officer Army Research Office (Durham) ATTN: Dr. Robert Mace Dr. H. Robe Box CM, Duke Station Durham, North Carolina	1	Commander U. S. Naval Ordnance Test Station ATTN: Technical Library China Lake, California
1	Army Research Office ATTN: Mrs. Frances Whedon 3045 Columbia Pike Arlington, Virginia	1	Commander Pacific Missile Range ATTN: Technical Library Point Mugu, California
2	Chief of Research & Development ATTN: Atomics Office Department of the Army Washington 25, D. C.	1	Hq, USAF (AFCIN) Washington 25, D. C.
1	Chief of Naval Research ATTN: Mr. James Winchester Department of the Navy Washington 25, D. C.	1	Hq, USAF (AFRDC) Washington 25, D. C.
1	Commander Naval Missile Center ATTN: Code 212.11 Point Mugu, California	1	Hq, USAF (AFORQ) Washington 25, D. C.
3	Director U. S. Naval Research Laboratory ATTN: Dr. P. Mange Dr. Philip Shapiro Technical Library Washington 25, D. C.	1	Hq, USAF (AFDAP) Washington 25, D. C.
2	Chief of Naval Operations ATTN: Cdr W. Eaton, OP-75 Op03EG Department of the Navy Washington 25, D. C.	1	Hq, USAF (AFTAC) Washington 25, D. C.
		1	Hq, USAF ATTN: Major E. Lowry, AFRDR/NU Washington 25, D. C.
		10	AFSWC ATTN: SWRPA SWRPL CO, Naval Air Special Wpns Facility SWOI SWRPR SWRPS SWRPT SWRPI SWRJ SWRP Kirtland Air Force Base, New Mexico

# DISTRIBUTION LIST

<u>No. of Copies</u>	<u>Organization</u>	<u>No. of Copies</u>	<u>Organization</u>
1	Commander Air Force Office of Scientific Research ATTN: Tech Info and Intel Div Washington 25, D. C.	1	AFMTC (MTASI) Patrick Air Force Base, Florida
1	Commander Aeronautical Research Laboratory ATTN: Mr. Cody Wright-Patterson Air Force Base, Ohio	1	Commander Arnold Engineering Development Center Arnold Air Force Station Tullahoma, Tennessee
1	Commander Foreign Technology Division ATTN: AFCIN 4D3, Major Pearce Wright-Patterson Air Force Base, Ohio	1	APGC (PGAPI) Eglin Air Force Base, Florida
1	ASD (WWAD) Wright-Patterson Air Force Base, Ohio	1	RADC (RCOIL-2) Griffiss Air Force Base, New York
1	Office of Aerospace Research ATTN: Major Munyon Building T-D Washington 25, D. C.	1	BSD ATTN: Technical Library Norton Air Force Base, California
1	SSD ATTN: Technical Library AF Unit Post Office Los Angeles 45, California	1	ESD L. G. Hanscom Field Bedford, Massachusetts
1	Commander 6555 Test Wing (Dev) ATTN: DWZS, Lt Col J. G. Henry Patrick Air Force Base, Florida	3	AFSC (SCR, DCS/R&E) ATTN: Capt Bay Berrier Andrews Air Force Base Washington 25, D. C.
1	MDC Holloman Air Force Base, New Mexico	7	AFCRL ATTN: Dr. K. Champion CRT CRTPM CRZI CRZC CRZA CRRK L. G. Hanscom Field Bedford, Massachusetts
1	AFIT Wright-Patterson Air Force Base, Ohio	4	Scientific and Technical Information Facility ATTN: NASA Representative (S-AK/DL) Dr. Blumle Dr. R. Bordeau Dr. Martin Swetnick P. O. Box 5700 Bethesda, Maryland

# DISTRIBUTION LIST

<u>No. of Copies</u>	<u>Organization</u>	<u>No. of Copies</u>	<u>Organization</u>
5	NASA Goddard Space Flight Center ATTN: Mr. John Naugle Mr. Robert E. Bourdeau Mr. N. W. Spencer Mr. J. C. Seddon Mr. J. E. Jackson Greenbelt, Maryland	1	U. S. Atomic Energy Commission Los Alamos Scientific Laboratory ATTN: Report Librarian P. O. Box 1663 Los Alamos, New Mexico
1	NASA Facility Wallops Island ATTN: Robert L. Kreiger Temperanceville, Virginia	1	University of California Lawrence Radiation Laboratory ATTN: Technical Information Div P. O. Box 808 Livermore, California
6	Director National Bureau of Standards Central Radio Propagation Lab. ATTN: Alan Shapley Dr. R. Lawrence Dr. T. Van Zandt Mr. W. Wright Dr. K. Davies Technical Library Boulder, Colorado	1	U. S. Atomic Energy Commission Division of Technical Information Extension P. O. Box 62 Oak Ridge, Tennessee
2	National Science Foundation ATTN: Dr. Earl Dressler Atmospheric Sciences Washington 25, D. C.	1	President Sandia Corporation ATTN: Classified Document Division Sandia Base Albuquerque, New Mexico
1	Director Argonne National Laboratory ATTN: Technical Library 9700 South Cass Argonne, Illinois	2	Director Armour Research Foundation ATTN: Document Library Dr. C. M. Haaland Illinois Institute of Technology Center Chicago 16, Illinois
1	Director Oak Ridge National Laboratory ATTN: Technical Library P. O. Box "P" Oak Ridge, Tennessee	10	IGY World Data Center A Rockets and Satellites National Academy of Science 2101 Constitution Avenue Washington 25, D. C.
1	Brookhaven National Laboratory Technical Information Division ATTN: Classified Document Section Upton, New York	10	IGY World Data Center A Airglow and Ionosphere Central Radio Propagation Lab. National Bureau of Standards Boulder, Colorado

# DISTRIBUTION LIST

<u>No. of Copies</u>	<u>Organization</u>	<u>No. of Copies</u>	<u>Organization</u>
1	Boeing Aerospace Division ATTN: Dr. E. L. Chupp Seattle, Washington	1	Kaman Aircraft Corporation Nuclear Division ATTN: Dr. Frank Shelton Garden of the Gods Road Colorado Springs, Colorado
1	CONVAIR, A Division of General Dynamics Corporation ATTN: Dr. Victor Van Lint P. O. Box 1950 San Diego 12, California	1	Lockheed Missiles and Space Division Technical Information Center ATTN: Dr. Roland Meyerott 3251 Hanover Street Palo Alto, California
1	Cornell Aeronautical Laboratory, Inc. Box 235 Buffalo 21, New York	1	Director Lincoln Laboratory ATTN: Mr. James Pannell P. O. Box 73 Lexington 73, Massachusetts
1	Electro-Optical Systems, Inc. ATTN: Dr. Henry Richter, Jr. 125 N. Vinedo Avenue Pasadena, California	1	Mitre Corporation Middlesex Turnpike Bedford, Massachusetts
1	E. H. Plesset Associates, Inc. 1281 Westwood Boulevard Los Angeles 24, California	2	Millstone Hill Radar Station ATTN: Dr. H. W. Briscoe P. O. Box 276 North Chelmsford, Massachusetts
1	Edgerton, Germeshausen & Grier, Inc. ATTN: Dr. M. Shuler 160 Brookline Avenue Boston 15, Massachusetts	2	North Atlantic Radio Warning Service National Bureau of Standards P. O. Box 178 Fort Belvoir, Virginia
1	Geophysics Corporation of America Burlington Road Bedford, Massachusetts	1	Republic Aviation Corporation 223 Jericho Turnpike Mineola, New York
1	G. C. Dewey Company 202 E. 44th Street New York, New York	2	The Rand Corporation ATTN: Technical Library Dr. Robert Lelevier 1700 Main Street Santa Monica, California
4	General Electric Company Technical Military Planning Operation ATTN: Mr. Walter Hausz Dr. Walter Dudzick Dr. Roy Hendrick DASA Data Center 735 State Street Santa Barbara, California		



# DISTRIBUTION LIST

<u>No. of Copies</u>	<u>Organization</u>	<u>No. of Copies</u>	<u>Organization</u>
1	State University of Iowa Physics Department ATTN: Document Control Station for Dr. J. A. Van Allen Iowa City, Iowa	2	University of Michigan Department of Electrical Engineering ATTN: Mr. Andrew Nagy Mr. Larry Brace Ann Arbor, Michigan
1	Director Stanford Research Institute ATTN: Document Custodian for Dr. Allen Peterson, I. G. Poppoff Menlo Park, California	2	The Pennsylvania State University ATTN: Professor A. H. Waynick Dr. W. J. Ross Ionospheric Research Laboratory University Park, Pennsylvania
1	Stanford University ATTN: Security Officer Stanford, California	1	Dr. Wolfgang Pfister Geophysics Research Directorate Laurence B. Hanscomb Field Bedford, Massachusetts
1	Space Technology Laboratories, Inc. 5730 Arbor Vitae Street Los Angeles 45, California	1	Dr. Gian Carlo Rumi School of Electrical Engineering Cornell University Ithaca, New York
1	University of California Lawrence Radiation Laboratory ATTN: Dr. Ken Watson Berkeley 4, California	10	The Scientific Information Center Defence Research Staff British Embassy 3100 Massachusetts Avenue, N. W. Washington 8, D. C.
2	University of Illinois ATTN: Professor G. Swenson Professor S. Bowhill Champaign, Illinois	4	Defence Research Member Canadian Joint Staff 2450 Massachusetts Avenue, N. W. Washington 8, D. C.

<p>AD Ballistic Research Laboratories, AF SUMMARY REPORT ON STROGARM ROCKET MEASUREMENTS OF ELECTRON DENSITY TO AN ALTITUDE OF 1500 KILOMETERS S. T. Marks, C. E. Shafer, W. J. Cruickshank, R. E. Frenett and G. A. Dalk REL Report No. 1187 January 1963 REF &amp; E Project No. 1A011001B021 UNCLASSIFIED Report</p>	<p>UNCLASSIFIED</p> <p>Upper atmosphere - Electron density Upper atmosphere - Instrumentation Ionosphere - Electron density</p> <p>A summary report is presented which covers all phases of a project for the measurement of electron density to an altitude of 1500 kilometers by employing a five-stage solid propellant rocket combination known as the Strogarm, and a two-frequency propagation experiment. Included in the report are sections which describe the theory applicable to the measurements, the rocket vehicle, the airborne instrumentation, the ground instrumentation, the vehicle performance, and the experimental results. An early morning electron density profile to an altitude of 1500 kilometers is presented, together with a daytime and a nighttime profile to 650 kilometers. A model of the ionospheric inhomogeneities which existed during the daytime rocket flight is given. Scale heights and exospheric temperatures derived from the profiles are also presented and discussed.</p>
<p>AD Ballistic Research Laboratories, AF SUMMARY REPORT ON STROGARM ROCKET MEASUREMENTS OF ELECTRON DENSITY TO AN ALTITUDE OF 1500 KILOMETERS S. T. Marks, C. E. Shafer, W. J. Cruickshank, R. E. Frenett and G. A. Dalk REL Report No. 1187 January 1963 REF &amp; E Project No. 1A011001B021 UNCLASSIFIED Report</p>	<p>UNCLASSIFIED</p> <p>Upper atmosphere - Electron density Upper atmosphere - Instrumentation Ionosphere - Electron density</p> <p>A summary report is presented which covers all phases of a project for the measurement of electron density to an altitude of 1500 kilometers by employing a five-stage solid propellant rocket combination known as the Strogarm, and a two-frequency propagation experiment. Included in the report are sections which describe the theory applicable to the measurements, the rocket vehicle, the airborne instrumentation, the ground instrumentation, the vehicle performance, and the experimental results. An early morning electron density profile to an altitude of 1500 kilometers is presented, together with a daytime and a nighttime profile to 650 kilometers. A model of the ionospheric inhomogeneities which existed during the daytime rocket flight is given. Scale heights and exospheric temperatures derived from the profiles are also presented and discussed.</p>
<p>AD Ballistic Research Laboratories, AF SUMMARY REPORT ON STROGARM ROCKET MEASUREMENTS OF ELECTRON DENSITY TO AN ALTITUDE OF 1500 KILOMETERS S. T. Marks, C. E. Shafer, W. J. Cruickshank, R. E. Frenett and G. A. Dalk REL Report No. 1187 January 1963 REF &amp; E Project No. 1A011001B021 UNCLASSIFIED Report</p>	<p>UNCLASSIFIED</p> <p>Upper atmosphere - Electron density Upper atmosphere - Instrumentation Ionosphere - Electron density</p> <p>A summary report is presented which covers all phases of a project for the measurement of electron density to an altitude of 1500 kilometers by employing a five-stage solid propellant rocket combination known as the Strogarm, and a two-frequency propagation experiment. Included in the report are sections which describe the theory applicable to the measurements, the rocket vehicle, the airborne instrumentation, the ground instrumentation, the vehicle performance, and the experimental results. An early morning electron density profile to an altitude of 1500 kilometers is presented, together with a daytime and a nighttime profile to 650 kilometers. A model of the ionospheric inhomogeneities which existed during the daytime rocket flight is given. Scale heights and exospheric temperatures derived from the profiles are also presented and discussed.</p>
<p>AD Ballistic Research Laboratories, AF SUMMARY REPORT ON STROGARM ROCKET MEASUREMENTS OF ELECTRON DENSITY TO AN ALTITUDE OF 1500 KILOMETERS S. T. Marks, C. E. Shafer, W. J. Cruickshank, R. E. Frenett and G. A. Dalk REL Report No. 1187 January 1963 REF &amp; E Project No. 1A011001B021 UNCLASSIFIED Report</p>	<p>UNCLASSIFIED</p> <p>Upper atmosphere - Electron density Upper atmosphere - Instrumentation Ionosphere - Electron density</p> <p>A summary report is presented which covers all phases of a project for the measurement of electron density to an altitude of 1500 kilometers by employing a five-stage solid propellant rocket combination known as the Strogarm, and a two-frequency propagation experiment. Included in the report are sections which describe the theory applicable to the measurements, the rocket vehicle, the airborne instrumentation, the ground instrumentation, the vehicle performance, and the experimental results. An early morning electron density profile to an altitude of 1500 kilometers is presented, together with a daytime and a nighttime profile to 650 kilometers. A model of the ionospheric inhomogeneities which existed during the daytime rocket flight is given. Scale heights and exospheric temperatures derived from the profiles are also presented and discussed.</p>